ORNL/NRCHQ2514D0004
Task Order 31310018F0058 M0001

Review of Advanced Manufacturing Techniques and Qualification Processes for Light Water Reactors—Laser Powder Bed Fusion Additive Manufacturing

Joseph Simpson
Ryan Dehoff

September 18, 2020

OAK RIDGE NATIONAL LABORATORY
MANAGED BY UT-BATTELLE FOR THE US DEPARTMENT OF ENERGY

ORNL/NRCHQ2514D0004
Task Order 31310018F0058 M0001

MANUFACTURING DEMONSTRATION FACILITY
Materials Science and Technology Division

REVIEW OF ADVANCED MANUFACTURING TECHNIQUES AND QUALIFICATION PROCESSES FOR LIGHT WATER REACTORS—LASER POWDER BED FUSION ADDITIVE MANUFACTURING

Joseph Simpson
Ryan Dehoff

Date Published: September 18, 2020

Prepared by
OAK RIDGE NATIONAL LABORATORY
Oak Ridge, TN 37831-6283
managed by
UT-BATTELLE, LLC
for the
US Nuclear Regulatory Commission
under contract NRCHQ2514D0004
Task Order 31310018F0058 M0001

CONTENTS

LIST OF FIGURES

LIST OF TABLES

ABBREVIATIONS

2D	two-dimensional
3D	three-dimensional
AI	artificial intelligence
AM	additive manufacturing
AMM	advanced manufacturing method
AMT	advanced manufacturing technology
ANSI	American National Standards Institute
ASTM	American Society for Testing and Materials
AWS	American Welding Society
CAD	computer-aided design
CCD	charged coupled device
CT	computed tomography
DED	directed energy deposition
DOE	US Department of Energy
EDM	electrical discharge machining
EDS	energy-dispersive x-ray spectroscopy
GE	General Electric
HAZ	heat-affected zone
HdH	hydride-dehydride
HIP	hot isostatic press
HT	heat-treated
HV	Vickers hardness scale
IASCC	irradiation-assisted stress corrosion cracking
ISO	International Organization for Standardization
LED	linear energy density
LPBF	laser powder bed fusion
NASA	National Aeronautics and Space Administration
Nd:YAG	neodymium-doped yttrium aluminum garnet
NIST	National Institute of Standards and Technology
NPP	nuclear power plant
NRC	Nuclear Regulatory Commission
ORNL	Oak Ridge National Laboratory
PBF	powder bed fusion

QA	quality assurance
QC	quality control
QM	Quality Management
SCC	stress corrosion cracking
SEM	scanning electron microscopy
STL	stereolithography
UTS	ultimate tensile strength
VED	volume energy density
YS	yield strength

EXECUTIVE SUMMARY

Additive Manufacturing, specifically Laser Powder Bed Fusion, is being explored by academic, industrial, and regulatory entities for technical feasibility, cost effectiveness, and safety of fabricating components for nuclear power plant applications. Laser Powder Bed Fusion is capable of fabricating highly complex geometries, and in some applications can reduce assemblies of 10s of parts to a single as-fabricated component. In conventional manufacturing the material properties are well characterized, and the difficulty lies in machining and forming the desired geometry. In laser powder bed fusion, the difficulty lies in characterizing material properties while geometric freedom is nearly unlimited.

In general, laser powder bed fusion is a reproducible process with material properties equivalent or superior to conventional manufacturing, provided that appropriate calibration, technician training, and feedstock tracking is followed. However, quantitative data on part to part variability in a production setting, powder feedstock lot to lot variability, and machine to machine variability is not readily available due to corporate confidentiality. Academic studies have attempted to address the knowledge gap in property variability, but frequently suffer from incomplete reporting, narrow focus, and lack of replicate specimens. As a result, reported material property values for laser powder bed fusion components vary widely in common measurements such as yield strength (YS) and ultimate tensile strength (UTS). Specific properties such as irradiation stress corrosion cracking (SCC) crack growth rates may only have one or two published journal articles.

Many of the codes and standards indirectly supporting laser powder bed fusion are well established (e.g. powder measurement, laser calibration). Codes and standards specifically on laser powder bed fusion vary widely in quality, and some standards explicitly contradict on a few important details such as feedstock recycling criterion. The National Aeronautics and Space Administration (NASA) has published MSFC-STD-3716, which provides a statistically rigorous framework for determining material properties and design values in the context of a laser powder bed fusion production setting. AWS and ASTM standards on laser powder bed fusion specify collecting material property data from simplified geometries such as cylinders and bars. However, the authors recommend that material properties initially not be evaluated from simplified geometries but instead from sectioned end-use geometry components when possible. Material properties are a function of geometry in laser powder bed fusion, and the use of simplified geometries may give erroneous values. In the context of light water reactors, additional studies are needed on the dendritic microstructure of laser powder bed fusion 316L, on the acceptable chemical composition range of laser powder bed fusion 316L (which may not be identical to conventional 316L), and on differences in welding laser powder bed fusion materials relative to conventional materials. Some of above studies are already in progress or under consideration with ASME Code Cases.

In summary, additive manufacturing represents a significant opportunity for American manufacturing and nuclear electrical energy generation. Some codes and standards details must be resolved empirically as production data becomes available, and additional studies on the microstructure and welding of laser powder bed fusion 316L are needed. However, early studies indicate that laser powder bed fusion 316L can offer equivalent or superior performance relative to conventional 316L given appropriate manufacturing parameters and heat treatments, while significantly improving cost effectiveness and reducing assembly complexity. The NRC has developed a companion document to this report (ML20351A204) that provides context to the gaps identified in this report from a regulatory perspective and highlights key technical information related to LPBF-fabricated components in nuclear power plants.

1. INTRODUCTION

Nuclear energy supplies approximately 18% of the US electrical power supply and the majority of carbon-free electricity [1], and is a critical component of reliable domestically sourced power. To lower construction and maintenance costs, multiple advanced manufacturing methods (AMMs) are being evaluated by academic, industrial, and regulatory bodies for cost effectiveness, technical feasibility, and safety [4]. The Nuclear Regulatory Commission (NRC) is the federal agency responsible for regulating NPP operation and ensuring public safety. Therefore, the NRC has a vested interest in surveying current scientific literature on AMM. The NRC internally uses the term Advanced Manufacturing Technology (AMT) in lieu of AMM and is pursuing technical knowledge of multiple AMM per the NRC's Action Plan. The objective of this report is to document the current state of one specific AMM—laser powder bed fusion (LPBF)—with respect to material microstructures and properties relative to conventional manufacturing, technical gaps in ensuring repeatability, and standards and regulatory gaps in machine calibration, minimum requirements, and inspection practices. This report is motivated by the potential use of LPBF in fabricating components for new NPPs as well as replacing components that are no longer commercially available for use in existing NPPs. The NRC has developed a companion document to this report (ML20351A204) that provides context to the gaps identified in this report from a regulatory perspective and highlights key technical information related to LPBF-fabricated components in nuclear power plants.

2. LPBF TECHNICAL REVIEW

Additive manufacturing (AM) is a collection of technologies that fabricate components by selectively adding material layer by layer as opposed to conventional subtractive manufacturing, which removes material from a blank or billet or shapes material via stamping or forging. AM has progressed rapidly in the past 30 years from rapid design prototyping with polymers in the automotive industry to scale production of metal components as evidenced by Boeing's use of AM to reduce weight in the 787 Dreamliner [5] and SES-15 spacecraft [6] and General Electric's (GE's) decision to produce aviation fuel injection nozzles via AM [7]. Some of the most common metal AM technologies at the time of this review are laser powder bed fusion (LPBF) and electron beam melting (both of which are powder bed fusion (PBF) technologies [8–10]), laser directed energy deposition (DED), and binder jetting.

Key AM technologies that may be used in the fabrication of nuclear reactor core structures are LPBF, laser DED, and binder jetting. These technologies are not currently in widespread use in fabricating components for NPP service but have the potential to drastically reduce fabrication costs and timelines, combine multiple systems and assembled components into single parts, and increase safety and performance by tailoring local material properties and redesigning geometries for optimal load paths. Terminology within the LPBF industry is highly unstructured and frequently proprietary; Table 1 contains a list of common and proprietary terminology where each term is synonymous with LPBF.

Table 1. Common and proprietary synonyms for LPBF.

Terminology	Patent Owner
Cusing	Concept Laser/General Electric
Selective laser melting	SLM Solutions
Direct powder bed fusion	—
Direct metal laser sintering	—
Direct metal laser melting	General Electric

The following review represents the current state of literature on LPBF and emphasizes quality control (QC), material performance repeatability, and component performance compared with conventionally manufactured materials. Research and standards published by government entities such as the National Institute of Standards and Technology (NIST) and the US Department of Energy (DOE) have been included where applicable. Literature should be reviewed, and new knowledge should be integrated frequently because of the rapid pace of advancements in AM and associated industries. AM presents unique challenges in certification for NPP applications such as anisotropic material properties, porosity, underdeveloped process control feedback systems, and reproducibility. Conventional manufacturing also has challenges with variability; however, conventional component variability is generally concerned with geometric accuracy rather than material properties. Casting is the most analogous conventional manufacturing method with respect to material property variability and defects (e.g., porosity). This review begins with an overview of LPBF, followed by a systematic review of literature to detail the fabrication process and difficulties with repeatably fabricating fully dense, geometrically accurate components with known material properties, and a ranking of essential safety differences and a Codes and Standards gap analysis.

2.1 TERMINOLOGY

Several terms used by the LPBF industry are specifically relevant to QC and include short feeding, streaking, swelling, chatter, denudation, and spatter. “Short feeding” may also be referred to as “incomplete feeding” or “short spreading” and is used to describe when the recoater spreads an incomplete layer of powder across the top surface of the build chamber, typically due to low powder dosing rates. Figure 32 depicts short feeding as well as several other LPBF processing discontinuities. “Streaking” refers to uneven powder spreading caused by worn recoater blades. When grooves are abraded into the recoater blade, powder will spread through the grooves as well as under the blade, resulting in powder mounds parallel to the recoater travel. “Swelling” or “super elevation” describes the swelling and volumetric expansion of a component, typically upward, which can prevent uniform powder spreading and may abrade the recoater if severe. Swelling is caused by warping of components and is typically most severe at the perimeter of the components. “Chatter” or “recoater hopping” refers to the recoater bouncing vertically when spreading powder. Chatter typically occurs because of LPBF machine warpage or powder caught in the recoater guide rails. “Denudation” is a relatively recent discovery within the LPBF community and refers to gas convection conditions under which powder feedstock is blown away from the melt pool. “Spatter” refers to large molten ejecta that leave the melt pool and is likely familiar to readers with a background in welding.

2.2 MANUFACTURING METHOD

LPBF fabricates components by sequentially melting thin layers of metal powder together to create the specified geometry. The process begins with a user designing a three-dimensional (3D) computer-aided design (CAD) model of the component in an engineering design software package (e.g., SolidWorks, Autodesk, or AutoCAD). The CAD model is then loaded into a separate software package for LPBF specific processing; this processing is commonly referred to as “slicing” within the LPBF industry. Slicing consists of separating the original CAD model into multiple layers that are vertically stacked; slicing is not proprietary, is required for all LPBF machines, and is conducted in a virtually identical manner for all LPBF machine manufacturers. Figure 1 [11] illustrates a CAD model prior to and after slicing.

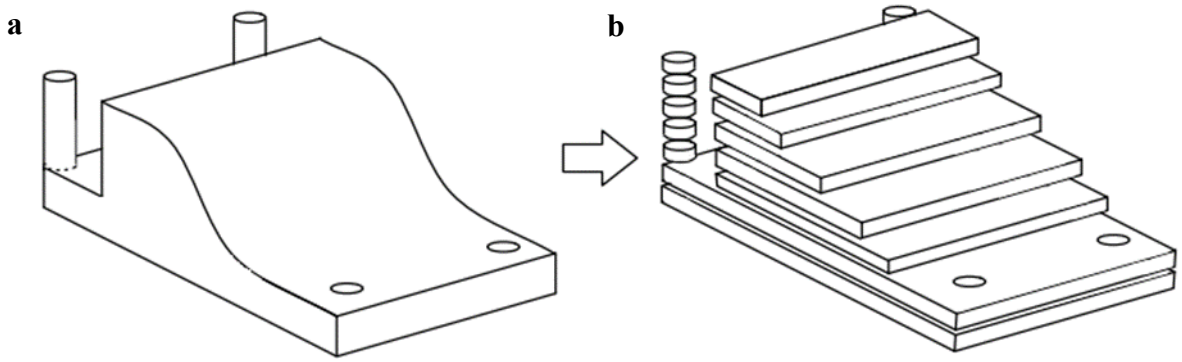

Figure 1. Example CAD slicing (a) before slicing and (b) after slicing [11].

After slicing, each layer of the sliced CAD model is assigned a unique scan strategy calculated for that layer. "Scan strategy" refers to all settings used by the LPBF machine (e.g., laser power, laser acceleration, laser beam diameter, acceptable O_2 levels) as well as the two-dimensional (2D) path that the laser travels. Once a CAD model has been sliced and scan strategies have been assigned to each layer, the files are transferred to the LPBF machine.

LPBF machine setup is completed by cleaning the machine, installing a flat "build plate" or "start plate" upon which the component is fabricated, and loading sieved metal powder for feedstock. Build plates are flat, thick (2 to 3 in.) metal plates and are treated as consumables. Figure 2 [12] provides a system schematic representative of many LPBF machines. A thin layer of metal powder is spread from the powder tank across the surface of the build plate via a recoating mechanism. Any excess powder from recoating is deposited into an overflow container for later sieving and reuse. The laser then activates and scans the 2D outline of the first (bottom) layer using the settings and laser path in the scan strategy for the first layer. After the first layer is fused together, the laser deactivates and the recoater spreads a second layer of metal powder. The laser then scans and fuses the second layer using the second layer's scan strategy, and the recoating/scanning process is repeated until the component is fabricated.

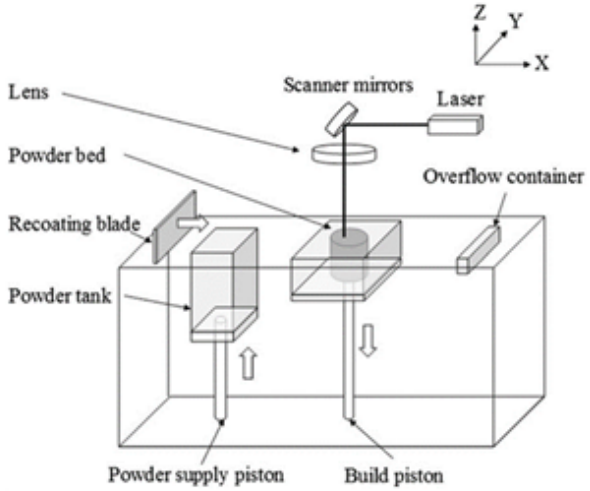

Figure 2. System schematic for generic LPBF system [12].

2.2.1 Powder Evaluation

Feedstock powders must be evaluated and carefully selected based on elemental composition, flowability, internal porosity, particle geometry, size distribution, and surface features to minimize or eliminate fabrication issues such as uneven powder spreading and feedstock induced porosity. Many powder manufacturers publish information on the sieve sizes used in production or the mean particle size; however, the D10, D50, and D90 (particle size at which 10%, 50%, and 90% of particles are respectively of equal or lesser size) of a particle size distribution should be documented. The powder size distribution has been documented to directly affect flowability [13], and flowability qualitatively affects the powder packing density and probability of manufacturing defects such as incomplete spreading. Powder reuse tends to shift the size distribution towards larger particles; flowability generally improves with powder reuse due to fewer smaller particles [14]. Low flowability may result in incomplete spreading, non-uniform spreading or spreading system jamming. ORNL staff experience indicates that as flowability increases, manufacturing complications decrease in frequency until a threshold is reached and said complications are observed highly infrequently. Further increases in flowability beyond the flowability threshold do not result in observable improvement. Powder characteristics may be measured via scanning electron microscopy (SEM) and energy-dispersive x-ray spectroscopy (EDS) [15], and the Hall Flow Meter. SEM can image dispersed samples of metal powder, typically against highly contrasting and conductive backgrounds such as carbon, to identify individual particles and the particle size distribution. SEM can simultaneously provide qualitative information on particle shape and the presence of satellites. EDS is a well-established method of determining rough elemental composition, and if particles are sufficiently well dispersed when imaging, the composition of the overall sample and also individual particles can be determined. Powder flowability may be quantitatively measured via the Hall Flow Meter method. Analyses of powder characteristics and their measurement have been described in the following publications [16,17].

2.2.1.1 Elemental Composition

Control over the elemental composition of metal AM components is critical to ensuring QC and predictable properties. Therefore, virtually all systems use pre-alloyed powders to achieve high elemental control and homogeneity [18]. The elemental composition of fabricated components may deviate from that of the feedstock because of four primary causes: powder cross-contamination, melt pool vaporization, oxidation of feedstock, and oxidation of the melt pool. Melt pool oxidation is minimized by operating in a high-purity inert gas environment for LPBF [19]. Powder cross-contamination is known to be a serious area of concern and can only be solved by either dedicating machines to a single feedstock or meticulously cleaning during powder changeovers. Metal vaporization may be a concern for elements with high vapor pressures [20], but the high travel speed of the melt pool means any location on the build surface is only momentarily molten before solidifying. One study on Ti-6Al-4V demonstrated the ability to numerically predict the vaporization mass loss for selected elements in an Arcam melt pool and experimentally demonstrated a mean aluminum loss of 0.12 wt % per melt cycle over five melt cycles [21]. Whether compositional change due to vaporization is significant depends on the specific alloy used, the powder lot elemental composition, and the role of the element of interest in solidification and microstructure formation.

One way to reduce the cost of LPBF components is to recycle powder; some systems, such as the Concept Laser X Line, automatically sieve and store recycled powder in a closed-loop inert gas environment whereas other systems expose recycled powder to air during handling and sieving. The latter method may alter the chemical composition of powder over multiple reuse cycles via oxidation. In one study, Ti-6Al-4V powder repeatedly recycled and exposed to air in an Arcam electron beam PBF system revealed an oxygen increase from 0.08 to 0.19 wt %, aluminum decrease from 6.47 to 6.37 wt %, and vanadium decrease from 4.08 to 4.03 wt % over 21 cycles [22]. Determining whether a compositional

change, irrespective of cause, is significant requires two analyses. First, the compositional change must be compared against the inter- and intra-lot variability from the powder supplier, including measurement uncertainty. If a compositional change is within inter-lot variability or measurement noise levels, it is highly unlikely to result in meaningful microstructural differences. Secondly, if the composition change is statistically significant, the effect must be evaluated on an element-by-element basis for a given alloy. For example, a 0.10% increase in oxygen may result in negligible changes to the microstructure and material properties for one alloy and highly detrimental changes in a second alloy.

A 2017 study by NIST evaluated numerous powder characteristics for S17-4 PH stainless steel powder reused over 11 cycles and concluded that no statistically significant difference existed in powder microstructure, morphology, size distribution, chemical composition, or mechanical properties of the fabricated specimens; powder bed packing density and flowability improved with increasing cycles [23]. A more recent 2019 study [24] evaluated 316L feedstock composition before and after 30 reuse cycles and found that only oxygen and carbon changed by statistically significant amounts. The reused powder contained a carbon content of 0.016 wt % (standard deviation of 0.002), which is within the American Society for Testing and Materials (ASTM) F3184 - 16 specification of 0.030 wt % max; ASTM F3184 - 16 does not specify acceptable oxygen content. Single crystal ferrite particles were present in the recycled powder, but not virgin feedstock as shown in Figure 3 [24]. A mechanism of spatter ejecta from the melt pool that solidifies in the inert gas environment of the build chamber was proposed for the observed ferrite formation. Alternatively, feedstock particles near the melt pool or entrained by the vapor plume could undergo a rapid solid-state heat treatment resulting in ferrite. Critically, however, the study did not report whether detectable quantities of ferrite were observed in the fabricated components. Therefore, it is unclear at this time whether ferrite in either virgin or recycled 316L feedstock correlates to ferrite in fabricated components.

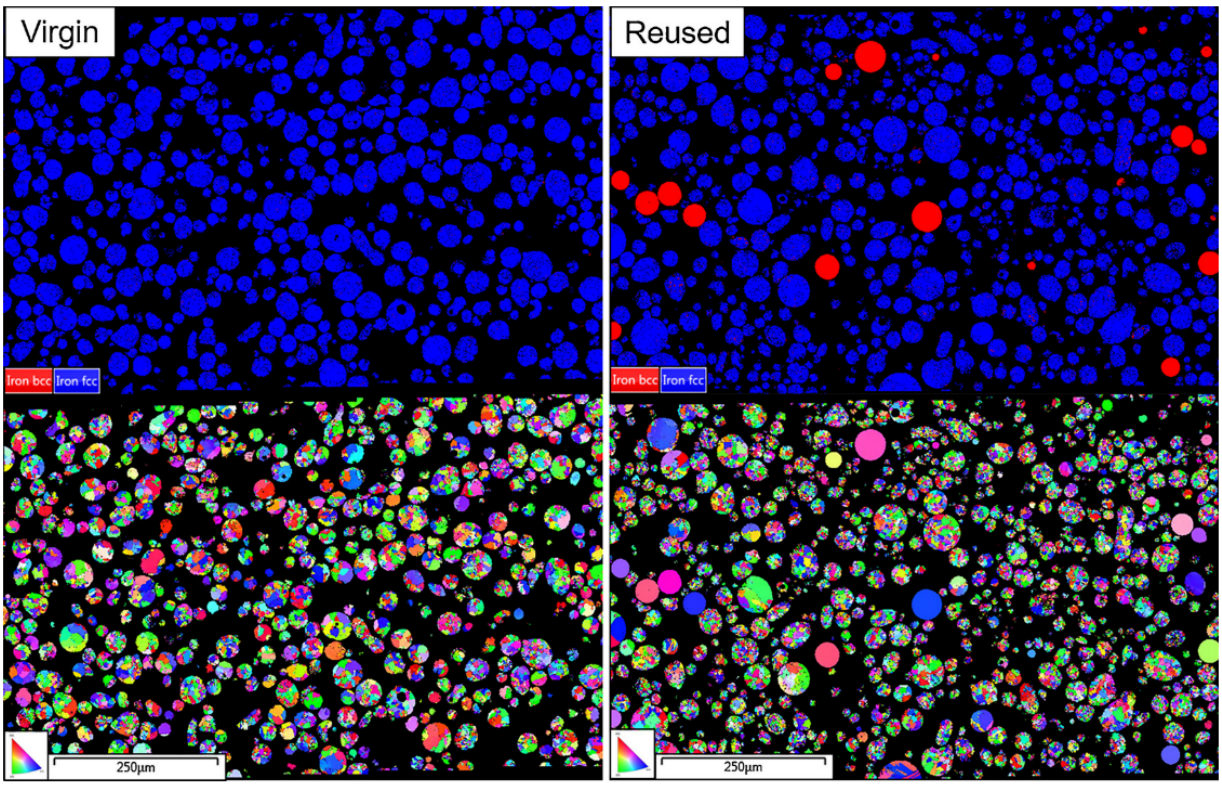

Figure 3. Inverse pole map of virgin and recycled 316L [24]**.**

Heiden et al. [24] also reported the presence of nanoscale SiO_2 surface growths on virgin powder and larger SiO_2 and $MnCr_2O_4$ growths on recycled powder as shown in Figure 4 [24]. The powder production method was not specified, but preferential oxygen scavenging by Si is likely the main cause of the oxide growths in the virgin powder. Oxygen scavenging during the LPBF process also likely caused the $MnCr_2O_4$ growths and enlarged SiO2 inclusions. SiO_2 inclusions in LPBF 316L fabricated components have been correlated to accelerated SCC crack growth rates; the topic is discussed in depth in Section 2.4.1. Taken as a whole, powder recycling appears to have beneficial and detrimental effects on the QC of the fabrication process as well as on fabricated component material properties. However, quantitative standards for determining when powder can no longer be recycled are needed.

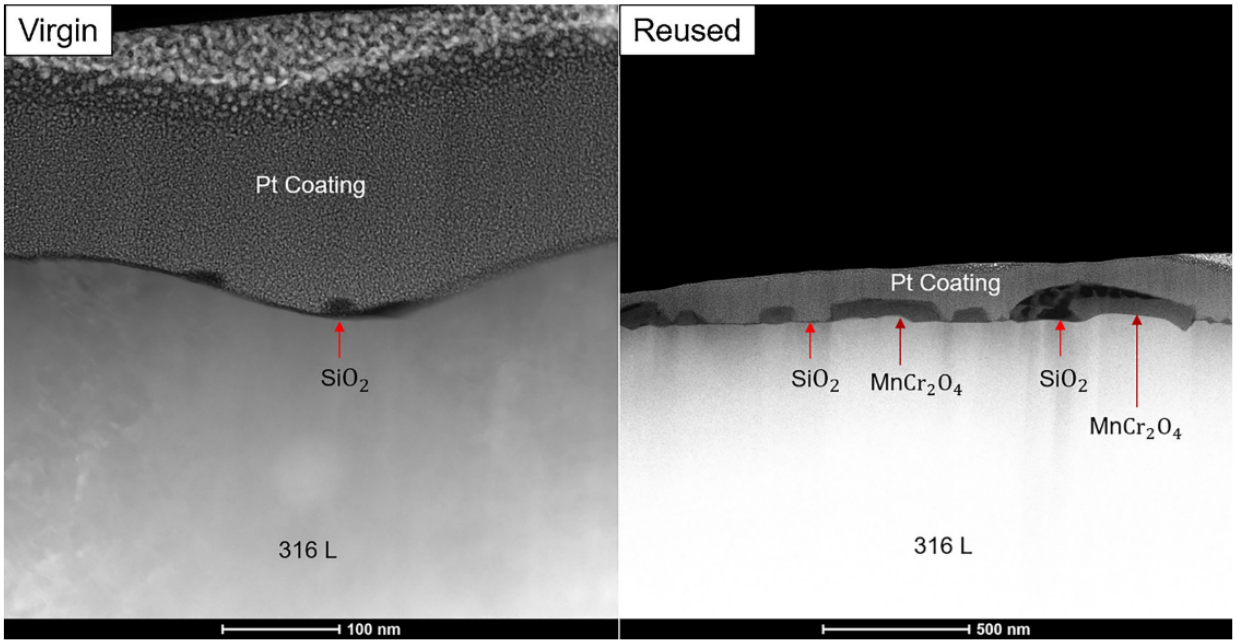

Figure 4. Observation of oxides on 316L feedstock particle surfaces [24]**.**

2.2.1.2 Powder Porosity

Internal porosity and trapped gas in powders can result in porosity in metal AM-fabricated components [25] and is one of several porosity sources in LPBF; therefore, minimizing internal porosity in feedstocks is typically desirable. Porosity in components resulting from gas entrapped in powder can be recognized by spherical voids whereas fabrication process–induced porosity tends to exhibit irregular and elongated voids as shown in Figure 5 [18] and Figure 6. [26]. Figure 5. Powder porosity largely depends on the production technology used. Powders produced via plasma atomization or a plasma rotating electrode process have been shown to eliminate voids resulting from gas entrapped in powder [25–27] whereas gas atomization yields powder with significant quantities of entrapped gas as shown in Figure 7 [26]. Gas atomization and rotary atomization yield powders with satellites and irregular shapes, respectively, which adversely affect flowability and powder packing density.

Another powder production technique that has been evaluated for LPBF applications is hydride-dehydride (HdH) [28]. Bulk metal is converted to a metal-hydride via a gas-solid chemical reaction. The resulting phase transformation results in significant (>15 vol %) expansion that produces significant stresses, pulverizing the brittle hydride into powder. The hydrogen is then removed by heating the hydride under vacuum, recovering the metal in powder form. HdH powder has been shown to have difficulties with high levels of porosity, but porosity could be reduced by a “double melt” method and hot isostatic pressing

(HIPing). “Double melting” refers to the practice of rastering the laser across each layer a second time (as compared with the standard practice of melting a layer a single time). Analysis of process parameters on powder atomization-induced and process-induced porosity has been reported elsewhere [29].

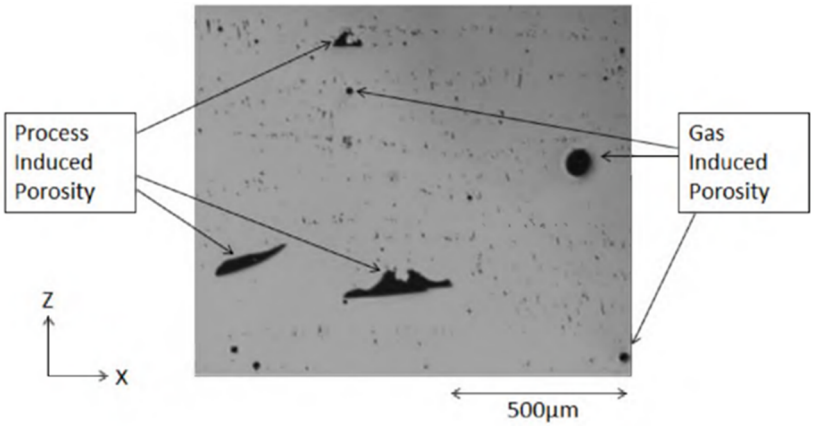

Figure 5. Process-induced porosity vs. gas-induced porosity [18]**.**

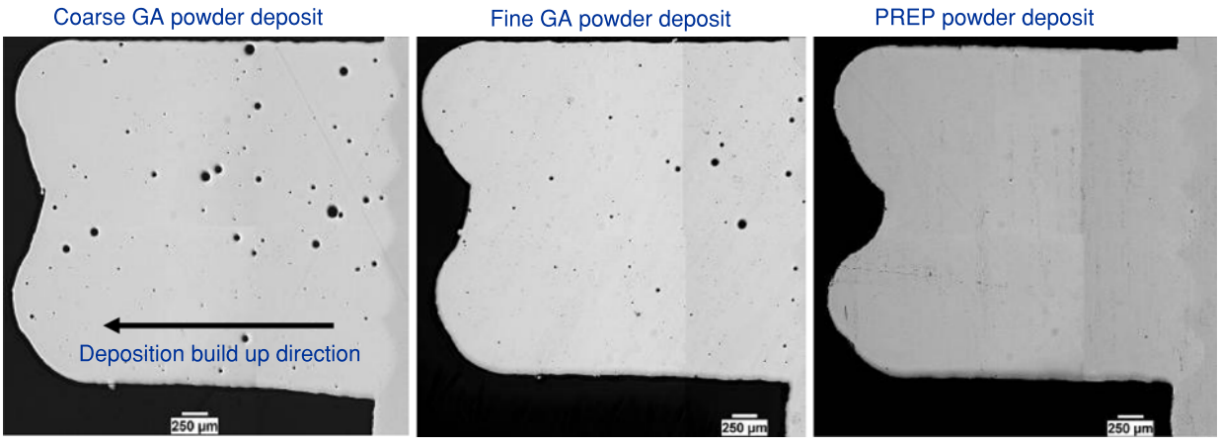

Figure 6. Examples of powder atomization-induced porosity in components [26]**.**GA = gas-atomized; PREP = plasma rotating electrode process

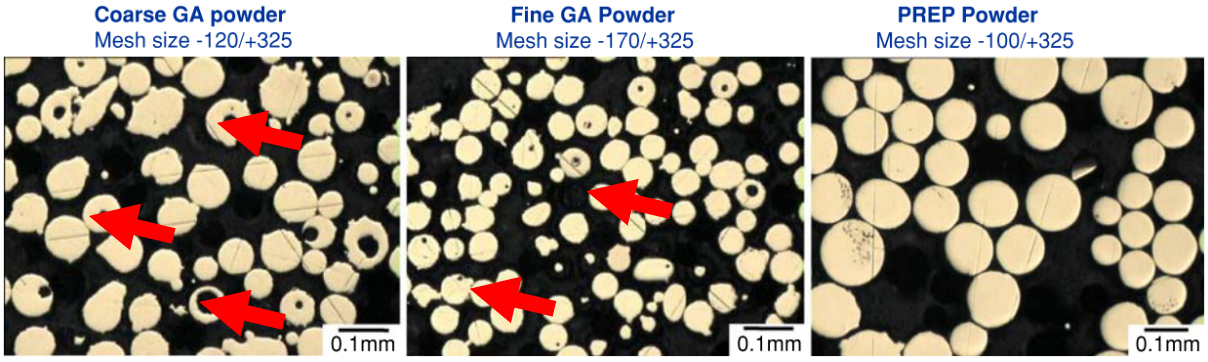

Figure 7. Examples of powder porosity [26]**.**

2.2.2 File Preparation

File preparation consists of machine instructions on the energy source scan path, timing of turning the energy source on and off, layer thickness, energy source spot size, energy output, environmental parameters, and coater parameters. The machine parameters and scan strategy used must ensure complete fusion while avoiding issues such as melt pool balling, delamination, porosity, warping, and unacceptable residual stresses. Melt pool "balling" refers to beads or balls that form on the top of the melt pool under specific conditions due to surface tension in the molten metal and are illustrated in Figure 12. Two terms related to file preparation that are commonly used in the LPBF community are "contour" and "infill." "Contour" refers to the outside edge of a layer slice and "infill" refers to the interior of a layer slice. "Scan strategy" in the context of LPBF refers to the path the laser travels during the melting process. Multiple scan strategies such as bidirectional rastering, unidirectional travel, and checkerboard/island have been developed as illustrated in Figure 8 [30]. Scan strategy optimization depends on if the objective is build time minimization, thermal gradient reduction, or surface finish quality, as well as the limitations of the LPBF system.

Unidirectional and bidirectional infill scanning have historically been prevalent because of the high efficiency and simplicity of programming; however, these strategies develop high thermal gradients and, therefore, internal stresses. Island scanning melts randomized unidirectional or bidirectional patches in a checkerboard pattern as a compromise between the efficiency of bidirectional scanning and the thermal gradient reduction of randomized spot melting and has been shown to reduce residual stress [31]. LPBF typically melts the contour after melting the infill to achieve smoother surface finishes than melting the contour before the infill [31].

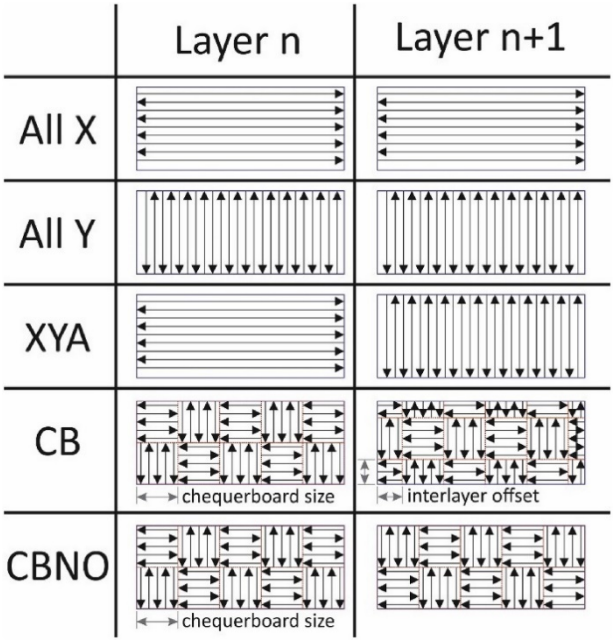

Figure 8. A variety of commercially available scan strategies [30]**.** CB = checkerboard with interlayer offset. CBNO = checkerboard with no interlayer offset.

Many LPBF systems provide significant flexibility to operators in choosing parameters. For example, operators may specify the scanning pattern used (e.g., unidirectional, bidirectional, checkerboard), whether contours will be melted prior to or after infill, and interlayer pattern rotation angles, laser power, laser spot size, and travel speed to name a few. These parameters directly affect the thermal history of a specific location within a component, porosity, surface quality, yield and tensile strength, and other

qualitative and quantitative outcomes. Process parameters must be coordinated to control the critical relationship between thermal energy output and melt pool velocity. At the time of this review, most PBF systems do place restrictions on scan strategies such as uniform layer thickness throughout a component, constant energy source velocities, and constant delay periods to dissipate thermal energy between layers. Scan strategy parameters are typically static and uniform; however, the way in which scan strategies and heat transfer from the melt pool interact with the component geometry is nonuniform throughout the component. Therefore, the microstructure and material properties change throughout the component because of varying local temperatures that result from heat transfer. Varying processing parameters to be nonconstant and nonlinear may be a possible route to compensate for the effect of geometry and result in uniform if not isotropic microstructures. The ability to control currently restricted parameters in addition to incorporating closed-loop control systems may aid in forming uniform microstructures. Determining what parameter combination should be used at each point throughout a component with this method is nontrivial and will likely require advances in multi-scale simulation techniques and/or computer processing power. These parameter control changes are significant technological challenges but offer the possibility of solving AM issues such as intra-component yield and tensile strength variation.

The energy source used in LPBF interacts with the powder bed and melt pool in various ways depending on the total power applied, power distribution, and processing environment. Improper processing parameters may result in one or more detrimental phenomena. Localized boiling of the melt pool is common to LPBF and may result in convective transport liquid or vapor known as “spatter” when the droplet overcomes surface tension; Figure 9 [32] depicts an example of spatter formation. Spatter is observed in LPBF and welding as white “fireworks” and is caused by excessively high temperatures in the melt pool. Ejected material is typically not a concern unless large or frequent enough to interfere with the recoater blade depositing a uniform powder layer. Ejected material must be removed from recycled powder via sieving. However, boiling of the melt pool can result in “keyhole” voids by creating metal vapor cavities where the melt pool solidifies prior to the void floating to the melt pool surface.

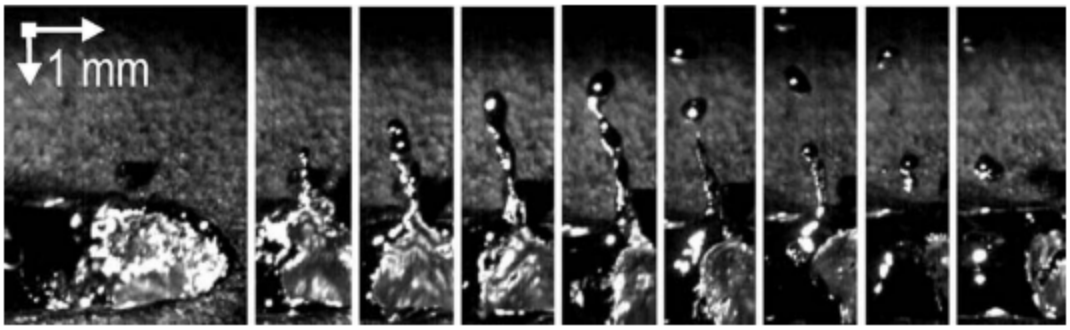

Figure 9. Example spatter formation [32]**.**

LPBF transfers energy to the powder bed or melt pool via photons. The absorptivity of powders and melt pool affect energy transfer [33], and some highly reflective powders cannot be processed with LPBF as a result of reflected energy destroying optics and sensors. LPBF laser beams are typically distributed in a Gaussian profile; however, ring beam shaping has shown the potential for finer microstructures because of more even power distribution [19]. Pulse shaping of Gaussian laser beams (the control of output power over time) has also shown the ability to reduce spatter ejection, improve surface roughness, and decrease melt pool width [34]. Pulse shaping can also effectively preheat powder, thereby decreasing reflectivity and potentially allowing for LPBF fabrication of highly reflective powders. However, pulse shaping and non-Gaussian beam profiles significantly increase computational requirements. One study recently discovered phenomena in LPBF is “denudation,” in which convective gas currents above the melt pool blow powder away from the melt pool [35,36]; comparatively little is known about causes, effects, or solutions to denudation in comparison with keyholing or spatter formation. One 2020 simulation article

indicated that denudation is an unavoidable aspect of LPBF but the gas currents and effects may be controlled by processing parameter selection [37]. From the perspective of component quality reproducibility, a thorough knowledge base on denudation is not necessary as the effects of denudation appear to be primarily related to the laser velocity and power. Therefore, the effects of denudation are expected to be repeatable provided that the same scan strategy is used for the same component geometry. Closed feedback loop controls that alter the scan strategy in-situ may require more a thorough knowledge base on denudation.

In summary, the primary powder/laser interactions of concern are spatter formation and keyholing due to excessive energy transfer. Spatter may result in abrasion and erosion of the recoater or be dragged through the powder bed and create uneven layers. Keyholing results in spherical pores within a component. The effects of denudation on component quality are not well understood at this time.

2.2.3 LPBF Design Considerations

LPBF AM has revolutionized design in fields where it has been applied, particularly for components redesigned to use the advantages of AM. LPBF does not require straight lines, conventional simple geometries, or direct lines of sight for internal features. Design is, however, limited by four major obstacles. The simplest limitation is the build chamber size of the LPBF system. GE's ATLAS machine can fabricate components up to 1.1 × 1.1 × 0.3 m [38] and, to the authors' knowledge, is the largest commercially available LPBF system at the time of this document's publication. Most manufacturers' systems are considerably smaller with build volumes of 200 to 250 mm cubed. Components must fit within the build volume of a LPBF system during fabrication, which imposes a size limitation.

The second limitation is overhangs and unsupported surfaces. LPBF bonds one layer to the previous layer and for an overhang, no supporting layer is under the melt pool, but rather, loose powder. The lack of substrate supporting the melt pool leads to several issues including swelling, rough bottom surfaces, curling, and inconsistent heat transfer properties within the fabrication process. Swelling occurs when melted material rises above the powder bed plane as shown in Figure 10 [18] (a). The primary cause of swelling is surface tension of the melt pool, similar to humping in welding, and directly relates to melt pool geometry [25]. Underside surface roughness is affected by powder particles sintered or partially melted onto the bottom surface of the unsupported melt pool. Curling of unsupported surfaces occurs when new layers on a build solidify and contract upon cooling, warping previously deposited layers. Fabrication of overhangs is possible using support structures of lattices [39] and wafers to provide thermally conductive paths and mechanical anchoring to counter thermally induced stress. Limited unsupported overhangs are possible, though, and the maximum overhang angle depends on the material used and parameters. 45° is commonly viewed as the maximum achievable overhang angle.

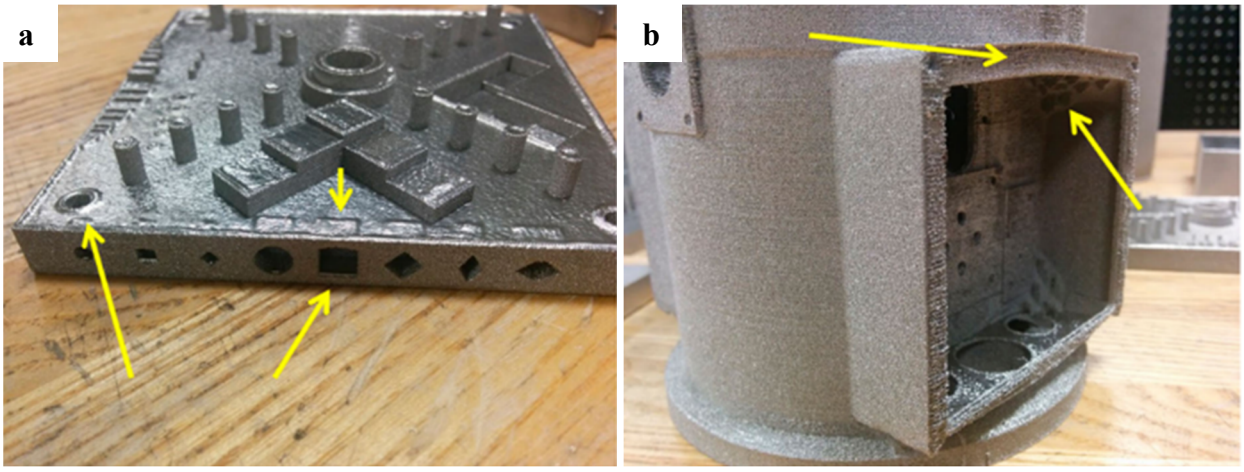

Figure 10. Examples of (a) swelling and (b) warping in PBF components [18]**.**

The third limitation in LPBF component design is anisotropic material properties. Columnar grain structure in LPBF systems has been well documented [40,41] and leads to anisotropic or transversely isotropic material behavior with the yield and tensile strengths typically being higher in the build direction (Z axis) [42]. Therefore, the build orientation, load path analysis, and LPBF limitations on overhangs must be considered simultaneously when designing components. The orientation of the component in the build chamber will determine the transversely isotropic property plane, and limitations on overhang angles preclude certain geometries. Designers can use geometries not possible with conventional manufacturing (particularly organic shapes, which can reduce stress concentrations) to redirect load paths in optimal ways. When properly accounted for and incorporated into a design, anisotropic behavior is not problematic as evidenced by the extensive use of fiber-reinforced composites with anisotropic properties. Recent work has focused on understanding and controlling the columnar-to-equiaxed grain transition [42–44] and describing the transition as a process map [45] to selectively form the grain structure of choice. The thermal history of an AM component is also important to consider when designing for critical applications. For example, if 10 tensile test specimens are fabricated individually and sequentially and removed from the machine when complete, the material properties will be different than had all 10 specimens been fabricated simultaneously. In the former case, the component will be built comparatively quickly and so experience a higher mean temperature. In the latter case, the time interval between layers for a given specimen will be greater because of the time spent melting other specimens, so more thermal energy will dissipate between layers. Depending on the alloy used and the desired phase or microstructure, this factor can be used advantageously to control microstructure.

Surface finish and minimum feature size are the fourth limitation in LPBF component design. Surface finish is generally a qualitative aspect of LPBF components but may be a major design consideration in the case of fatigue or internal gas or liquid channels in which pressure head losses are relevant. LPBF geometry resolutions in the range of 80 to 250 μm have been reported in literature [46] and depend on the laser spot size and geometric accuracy of the LPBF system.

2.2.4 Substrate and Powder Removal

After fabrication, components must have excess powder removed and are typically cut off build plates. LPBF components can be cleaned by brushing and vacuuming excess powder. Components are typically removed from build plates with electrical discharge machining (EDM) or bandsaws. Removing entrapped powder from channels and internal cavities can be challenging and cutting components off build plates presents handling difficulties for EDM and bandsaws designed for tubular and beam stock. Although not

technologically challenging, specialized support equipment is required for depowdering and build plate removal.

2.3 PROCESSING PARAMETERS

Processing parameters in LPBF can be grouped into (a) parameters of the LPBF machine and (b) post-processing parameters such as HIPing and heat treatments. Modeling and optimizing LPBF machine parameters is difficult because of the interconnectedness of outcomes and high dimensionality of independent variables. For example, optimizing for low porosity typically requires high energy input, which may result in larger grain sizes due to larger heat-affected zones (HAZs) of the melt pool. HIPing and heat treatments affect the microstructure of LPBF components in fairly predictable manners; however, the significant differences in starting microstructures between conventional and LPBF materials may necessitate the development of new heat treatments for LPBF rather than using existing heat treatments for conventionally manufactured materials.

2.3.1 Energy Density

Processing parameters specified during the file preparation phase dictate the laser's travel path, speed, power output, beam diameter, and other aspects of the fusion process. Depending on the manufacturer, LPBF systems require dozens to hundreds of parameters to be specified. Three parameters are commonly cited as critical in determining the thermal energy transfer to the melt pool: power, spot size, and scan speed. All three parameters are linked by the need to control the melt pool geometry and form fully dense components. Process mapping has emerged as a method of describing the power-speed relationship useful to PBF and other metal AM methods and is similar to welding process mapping [47]. One representative LPBF process map for maraging steel is shown in Figure 11 [48]. Some combinations of power and velocity are not viable because of melt ball formation and delamination as shown in Figure 12 [49]. Melt ball formation occurs because of melt pool instabilities when the surface tension of the melt pool exceeds the wetting ability of the previous layer [50]; melt balls result in fabrication failure due to interference with the rake and nonuniform layer formation. Delamination results from insufficient remelting of previous layers and will occur when the interlayer bonding strength is exceeded by thermally induced residual stresses. Delamination can be further influenced by high thermal gradients, incomplete melting, and grain boundary precipitate formation. Studies have particularly identified the importance of scan strategy [51] and applied energy input [52] in delamination occurrence. A recent study analyzed the effect of spot size by varying the focus plane in LPBF. For a constant wattage, out-of-focus beams resulted in larger spot sizes, lower power densities, and coarser columnar grains [53].

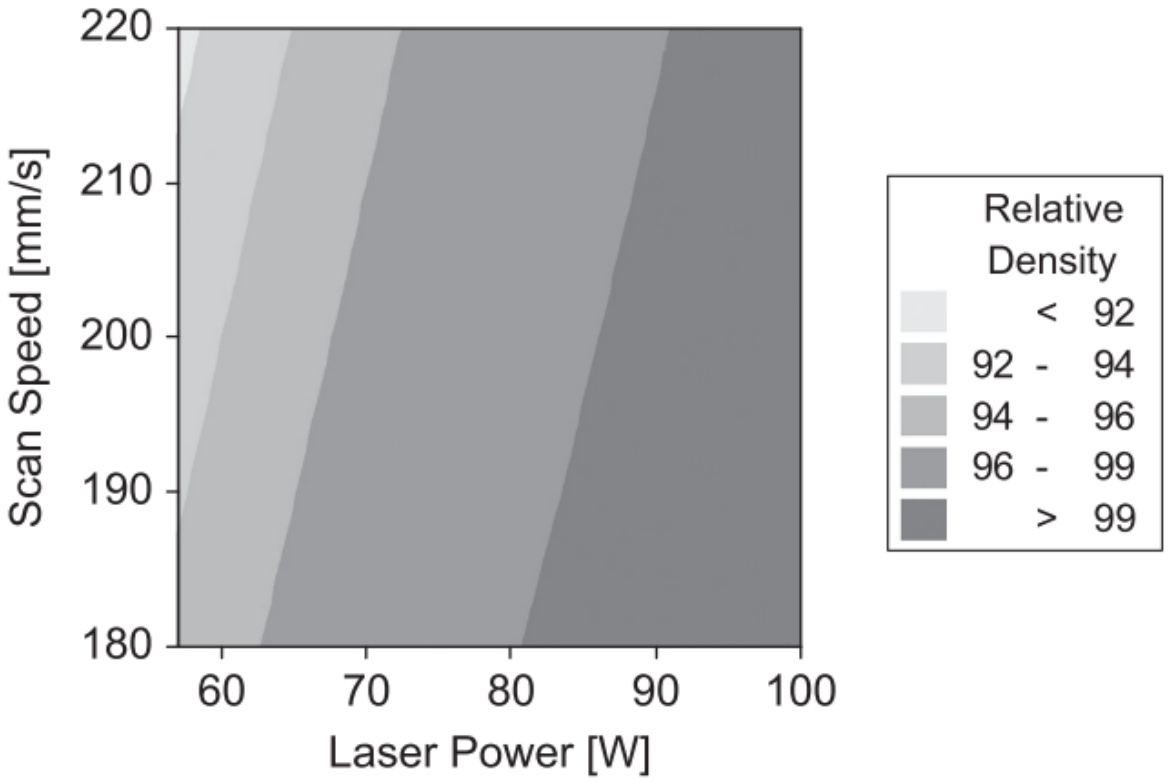

Figure 11. Example process map for LPBF [48]**.**

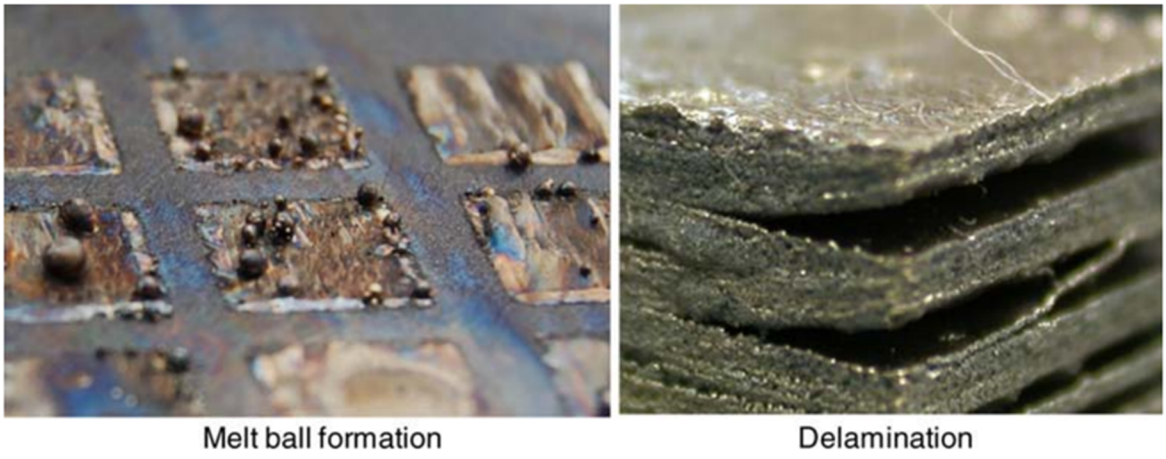

Figure 12. Fabrication failure examples due to power-speed relationships [49]**.**

Physics-based simulations can be used to estimate melt pool size [54,55], lack of fusion [54], keyholing [56–59], and solidified microstructures [60,61] to determine optimal LPBF parameters; simulations may be simplified approximations or precise models. “Lack of fusion porosity” refers to comparatively large irregularly shaped pores formed by insufficient overlap between layers or between hatch lines. “Keyholing porosity” refers to comparatively small pores that are typically spherical; keyholing is the result of gas bubbles trapped within solidified material. Such gas bubbles may be formed by residual feedstock porosity or localized boiling of the melt pool forming metal vapor cavities. Simulations offer valuable insights but suffer from computationally expensive methods (i.e., simulations taking days or weeks to run), deviation from empirical results, and a frequent lack of stochastic uncertainty. One active

area of research for reducing computational expense is multi-scale models; for example, when modeling the first melt pool track of a build the substrate and powder bed can be assumed to have a uniform background temperature. However, as the build progresses the substrate and component experience varying local "voxel" temperatures. A voxel is a cube inside the model that represents a discrete point in the component. The local voxel temperature is necessary to know when simulating the melt pool and for predicting precipitation, grain growth, and so on, but the rate at which voxel temperatures near (10s to 100s of microns) the melt pool change is significantly higher than far (1,000s of microns) from the melt pool. Therefore, a need exists for models that update voxels close to the melt pool at one frequency and far from the melt pool at a different frequency to reduce computational expense. Determining the distances and frequencies at which different voxel regions can be updated without losing significant model accuracy is an ongoing area of research. One method that has been explored to address the above-mentioned shortcomings of simulations is to iteratively use simplified approximations with quick experimental layouts [62]. Such an approach reduces development time, reduces the number of experimental samples that must be prepared relative to a purely empirical approach, and provides stochastic uncertainty data for models. Overall, simulations can identify regions of nominally "good" parameters for simple geometries but are not well suited for precise parameter fine-tuning or for modeling of complex or large components due to prohibitive computational expense.

2.3.2 HIPing and Heat Treatments

HIPing is a method in which components are heated in the presence of a high-pressure inert gas environment to close internal pores [63]. Internal cracks may also be remediated by HIPing as demonstrated in LPBF-fabricated Ni superalloy components but surface-connected cracks remain after HIPing [31]. The high temperatures of HIPing also facilitate grain growth in some materials. Inconel 718 deposited on an Inconel 718 substrate via LPBF and subsequently post-processed with HIPing was observed to result in grain growth in the substrate but not the deposited material [64]; differences in phases or grain boundary precipitates may have caused the variation in response to HIPing. If so, appropriate characterization or homogenization of deposited material prior to HIPing may be necessary to achieve consistent responses.

The effects of HIPing and heat treatment combinations on Ni superalloys [65–75], Ti alloys [76–78], Al alloys [79], and steels [80,81] have been reported in literature, and data on the effects of HIPing on porosity and elongation at failure are shown in Table 2. The difference in YS and UTS between as-fabricated and HIPed samples due to grain size cannot be directly correlated because of the often-significant effects of phase transformations and precipitation; however, Young's modulus is usually negligibly affected by HIPing. Porosity and internal cracks are typically reduced by an order of magnitude in volume. Treatment times as short as 4 min have been shown to reduce porosity as significantly as 3 to 4 h treatments [74], suggesting that lengthy treatments are unnecessary to reduce porosity. Studies that heat-treated (HT) after HIPing reported negligible variation in porosity between post-HIPing samples and post-HIPing + HT samples [68], indicating that porosity reduction is permanent. Elongation at failure has been reported to improve by 30 to 200% with HIPing, but ductility may not improve in cases in which highly brittle phases are formed as a result of the HIPing temperature profile. Fatigue resistance increases with HIPing because of the reduction in internal crack nucleation sites but is similarly difficult to compare because of thermal effects on grain size and phase formation for each alloy system.

Table 2. Effects of HIP on porosity and elongation at failure for PBF components.

Material	HIP pressure (MPa)	HIP temperature (°C)	HIP time	Pre-HIP porosity (%)	Post-HIP porosity (%)	Pre-HIP elongation (%)	Post-HIP elongation (%)	Ref.

H13 tool steel	100	1,130	6 hr	0.11	0.005	3.3 ± 1.6	6.6 ± 0.6	[81]
Hastelloy X	103	1,160	4 hr	0.29–0.34	<0.1	—	—	[69]
Inconel 718	120	1,200	4 hr	—	—	6 ± 1	14 ± 1	[68]
Inconel 718	102	1,160	3 hr	0.48–1.35	0.01	—	—	[70]
Inconel 718	150	1,180	3 hr	0.27	0.06	21 ± 5	34 ± 3	[72]
CMSX-4	100	1,300	4 min	0.607	0.061	—	—	[74]
CMSX-4	100	1,315	4 min	0.607	0.074	—	—	[74]
Ti-6Al-4V	100	920	2 hr	0.97	0.10	13.6 ± 1.4	17.7 ± 0.9	[77]
Inconel 718	120	1,200	4 hr	0.70	0.05	—	—	[75]

2.4 MICROSTRUCTURE AND MECHANICAL PROPERTIES

Meaningful comparison of literature results is complicated by the significant number of fabrication parameter variables and incomplete reporting in literature. For example, absorptivity of Fe varies from 0.12 at room temperature for a CO_2 laser to 0.25 to 0.32 for a Nd:YAG (neodymium-doped yttrium aluminum garnet) laser [82]. Therefore, reporting both applied power and laser wavelength is necessary to calculate absorbed energy, yet laser type is not consistently reported. Similarly, spot size, hatch spacing, layer thickness, build orientation, and material porosity are not consistently reported yet are required for accurate parameter comparison and calculation of thermal history. Incomplete reporting can be partially attributed to three causes: (1) non-standardized terminology within the LPBF community, (2) inter-supplier variation in hardware and software, and (3) a lack of reporting standards. Uncertainty in interpreting results is further complicated by the influence of geometry as an independent variable, and the lack of accepted standardized geometries frequently leads to unique geometries for each study. Therefore, interpretation of quantitative results in LPBF material properties should be more skeptical than typical for scientific endeavors.

Four alloy groups have seen significant use in metal AM to date [8,83,84]: titanium alloys [8,85–87], steels, Inconel alloys [42,88], and aluminum alloys [89,90]. Specific steel classes used in AM include austenitic stainless steels [91], tool steels [92], precipitation hardenable stainless steels [93], and maraging steels [48]. General reviews on the hardness of AM metals [94], the effect of build orientation [95], and anisotropic material properties [96] have been published. Key issues for each system are briefly reviewed in this section; however, the study, prediction, and control of microstructure of metal AM processes encompasses a vast field of research because of the high number of combinations of processing methods and alloy designs. The primary focus of the material property review is on LPBF 316L given the application in NPP environments and well-documented reference performance of conventionally manufactured 316L in irradiated environments.

Additively manufactured metallic components frequently have comparable if not superior properties to conventionally manufactured parts, partially due to fine grain sizes [8]. LPBF essentially welds layers together and the small (50 to 500 μm) spot size of the energy source results in small melt pools and rapid cooling, which inhibits grain growth upon solidification. Columnar grain structures oriented lengthwise in the build direction (Z axis) are frequently observed in LPBF, and this grain structure has been reported in Ti-6Al-4V [97] and Inconel 718 [98–100]. Grain structures primarily depend on the temperature gradient and solidification interface velocity, and selectively forming columnar or equiaxed grains is possible by varying the energy source power and scan speed [101].

Reviews of the tensile properties of additively manufactured Ti-6Al-4V have been conducted [12,102] and numerous articles have been published on the subject [103–110]. In general, the reported Young's modulus, YS, and UTS of PBF Ti-6Al-4V are comparable to wrought Ti-6Al-4V whereas reported ductility varied significantly. Reviews of Ti alloy fatigue behavior [111] reveal strong relationships between fatigue strength and the method of powder production. Ti and its alloys are highly reactive with oxygen, and processes that form powder in a vacuum, such as plasma rotating electrode process, result in lower oxide content powders. LPBF of Ti forms a martensite phase with decreased ductility due to rapid solidification and cooling and, therefore, stress relief and phase transformation heat treatments are typically required for components with cyclical stress loads [112]. However, careful LPBF parameter choice has been reported to produce as-fabricated Ti-6Al-4V without martensite [113].

Commonly used Ni alloys in AM include Inconel 718, Inconel 625, and Invar 36. The first two alloys are used in the aerospace industry because of their strength retention at high temperatures [114]. Mechanical properties of Ni-based alloys have previously been reviewed and are listed in Table 3 [115]. Although clear relationships between transverse and longitudinal ductility or UTS and ductility for LPBF Ni alloys have not been reported, an expression has been developed [116] for estimating hardness given the elemental composition of a Ni alloy as shown in Eq. 1 [117]. Experimental results of hardness vs. Ni equivalent are plotted in Figure 13 [115]. Comparable hardness analysis for aluminum and steel alloys have been conducted [116].

Table 3. Summary of mechanical properties of Ni-base alloys fabricated by AM in literature compared with traditionally processed counterparts [115].

Alloy	P (W)	v (mm/s)	H (J/mm)		Orientation	E (GPa)	σ_y (MPa)	σ_{uts} (MPa)	Elongation (%)	HV
Powder bed fusion – laser heat source										
Invar 36	400	1800–4300	0.22	As-deposited	Long.		400	535	14	
					Transv.		340	455	30	
				HT	Long.		311	447	32	
Inconel 625	200	800–1200	0.25	HIP	Long.		380	900	58	347
					Transv.		360	880	58	296
Inconel 625	50	130	0.38	As-deposited	Long.	202.24 ± 4.12	800 ± 20	1030 ± 50	8–10	
					Transv.	140.66 ± 8.67	1070 ± 60	720 ± 30	8–10	
Haynes 230	200	450–1200	0.44	As-deposited	Long.	205 ± 4	798 ± 5	1102 ± 6	28 ± 1	
					Transv.	152 ± 1	656 ± 4	941 ± 2	32 ± 3	
Powder bed fusion – electron beam heat source										
Inconel 625	1800	10^4	0.18	As-deposited	Transv.		410	750	44	224
				HIP	Transv.		330	770	69	
Directed energy deposition – powder feedstock										
Inconel 718	–	–	–	As-deposited	Long.		650	1000	38% (Reduction in area)	
				HT	Long.		1257	1436	13% (Reduction in area)	
				HT+ HIP	Long.		1155	1380	20.4% (Reduction in area)	
Inconel 718	2350	8	294	As-deposited	Long.		590	845	11	
				HT	Long.		1133	1240	9	
					Long.		1170	1360	18	
Directed energy deposition – wire feedstock										
Inconel 625		5		As-deposited	Long.	180		722 ± 17	42.27 ± 2.4	240–270
					Transv.			684 ± 23	40.13 ± 3.7	
Inconel 718		5		As-deposited	Long.	154 ± 1	473 ± 6	828 ± 8	28 ± 2	
Inconel 718				As-deposited	Long.	163	666	1022	26.1	
				HT	Long.	24.1	947	1242	23.5	
				HT	Long.	25.8	932	942	22.2	
Traditionally processed										
Inconel 718	Cast - typical						915	1090	11	266 (max)
	Annealed and Aged - minimum						862	1034	20	318
Inconel 625	Cast - typical						350	710	48	266 (max)
	Annealed - typical						430	940	51.5	145 (min)
Invar 36	Cast - typical						265	483	44	–
	Annealed - typical						260	470	37	131

$$\varphi = \mathrm{Ni} + 0.65\mathrm{Cr} + 0.98\mathrm{Mo} + 1.05\mathrm{Mn} + 0.35\mathrm{Si} + 12.6\mathrm{C} - 6.36\mathrm{Al} + 3.80\mathrm{B} + 0.01\mathrm{Co} + 0.26\mathrm{Fe} + 7.06\mathrm{Hf} + 1.20\mathrm{Nb} + 4.95\mathrm{Ta} + 5.78\mathrm{Ti} + 2.88\mathrm{W} \quad (1)$$

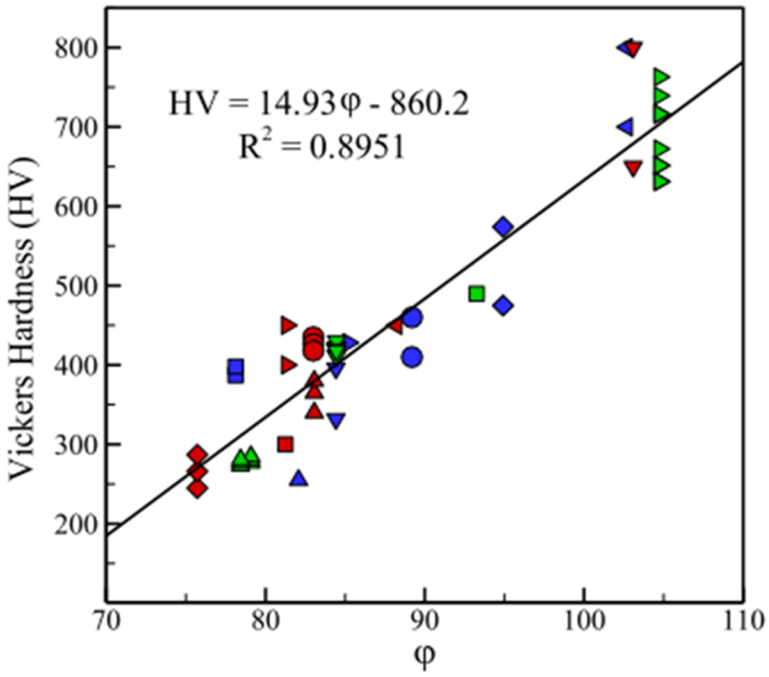

Figure 13. As-deposited Vickers Hardness (HV) as a function of nickel equivalent [115].

2.4.1 Properties of LPBF 316L

316L is commonly used in light water reactors for structural components; austenitic stainless-steel alloys—particularly 316, 316L, 304, and 304L—have been considerable researched in LPBF systems, but relatively little research on irradiated LPBF austenitic stainless steels has been published to date. All four alloys form delta ferrite and gamma austenite [118,119] as predicted by the relevant phase diagram in Figure 14[120]. Residual ferrite can be post-processed to austenite with solution heat treatments between 850 and 1,250°C [120,121], which is desirable for NPP applications because ferrite is a thermodynamically unstable phase, susceptible to void swelling under radiation damage, and a major contributor to alloy embrittlement [121,122]. Ferrite decomposes to the σ phase, a brittle intermetallic, and austenite upon aging. The σ phase is undesirable not only because of brittleness but also because it reduces grain boundary Cr content in the remaining austenite. Low-Cr grain boundaries then act as nucleation sites for SCC. Experimental results indicate that irradiation-assisted SCC (IASCC) can be reduced via reduction in grain size [123]; therefore, heat treatments should be kept as brief and low-temperature as possible to minimize grain growth. One additional consideration for metal AM stainless materials is that the presence of a small amount of oxygen forms disperse oxide precipitation in the matrix, which alters grain growth and hardness evolution during tempering [124]. One study of LPBF 316L reported to have achieved significantly smaller grain sizes (5 to 16 μm vs. 50 μm) than conventional 316L when solution HT at 1,100°C for 1 h [125]. Therefore, LPBF components may have comparatively high yield and tensile strengths due to grain size refinement even though not hot-worked; higher dislocation densities due to rapid solidification and residual stress also affect material properties [118,126–128].

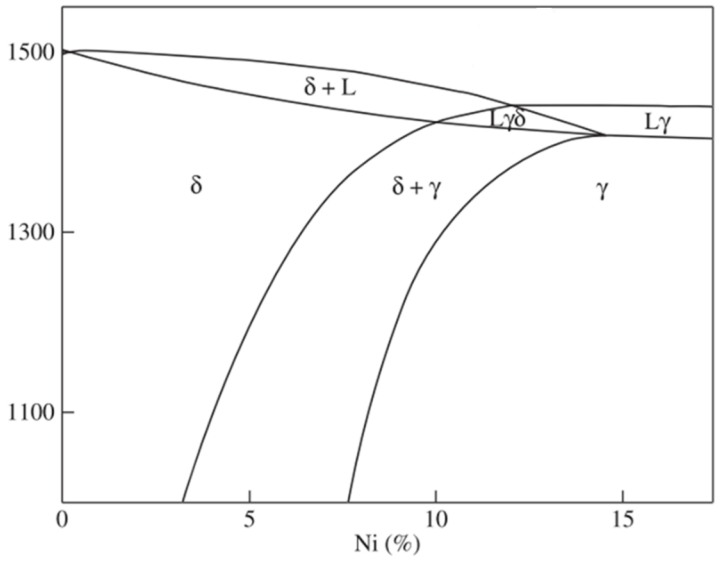

Figure 14. Phase diagram for 18 wt % Cr austenitic stainless steels [120]**.**

Tensile properties of LPBF 316L have been reported in literature [129–132]; in general, austenitic stainless steels fabricated by LPBF show slight anisotropy in material properties, and elongated grains and dendrites oriented in the Z axis are often observed [119,126,127,132,133]. YS and UTS are often higher than in conventionally manufactured and annealed austenitic stainless steels whereas elongation at failure is decreased. It is not clear whether the decreased ductility is due to porosity and internal defects or smaller grains leading to dislocation buildup at grain boundaries [119,126,130,134]. Variation in tensile properties due to part orientation has been reported at 555 to 738 MPa for UTS, 508 to 718 MPa for YS, and 20 to 47% for elongation at failure [129]. For comparison, ASTM F3184 - 16 "Standard Specification for Additive Manufacturing Stainless Steel Alloy (UNS S31603) with Powder Bed Fusion" specifies minimum requirements of 207 MPa for YS, 517 MPa for UTS, and 30% for elongation at failure for LPBF 316L. ASTM A276 - 17 "Standard Specification for Stainless Steel Bars and Shapes" specifies 310 to 515 MPa for YS, 550 to 655 MPa for UTS, and 25 to 30% for elongation at failure for conventionally manufactured cold-rolled 316L depending on size. Table 4 provides an overview of LPBF 316L tensile properties from literature.

Table 4. Tensile properties of 316L from literature.

Reference	[129]	[130]	[131]	[132]
UTS (MPa)	555–738	567–659	493–630	317–528
YS (MPa)	508–718	444–534	—	287–438
Elongation at failure (%)	20–47	8–16	—	7–23
Variable of study	Orientation	Orientation	Preheating vs. room temperature	Processing parameters
Note	—	High (2.5–6.2%) porosity	—	High (1.5–8.8%) porosity

The fracture toughness of LPBF 316L has not been thoroughly studied to date, and multiple publications lack critical details such as porosity, porosity measurement method, and processing parameters (i.e., proprietary parameter combinations) [135–138]. To the authors' knowledge, only one published LPBF

316L fracture toughness study [138] has presented results on HT (HIP + solution HT) LPBF 316L. Tabulated fracture toughness results are presented in Table 5. Results to date suggest as-fabricated LPBF 316L has ~40% lower fracture toughness relative to conventional annealed 316L; HIP + solution HT LPBF 316L has ~50% higher fracture toughness than conventional annealed 316L. As-fabricated fracture toughness varies ~14% because of part orientation, and toughness appears to have a strong negative correlation to porosity. The exact relationship between porosity and fracture toughness has not been quantified as of this document's publication. Although replicate studies are needed to confirm repeatability and quantify variance, LPBF 316L may offer comparative fracture toughness values relative to conventional 316L given careful selection of processing parameters and heat treatments.

To the authors' knowledge, no irradiated LPBF 316L fracture toughness results have been published to date. As reported in ref. [138], GE Hitachi has planned experiments to irradiate and obtain fracture toughness results in collaboration with Idaho National Laboratory; however, a timeline was not provided. DOE's Oak Ridge National Laboratory's (ORNL's) Transformational Challenge Reactor Program does not anticipate irradiating any fracture toughness specimens in 2020.

Table 5. Fracture toughness values for LPBF 316L from literature.

Study	[135]	[136]	[136]	[137]	[138]	[139]
Machine	M1, Concept Laser	Mlab Concept Laser	AM250, Renishaw	M270, EOS	M290, EOS	Irradiated (0–10 dpa) conventional 316L/304L reference
Processing parameters	180 W power 1,600 mm/s velocity 30 μm hatch spacing 75 μm spot size	Not provided	Not provided	175–190 W power 800 mm/s velocity 40 μm layer thickness	Not provided	
Variable	Orientation	Orientation	Orientation	Power, orientation	None	
Porosity	~4%	0.07–0.35%	~2.5%	Not provided	Not provided	
Heat treatment	As-fabricated	As-fabricated	As-fabricated	As-fabricated	HIP + solution	
Fracture toughness	145–176 MPa $m^{1/2}$	124–144 J	20–28 J	54–140 J/cm^2	387–429 MPa $m^{1/2}$	70–250 MPa $m^{1/2}$

Fatigue properties of LPBF austenitic stainless steels has been reported in literature in both original studies [140,141] and reviews [142]. Riemer et al. [140] reported that fatigue limit and crack growth rate strongly depend on heat treatment in 316L for cracks growing perpendicular to the build plane (i.e., the X-Z or Y-Z planes) but not for cracks growing parallel to the build plane (i.e., the X-Y plane). Figure 15 illustrates how fatigue cracks grow through columnar grains in the X-Z plane but between grains in the X-Y plane for as-fabricated and stress-relieved 316L, providing a mechanistic explanation for the observed difference in fatigue limit and crack growth rates from orientation. HIPed, and presumably solution HT, LPBF 316L has enlarged relatively equiaxed grains and therefore exhibits fatigue crack growth more similar to conventionally manufactured material. Fatigue limit and crack growth rates for 316L with stress relief and HIP heat treatments are presented in Figure 15 and Figure 16 [140]. Spierings et al. [141] reported fatigue endurance limits of 200 to 270 MPa (R = −1) for un-HT 316L in the X-Y plane for various surface finishes, the results of which are presented in Figure 17[141]. The observed range of LPBF 316L endurance limits compared favorably with conventional 316L endurance limits of 141 to 207 MPa under a less demanding cycle mean load of R = 0.1. The same mechanism of crack growth through grains rather than at grain boundaries reported by Riemer et al. may be the driving force for the higher endurance limits observed in LPBF 316L. Unfortunately, neither study reported porosity levels or pore morphologies in fabricated components.

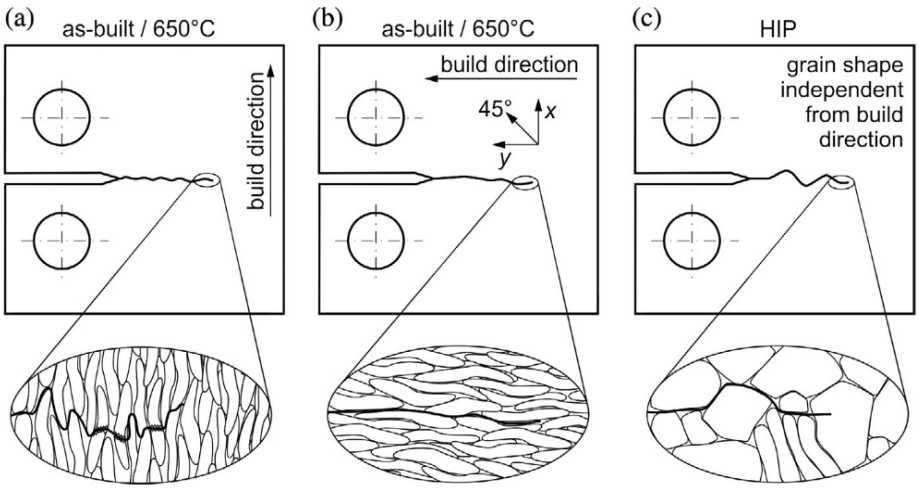

Figure 15. Interactions of fatigue crack growth with grain boundaries in LPBF 316L for (a) stress-relieved with crack growth parallel to build plane, (b) stress-relieved with crack growth perpendicular to build plane, and (c) HIPed parts [140].

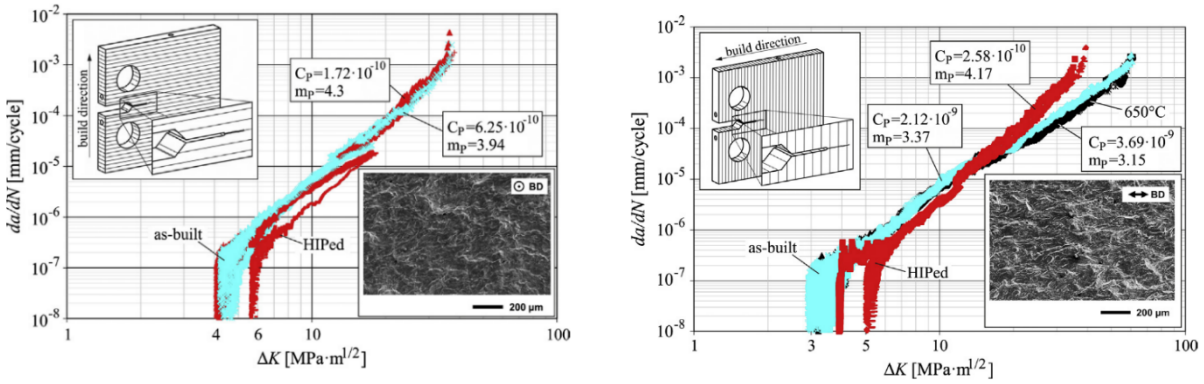

Figure 16. Fatigue crack growth rates in the (a) X-Y and (b) X-Z planes for LPBF 316L [140].

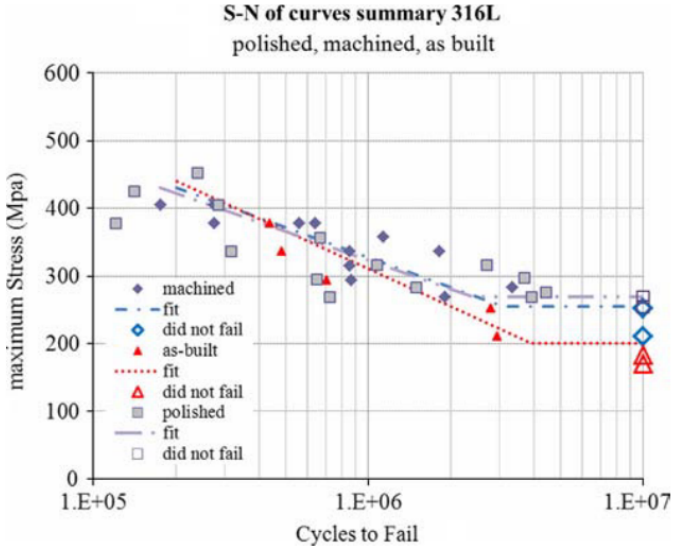

Figure 17. Fatigue limits of LPBF 316L for various surface finishes [141].

The effects of surface roughness on the fatigue life of LPBF 316L have been reported [143–145]. Blinn et. al. [143] observed high sensitivity to surface roughness in stress-relieved unpolished samples with high cycle ($>10^5$) fatigue and low sensitivity with low cycle (10^4) fatigue. Shrestha et. al. [145] reported significantly higher scattering in low cycle lifetimes in machined specimens relative to as-fabricated specimens. This unexpected result was postulated to be caused by an internal lack of fusion pores being exposed to the surface via turning and polishing. Solberg et. al. [144] fabricated fatigue specimens with ~5% porosity and observed a transition in crack nucleation sites from internal pores in low cycle lives to external surface roughness in high cycle lives at ~10^5 cycles. Taken as a whole, the fatigue lives of LPBF components appear to be predictable using existing fatigue testing methods for a given processing parameter, post-processing treatment, and surface roughness. As reiterated elsewhere in this document, all testing specimens should be sourced from final component geometries because grain size and orientation affect crack growth rate, and geometry and heat transfer characteristics directly affect grain size and orientation.

A literature search on corrosion-related crack propagation in LPBF 316L, cyclic or constant load, revealed few published studies. One notable study on SCC by GE Global Research [146] (republished in [147]) evaluated stress relief vs. HIPing + solution annealing heat treatments for LPBF 316L. Crack growth in stress-relieved LPBF 316L was preferential along the build direction (Z axis) and approximately two times higher in the build direction than in annealed conventional 316L, qualitatively mirroring fatigue behavior. However, when cracks grew perpendicular to the build direction and thus through grains rather than along grain boundaries, the crack growth rate was comparable to annealed conventional material. HIPed + solution-treated LPBF 316L was observed to have comparable SCC crack growth rates to annealed conventional 316L, and the crack growth mode in HIPed + solution-treated LPBF 316L was along grain boundaries. Post-SCC fracture surfaces of HIPed + solution-treated specimens revealed a significant frequency of corroded pits with diameters of ~500 to 1,500 nm. Corroded material within the pits was identified to be rich in chromium and oxygen but deficient in iron, nickel, and silicon. Inclusions at the crack tip that had not yet been corroded were identified to be rich in silicon. Figure 18 [146]depicts corroded pits on SCC intergranular fracture surfaces of LPBF 316L. Si-, Mn-, Cr-, and O-rich nanoscale inclusions have been reported in non-HT LPBF 316L in other studies [148]. In summary, the SCC crack growth rate of LPBF 316L appears to highly depend on the heat treatment and may be accelerated by oxide inclusions.

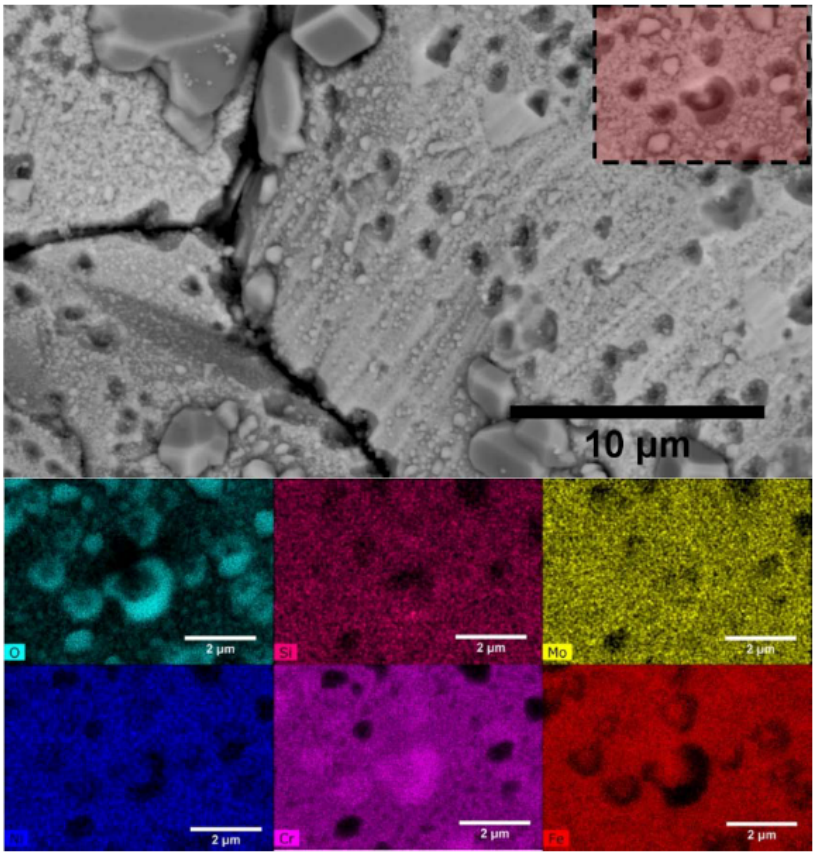

Figure 18. Intergranular fracture surface of SCC LPBF 316L with corroded pits [146]**.**

Rebak et al. [146] present compelling information that Si-rich inclusions at grain boundaries in LPBF 316L contribute to accelerated SCC growth rates but that the crack growth may be moderated to rates comparable to conventional 316L via heat treatments. However, information lacking from the GE study presents gaps that must be addressed. Chemical composition of the conventional annealed control specimens was not published, nor were fractography images of conventional control specimens. Rebak et al. state that few inclusions were observed in the conventional control specimen but do not quantify the inclusions (e.g., counts per square millimeter) or provide chemical composition information on the few inclusions observed in the conventional control specimen. Spatial distribution information on Si inclusions in the LPBF specimens was also not published (e.g., proximity to grain boundaries, clusters vs. uniform distribution, line patterns). Therefore, several pertinent questions must be addressed to understand and minimize SCC in LPBF 316L.

First, the root cause of Si inclusion formation in LPBF 316L components must be identified. Considering that a high frequency of Si rich inclusions was not observed in the conventional control specimen and inclusions of this type have not been widely reported in conventional 316L [149] even though the powder feedstock used was within ASTM F3184 - 16 composition specifications, the authors conclude that Si inclusions result from phenomena within the LPBF process or preceding feedstock production processes. Cross-sectional analysis of powder feedstock may help determine whether Si inclusions are present in feedstock material. Regardless of the cause of formation, limiting Si inclusion formation may be possible by specifying ultralow Si content in powder feedstock. Eliminating Si as a primary oxygen scavenger may result in other oxide species forming, which may then need to be evaluated for susceptibility to corrosion in light water reactor conditions.

Second, the spatial distribution of Si inclusions relative to grain boundaries in the as-fabricated/stress-relieved and HIPed/solution-treated states must be quantified. If inclusions are present in powder feedstock, simulation of LPBF Marangoni convection currents within the melt pool may provide insight as to the distribution of inclusions after melt pool solidification. Empirical observation of inclusions relative to grain boundaries may reveal whether inclusions preferentially align with grain boundaries in the as-fabricated state as well as how recrystallization due to HIPing/solution heat treating affects the concentration of inclusions at grain boundaries. If Si inclusions at as-fabricated LPBF grain boundaries are sufficiently reduced, HIPing and/or solution heat treating post-processing may be eliminated, making only stress relieving possible. Not only would significant cost savings be realized, but also, LPBF components would be limited in size by the volume of the LPBF machine rather than the volume of the HIP chamber.

Corrosion fatigue crack growth of LPBF 316L was also evaluated in the GE study [146] and post-processing heat treatments were observed to affect crack growth rates as illustrated in Figure 19 [146]. In all cases, LPBF 316L was observed to have higher crack growth rates than conventional 316L at low stress amplitudes and crack growth rates comparable to conventional 316L at higher stress loads. To the authors' knowledge, GE's work [146] is the only published study to date on corrosion fatigue in light water reactor simulated environments.

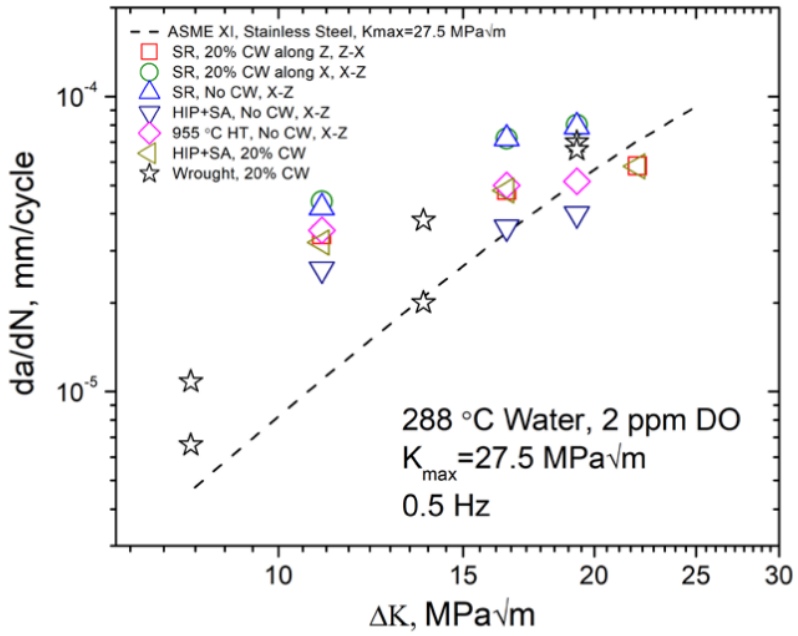

Figure 19. Corrosion fatigue crack growth rates in LPBF 316L for various heat treatments [146]**.**

2.4.2 Properties of Irradiated LPBF 316L

The effects of irradiation on LPBF 316L microstructures and material properties are currently unclear. Several recent studies have presented results on irradiated additively manufactured 316L discontinuities [146,148,150–153], including stress relieved [146,152], solution HT [151], and HIPed [146,152] samples. Comparisons of loop densities in the X-Y vs. Y-Z planes [152] and the effects of vertical vs. horizontal sample orientation [150] have been published. Quantitative comparisons from one study to another are not possible because of the significant differences in processing parameters, radiation doses, and lack of processing parameter documentation, and no one study encompasses all three heat treatments (as-

fabricated, stress-relieved, solution-treated/HIPed). Table 6 lists the documentation available for references on irradiated LPBF 316L properties.

Table 6. Documentation in irradiated LPBF 316L references. X indicates data is available

Reference	[153]	[152]	[151]	[150]	[148]	[146]
Laser power (W)	—	195	195	195	200	195
Laser velocity (mm/s)	—	1,200	1,083	1,200	850	1,200
Laser spot size (μm)	54	—	—	—	70	—
Hatch spacing (μm)	—	—	90	90	100	—
Layer thickness (μm)	—	20	20	—	—	20
Powder size data	—	X	X	X	—	X
Powder chemistry data	—	—	X	—	—	—
Conventional control sample	X	X	—	X	—	X
Radiation dose (dpa)	5.5	2.5	50–100	80	—	2.5, 100
Radiation method	Kr++ ions	Proton	Fe2+ ions	Fe2+ ions	He ions	Proton, self-ion

Qualitative interpretations of the sources in Table 6 and GE's study suggest that LPBF has the potential to significantly improve the resistance of 316L to void swelling. The formation of cellular sub-grains inside crystals in as-fabricated LPBF 316L samples has been reported to reduce the buildup of dislocation loops by as much as 60% [148,153] relative to conventional 316L, and the sub-grains are reported to be stable after 30 min at 400°C [153]. However, GE's study reported an order of magnitude higher dislocation loop density in stress-relieved LPBF 316L relative to conventional 316L [146] as summarized in Table 7[146]. Another study has reported as-fabricated LPBF 316L having significantly lower resistance to void density and void swelling buildup relative to solution HT LPBF 316L and fully recrystallized LPBF 316L [151]. Etched optical images of as-fabricated 316L samples with superior resistance to defect buildup are presented in Figure 20 (a) and (b) [148]and indicate grains characterized by submicron cellular sub-grains. . If sub-grain formation is a significantly beneficial mechanism in improving the resistance of LPBF 316L to irradiation defect damage, and then geometry-processing parameter combinations that produce fine sub-grain distributions and post-processing treatments that do not eliminate sub-grains are desirable and potentially result in superior performance relative to conventionally manufactured 316L. At the time of this publication, the inconsistencies in trends between irradiated microstructure studies cannot be resolved because of the limited number of studies published, incomplete reporting of processing parameters, and lack of overlap in evaluated heat treatments.

Table 7. Effect of proton irradiation on 316L at 2.5 dpa.

Alloy ID	Dislocation loops			γ′ precipitates			Voids		
	d(nm)	$\rho(10^{22}/m^3)$	$L(10^{14}/m^2)$	d(nm)	$\rho(10^{21}/m^3)$	fv(%)	d(nm)	$\rho(10^{21}/m^3)$	S(%)
SR AM 316L	18.9±9.0	4.7±1.9	8.9	6.2±2.5	5.5±3.1	.07	6.6±1.6	3.1±1.2	.047
HIP AM 316L	20.2±10.4	1.5±0.7	3.0	6.6±2.4	2.9±1.7	.04	8.4±2.0	0.08±0.04	.0025
Forged 316L	32.6±22.0	0.32±0.12	3.3	7.8±2.5	2.2±1.4	.06	19.5±4.9	0.34±0.19	.156

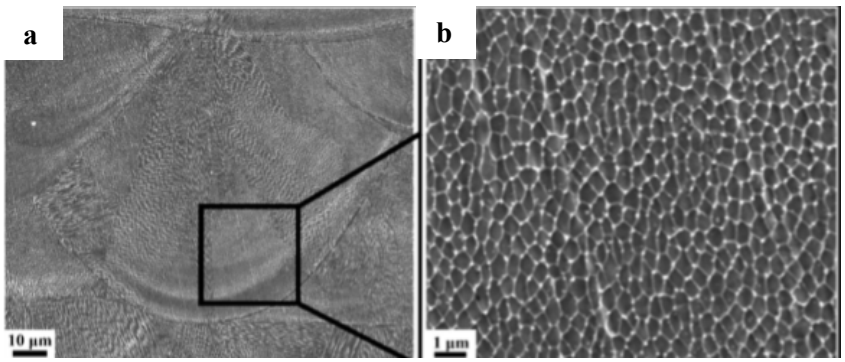

Figure 20. (a) SEM image of melt pool outline; (b) SEM image of crystal sub-grains from [148]**.**

IASCC in LPBF 316L has been minimally studied at the time of this publication. Only one published study was found [152] which uses the same data as the GE study [146]. Using the same stress relief and HIP + solution heat treatments as for ref. [146], LPBF 316L was proton irradiated to 2.5 dpa and strained under boiling water reactor normal chemistry solutions to 4% strain at a constant rate of 10^{-7}/s. The results are listed in Table 8 and graphically displayed in Figure 21 [152].

Table 8. IASCC crack statistics for LPBF 316L [152].

Alloy	Area	No. crack	Average crack length (μm)	Crack density (#Cracks/mm^2)	Crack length/unit area (Avg length x density) (μm/mm^2)
HIP AM316L	UIA	0	0	0	0
	IA	0	0	0	0
SR AM316L//PD	UIA	0	0	0	0
	IA	1	6.1	1.04	6.35
SR AM316L$^{\perp}$PD	UIA	0	0	0	0
	IA	35	7 ± 1	38 ± 0.2	272 ± 27
Forged 316L	UIA	0	0	0	0
	IA	50	9 ± 2	38 ± 1	342 ± 46

In contrast with unirradiated SCC, HIPed + solution-treated LPBF 316L demonstrated remarkably superior performance to conventional 316L with no observed cracks in the HIPed + solution-treated specimen. Stress-relieved LPBF 316L pulled perpendicular to the print direction had comparable crack densities and smaller average crack sizes. Qualitatively, the observed performance in IASCC crack resistance appears to mirror the volume void swelling percentage. Although more studies are needed to evaluate IASCC for isostatic stress rather than isostatic strain and to evaluate the effect of LPBF Si-inclusion-free microstructures, microstructures produced via LPBF may offer comparable or superior tensile, fatigue, SCC, and IASCC properties relative to conventional 316L given appropriate heat treatments.

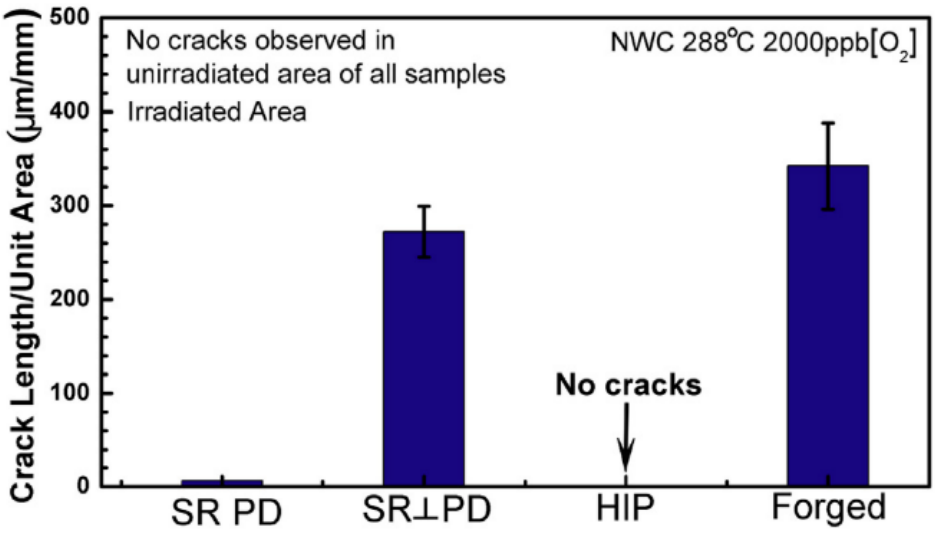

Figure 21. LPBF 316L IASCC crack length comparison [152]**.**

3. GAP ANALYSIS

AM is transitioning from laboratory experiments to industrial mass production of components. Many LPBF components will be required to conform to a quality assurance (QA)/QC process to ensure a minimum confidence level in component performance. However, as LPBF is transitioning to industrial usage, many pertinent standards are underdeveloped or do not exist. Best practices and standard operating procedures for machine calibration and process control must similarly be developed. This section discusses the gaps between existing requirements and requirements necessary for statistically repeatable and predictable performance; the section consists of four subsections—prefabrication, during fabrication, post-fabrication, and gaps in codes and standards.

3.1 PREFABRICATION

Requirements and challenges for the prefabrication LPBF processes can be grouped into three primary categories: software, the powder sieving system, and the LPBF machine. Each exhibit unique challenges and are reviewed in depth in the following sections.

3.1.1 Software

Software requirements in LPBF applications can be organized into three categories: file preparation, scan strategy-geometry interactions, and accurate thermal simulations. The current generation of proprietary LPBF vendor software packages frequently allows users to unintentionally commit errors in preparing CAD files and assigning laser scan strategies to each part. Interactions between scan strategy parameters and component geometry can result in variable melt pool sizes and local component temperatures, resulting in heterogeneous microstructures and therefore heterogeneous material properties. Difficulties arising in multiphysics simulations of the LPBF process and potential solutions are also discussed.

3.1.1.1 File Preparation

ORNL staff have identified four sources of uncertainty in LPBF file preparation: path independence in file preparation, tessellation, layer thickness/slicing interactions, and “ghost” parts. Additional

unidentified complications and sources of uncertainty may exist at the time of this document's publication. Components are first modeled in engineering CAD software packages such as SolidWorks or Autodesk and saved as ".STL" files. The STL file is then loaded into a "slicing" software package and separated into sequential layers as described in Section 2.2.2. Finally, each layer is assigned a scan strategy by proprietary LPBF vendor software packages, after which the completed file is transferred to the LPBF machine. "Path independence" refers to different laser scan strategies generated by user input paths. For example, a user could model and prepare a build with ten standard ASTM E8 tensile specimens by (a) loading and slicing the tensile bars one at a time sequentially, (b) loading and slicing batches of five tensile bars, or (c) loading and slicing all ten tensile bars at once. ORNL staff have observed some manufacturers' software packages to handle slicing and generating the laser scan path differently depending on the order in which parts are virtually modeled and the number of parts sliced. In other words, in the tensile bar example, the laser scan strategy for case (a), (b), and (c) may not be identical and may therefore result in non-negligible variations in porosity, microstructure, and material performance. Therefore, the only way to guarantee laser scan strategy consistency between replicate builds is to use the same sliced build file. Identical comparisons of the same part when not replicating builds (for example, comparing fabricating two copies of a part in a build vs. ten copies in a build) is more difficult and requires using the same procedure when modeling and slicing components.

Tessellation is the result of converting organic or curved surfaces into polygons. When the polygon count is low, the modeled component will appear blocky and may not meet dimensional tolerance specifications as illustrated in Figure 22 [154]. As a user increases the polygon count, the model asymptotically approaches the curvature of the organic shape at the expense of file size and computer RAM requirements. At the time of this publication, tessellation is not a routine issue encountered in LPBF as tessellation can typically be solved by increasing the polygon count. Large components or particularly intricate components are more likely to encounter difficulties in producing file sizes too large to process. Possible solutions to unmanageably large file sizes for large or intricate components include reducing the polygon count to the minimum acceptable threshold for geometric tolerances, reducing the polygon count below the acceptable threshold and machining to achieve the final geometric tolerance, and splitting components into multiple pieces when possible.

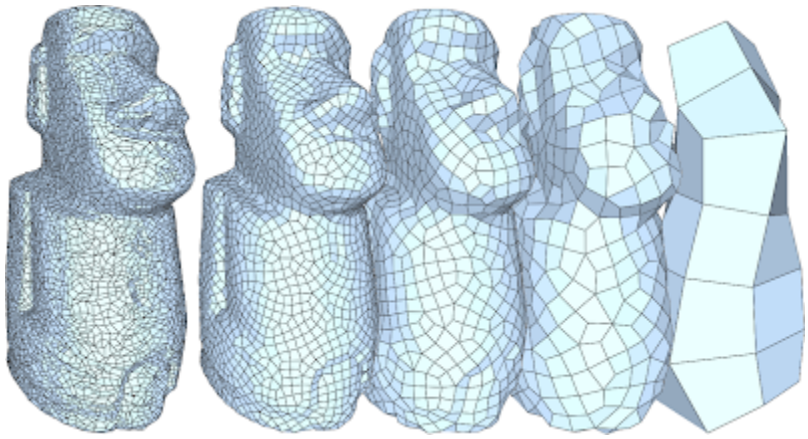

Figure 22. Example of tessellation with various polygon densities [154]**.**

Layer thickness/slicing interactions occur when the Z height of a component is not a multiple of the layer thickness (e.g., a 50.035 mm height part with layer thickness of 50 microns). Similar phenomena may occur at the interfaces of mated components if a gap/void exists at the interface; ensuring gaps between mated components are filled typically resolves the issue. The topmost layer of components affected by these interactions is typically irregular. Figure 23 illustrates layer thickness/slicing interactions at the interface of the pentagon solid model and the cylinder solid model. Layer thickness/slicing interactions

are frequently compounded by tessellation, and conversely are typically reduced in severity by increasing the polygon count. Layer thickness/slicing interactions may or may not be cause for rejection; the most likely causes for rejection are high top surface roughness and geometric tolerances. Potential solutions to layer thickness/slicing interactions are to (a) ensure that part models are a multiple of the layer thickness or (b) add supports underneath a component such that the height of the supports + the component are a multiple of the layer thickness.

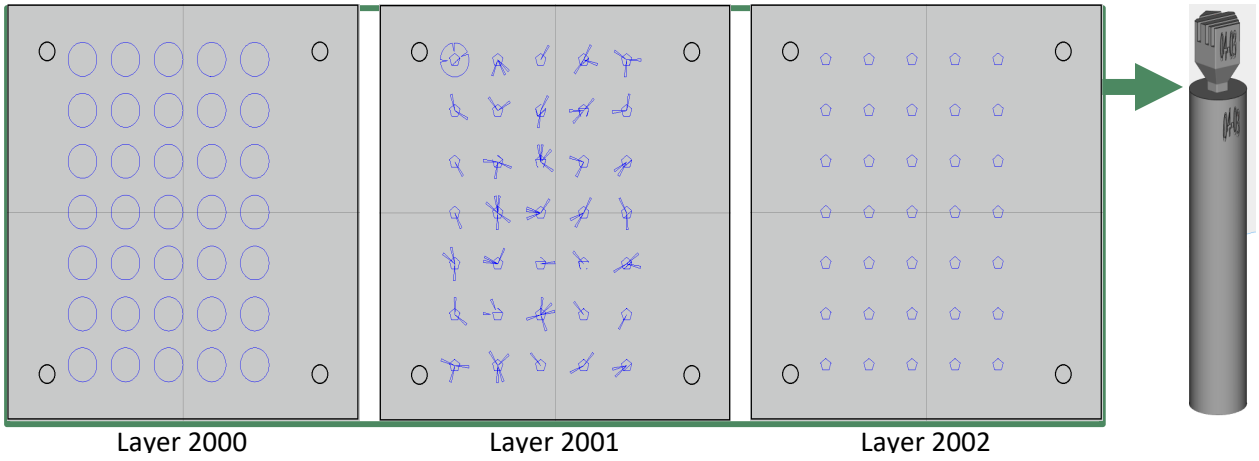

Figure 23. Example slicing layer thickness interactions at the interface between the mated pentagon and the cylinder.

Ghost parts are the result of user error; they are components that have been loaded into a slicer two or more times at the same coordinate and therefore appear to the user as one component. Slicing software treats ghost parts as separate components and assigns laser scan strategies for each part. Therefore, a ghost part will experience multiple laser scans rather than a single pass and cannot be expected to exhibit predicted microstructures or material properties.

Ghost parts can be detected by user observation of the fabrication process and by part counts in the slicing software. User observation detects ghost parts by the user looking for any remelting of scanned surfaces in the build. Unless specifically programmed, a LPBF machine should not remelt any scanned areas in a build job, and therefore, remelting is an immediate indication of ghost parts. Video capture of the fabrication process is also an effective method of verifying no ghost parts because the video can be inspected repeatedly by an unlimited number of reviewers. Part counts is a preventative method in which the slicing software user compares the count of components in the slicer software to the count of parts displayed on the screen. Figure 24 illustrates a build setup consisting of a 5 by 7 grid of tensile test specimens. The software registers 35 components, and therefore, the user can correctly deduce that no ghost parts are in the illustrated build. Counting parts is a simple and effective method but relies on users to not lose count or accidentally skip components.

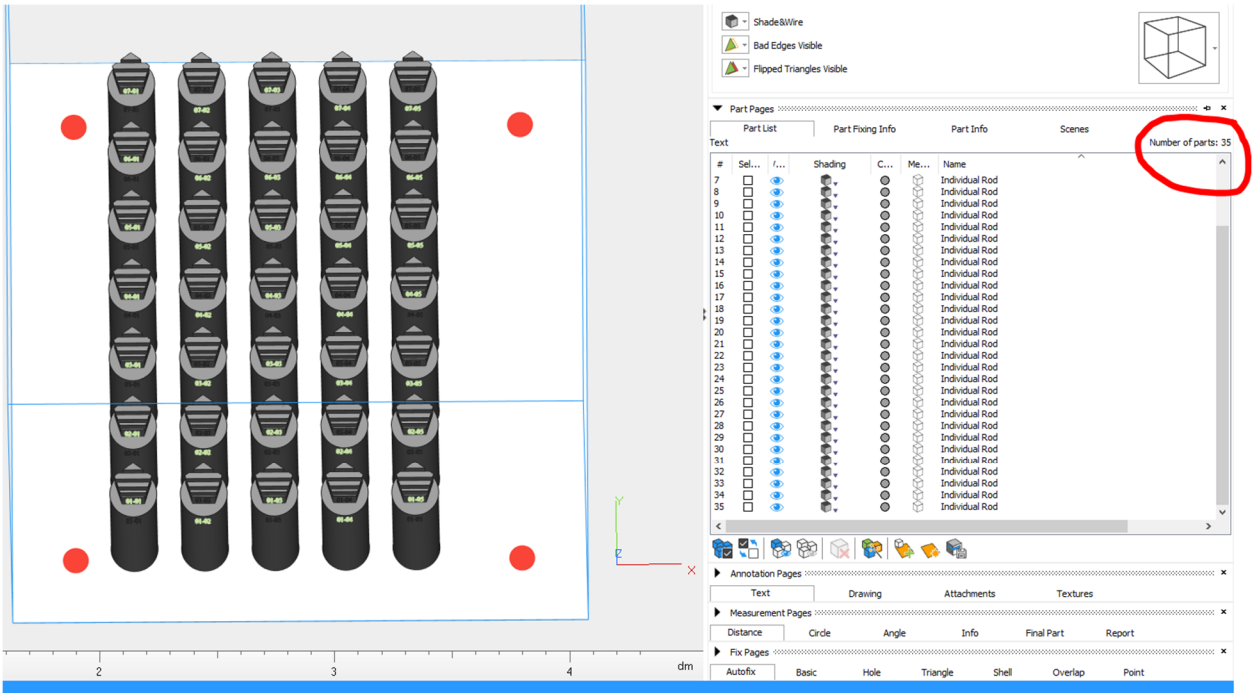

Figure 24. Example part count in slicing software.

3.1.1.2 Scan Strategy/Geometry Interactions

In conventional manufacturing, the material microstructure is homogenous and uniform throughout the initial ingot and machining does not affect material properties. This results in two important consequences that are frequently overlooked by engineers and scientists accustomed to conventional manufacturing techniques: (1) the material properties of conventionally manufactured components are homogeneous and uniform throughout the component, and (2) samples sourced from the same ingot as the component have material properties statistically indistinguishable from the manufactured component. Neither of these relationships hold for LPBF.

Instead, LPBF component geometry is a variable that affects heat transfer and the effect of the scan strategy on the local microstructure. “Scan strategy” is an encompassing term referring to both the path taken by the laser when rastering the surface of a component undergoing fabrication, as well as the laser parameters such as power, velocity, spot size, and so on. Some example commercially available LPBF scan strategy paths are illustrated in Figure 8 for reference. Scan strategies result in variable melt pool sizes, line vs. point solidification modes, and variable local part temperatures due to interactions with part geometry. Component properties such as tensile strength, fatigue strength, and ductility are not uniform throughout the component but instead are functions of geometry. To illustrate, three examples are provided in Figure 25. Example A can be expected to exhibit uniform if not homogeneous material properties once a steady-state mode of heat transfer is reached, assuming all else is equal in the build. The white bottom region of examples A and B represents the portion of the component with transient heat transfer properties. The red region of examples A, B, and C represent the steady-state heat transfer segments and can be expected to exhibit uniform material properties assuming all else is equal in the build. The green region of example B can be expected to exhibit microstructures that vary from the red region and from the top to bottom of the green region. With each additional layer in the green region, the energy applied to melt the topmost layer increases. Therefore, the heat transfer in the green region does not reach a steady-state equilibrium. The orange region in example C is similar to the green region of

example B in that a steady state of heat transfer is not reached; however, it is an example of decreasing rather than increasing energy input.

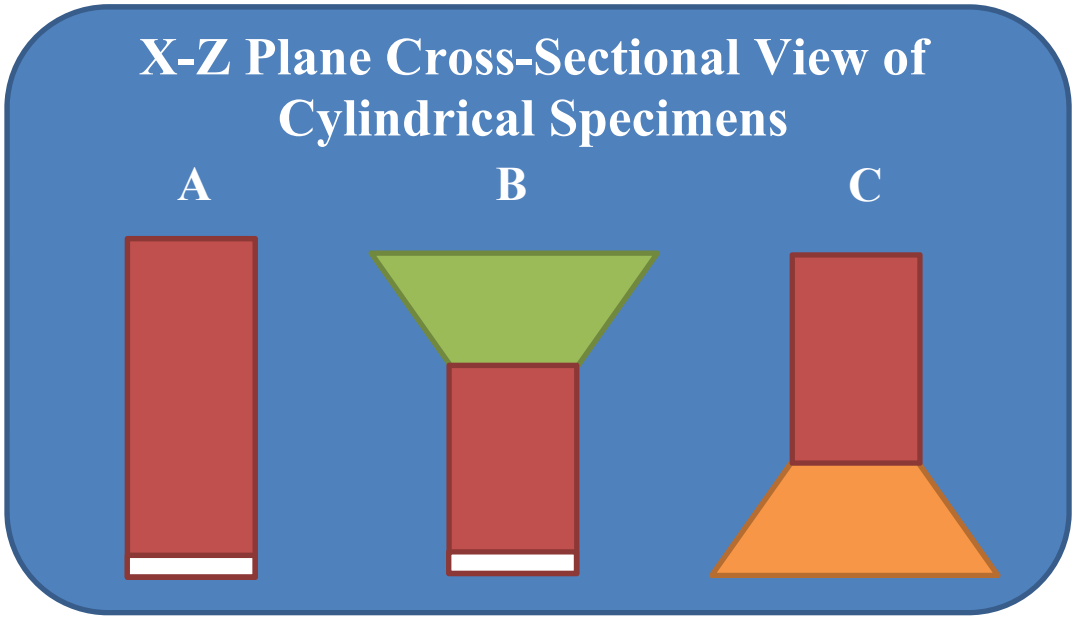

Figure 25. Illustration of the effect of changing cross-sectional area.

Scan strategy/geometry interactions may be even more pronounced in the X-Y plane. Most LPBF scan paths use a "line" solidification regime in which the melt pool solidifies perpendicularly to the overarching direction of the laser travel as shown in Figure 26 (a). This method results in rapid solidification of small melt pools, which yields fine grain size distributions and frequently prevents precipitation in many alloy systems. However, when the width of the raster stripe becomes sufficiently small as shown in Figure 26 (b), the melt pool will bridge from one raster pass to the next and result in a significantly slower solidification in the overarching direction of the laser. Raster bridging via this phenomenon almost invariably occurs in sharp corners (internal and external) and frequently occurs on the outside edge of components because of layer-wise rotation of the hatching angle. When the X-Y plane cross-sections of components are sufficiently small, raster bridging may occur across the entire surface of some layers and not at all on other layers. Therefore, obtaining uniform microstructures on components with varying thicknesses is difficult and an active area of research. The wall thickness and geometry required to observe raster bridging varies with scan strategy and the alloy used.

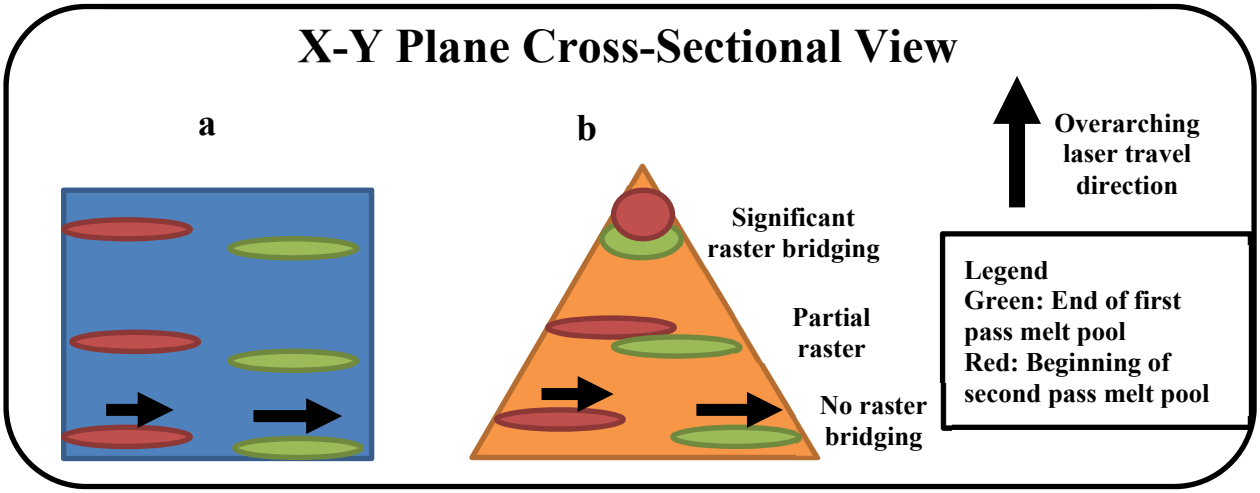

Figure 26. Illustration raster bridging (a) bulk region with no bridging and (b) corner with bridging.

3.1.1.3 Thermal History Simulations

One active area of research and process improvement is understanding, modeling, and preparing scan strategies for local thermal histories. Several factors affect performance measures such as interlayer bonding, tensile strength, porosity, and surface finish; these factors include environmental control, powder raking, power density, and control over the thermal history of a component. LPBF melts and rapidly solidifies the top layer and several underlying layers; layers immediately under the melt pool will experience multiple rapid heating and cooling cycles, which can affect grain size, phase formation, and precipitate formation depending on the ambient temperature of the build chamber, melt pool temperature, material thermal conductivity, time between passes, and component geometry. An example thermal history profile is shown in Figure 27[155]. In LPBF, the build chamber is near room temperature unless substrate heaters are deliberately added.

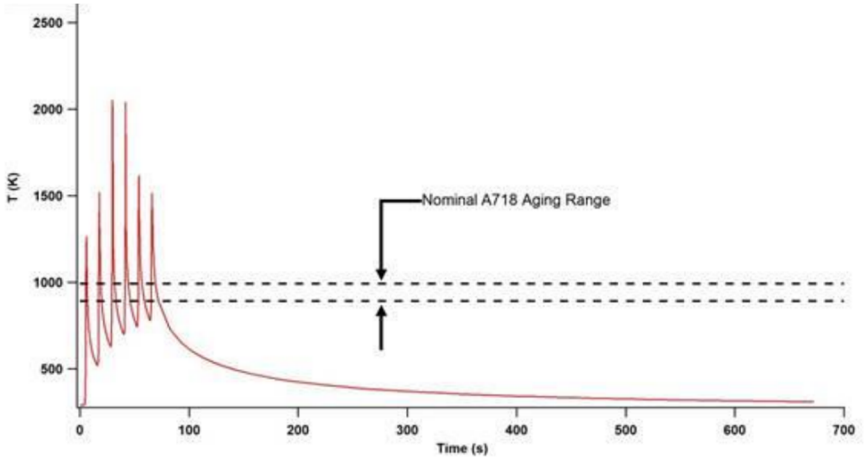

Figure 27. Example thermal cycling simulation [155]**.**

Time temperature transformations [155] and grain growth [156] are two major concerns with accurately modeling and measuring the local thermal history of a component because of the possible loss of strengthening mechanisms. One limitation of current scan strategies in preparing files is that the local temperature and thermal dissipation are not considered. For example, a pyramidal component will have

longer time intervals between layers at the bottom than at the top because of the change in cross-sectional area. For short layer times, rapid sequential deposition and insufficient time to dissipate thermal energy can produce a buildup of heat in the part, which modifies the build characteristic and acceptable process parameter window over time [157,158]. Software packages that accurately model and account for the local temperature might have delays between layers at the top of the pyramid in this example. In situ data collection is also an important aspect of the fabrication process because of the possibility of empirically correlating observational information with performance characteristics and nondestructively predicting whether a component will fail, where the failure will occur, and the mode of failure. Thermal data capture could improve thermal history simulations but would exponentially increase the quantity of data stored and processed. As discussed in Section 3.2.1, most in situ data is currently processed via artificial intelligence (AI), which introduces significant difficulties in interpretability. "Interpretability" refers to the ease with which humans can interpret the process of a predictive method. High-interpretability but low-accuracy predictive models would be linear regression, whereas low-interpretability but high-accuracy models include deep and convolutional neural networks.

3.1.2 Sieving System

Powder sieving consists of gradually feeding virgin or recycled powder into a mechanical sieve and separating sieved and "overflow" powders, which respectively do and do not pass through the sieve. Overflow consists of particles too large to pass through the sieve, spatter, and miscellaneous debris. Overflow is typically siphoned off and periodically disposed of to a metal dealer but can provide information on debris and spatter formation. A distinction exists between "single-pass" and "double-pass" sieving systems, which respectively have one and two sieves of different sizes as shown in Figure 28. Single-pass sieves only remove material larger than a certain size, whereas double pass sieves also remove material that is smaller than a certain size. Material that passes through the second sieve of a double-pass system is commonly referred to as "fines." Whether a single- or double-pass sieve is used depends on the size distribution of the unsieved powder and the objectives of the operator. Removing spatter and debris via overflow is industry standard; however, removing fines may be desirable because smaller particles have a higher probability of flammability, all else being equal. Conversely, removing fines results in additional consumables expenses and a greater proportion of reused material being diverted to the recycling waste stream. The effect of reuse and sieving on part quality is discussed in Section 2.2.1.1. Sieved powder is nominally considered good and can be either stored or transferred to a machine for use/reuse.

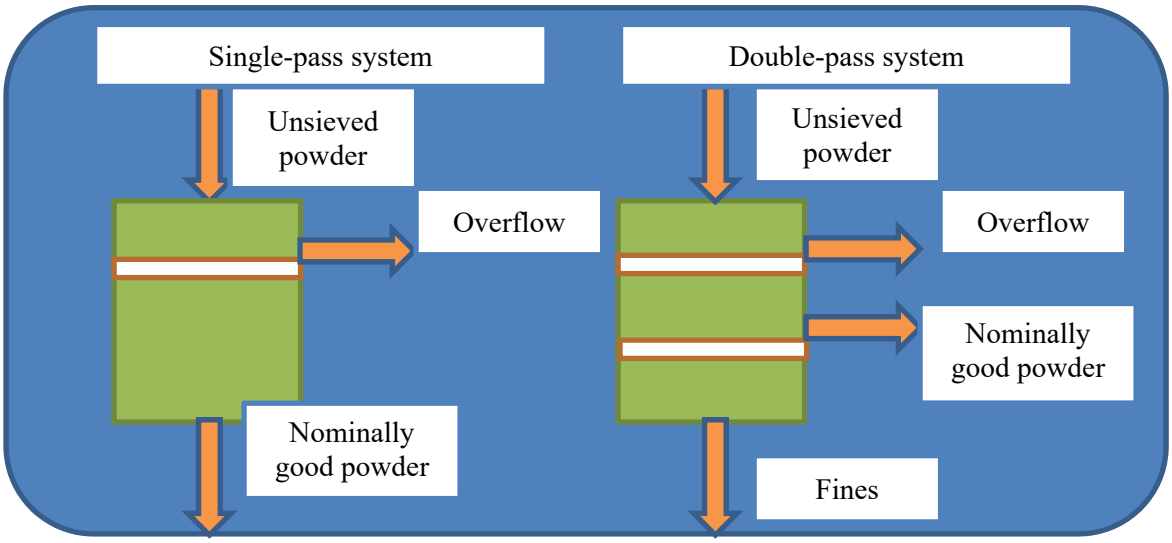

Figure 28. Single- and double-pass sieving system diagram.

Three primary QC concerns with sieving are tears and punctures in the sieve mesh, contamination, and atmospheric control. Atmospheric control is discussed in Section 3.1.3.4. Abrasion will occur and sharp debris can cut or puncture the sieve as a sieve is used, necessitating that sieve meshes be treated as consumables. The rate at which sieve meshes must be replaced depends on the frequency and quantity of powder sieved, sharpness of powder, and sieve quality and material. Sieves are typically visually inspected periodically and replaced either as needed or on a schedule. Contamination results from sieving powder of different compositions (i.e., 316L and Ti-Al6-4V) in the same sieve system or potentially different lots of the same composition and can typically be precluded by designating sieves for a specific composition. Notably, qualification of feedstock powder should occur using sieved nominally good powder and not unsieved powder—even virgin unsieved powder. Unsieved powder is not representative of the particle size distribution that will be used in the LPBF machine, and elemental composition and phases may not be uniformly distributed across the powder size range. Therefore, sieving may change the elemental composition and/or phases present in feedstock powder.

3.1.2.1 Atmosphere during Powder Recovery, Recycling, and Storage

Metal powder feedstock in LPBF has a high surface area to mass ratio and is therefore more susceptible to surface oxidation from air and humidity than an equivalent mass ingot. Additionally, surface oxidation cannot be removed from powder feedstock in the way that oxidation can be removed from ingots. Machine milling or grinding is not possible, and the high temperatures required for gaseous chemical reduction would sinter powder particles together. The rate at which metal powder oxidizes is a function of O_2 levels, humidity, feedstock composition and phases, and ambient temperature. Precise modeling of oxidation rates is beyond the scope of this document and is not included. The effects of powder oxidation on performance is discussed in Section 2.2.1.1.

Oxygen and humidity must be controlled during powder recovery, recycling, and storage to minimize the rate of oxidation. Some LPBF machines—such as the Concept Laser X Line and AddUp's FormUp series—allow for powder to be opened, transported, sieved, and stored entirely under inert gas environments. Many LPBF machines, however, expose powder to air at some point in the setup, sieving, transportation, fabrication, and cleanup processes. Air exposure most commonly occurs when loading sieved powder into LPBF machines and when removing builds from machines. Argon is the most commonly used inert gas because of its low reactivity and high molecular weight, which results in the displacement of oxygen to the top of containers. Industry-standard practice is to flood transportation/storage containers and sieving chambers with inert gas to reduce oxygen exposure; however, humidity in transportation/storage containers and sieving chambers is not routinely monitored. Whether humidity in powder correlates to detrimental qualitative properties (i.e., powder "caking" and poor flow) and/or detrimental quantitative properties (e.g., surface oxidation) is unclear. Detrimental effects due to humidity may be specific to composition and/or powder size distribution.

3.1.3 LPBF Machine

There are two fundamentally different approaches in qualifying complex machines: (1) qualifying the machine as a whole and (2) subsystem qualification. Although each method has its merits and faults, LPBF is more amenable to subsystem qualification. Subsystems in LPBF do not typically interact, and therefore, subsystem replacement or maintenance generally does not affect other subsystems. For example, adjusting laser alignment or power calibration is not expected to affect repeatability of the build stage, and replacing oxygen sensors for atmospheric control is not expected to affect the dosing repeatability of the powder bed. The following sections describes subsystems common to most LPBF machines, relevant calibration practices, and the effects of incorrectly calibrated subsystems.

3.1.3.1 Stage

The build chamber stage in conjunction with the build plate is one of the most important areas of machine hardware control. The build stage is raised and lowered specified amounts during a build to allow for additional powder to be spread across the top surface of a component. Lowering the stage by an insufficient amount can result in abrasion of the recoater wiper blade, which results in nonuniform powder spreading or in extreme cases of abrasion short feeding. Lowering the stage too much results in thicker than specified layers, which can cause delamination, unmelted powder, and porosity. Nonzero mean variation from specified values may result in incorrect Z axis dimensions.

Build plates must be level and sufficiently flat. Non-level build plates will result in incorrect part geometries as depicted in Figure 29. Build plate flatness does not affect part quality or geometry after the first few layers and does not affect geometry at all if the component is designed to be "floating" on supports as illustrated in Figure 30. However, flatness does affect the uniformity of powder spreading in the first few layers, which affects bonding of the fabricated component to the build plate. One additional concern with build plates is sufficient stiffness to resist residual stress deformation. Fabrication of LPBF components results in tensile stresses in the top surface of the build plate, which can cause build plate warping. Warping significantly affects the geometric tolerance of fabricated components as illustrated in Figure 31. Build plate warping is discussed further in 3.2.2.

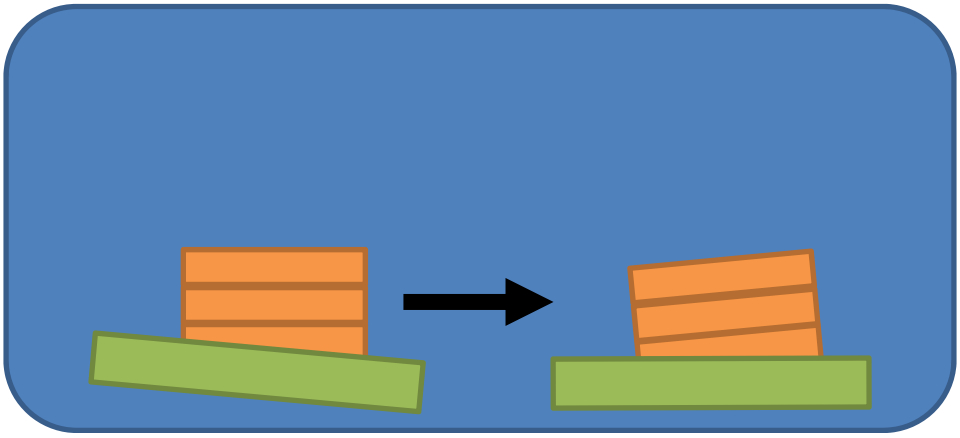

Figure 29. Illustration of effect of non-level build plates on part geometry.

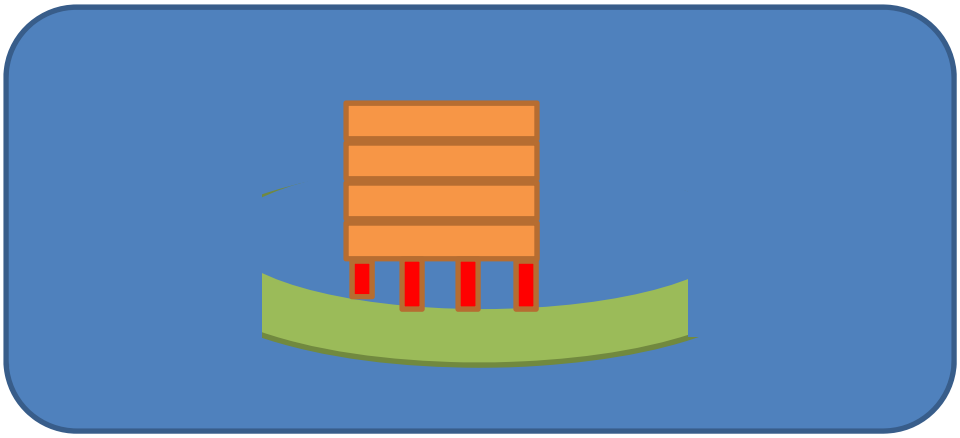

Figure 30. Illustration of mitigating non-flat plates via supports.

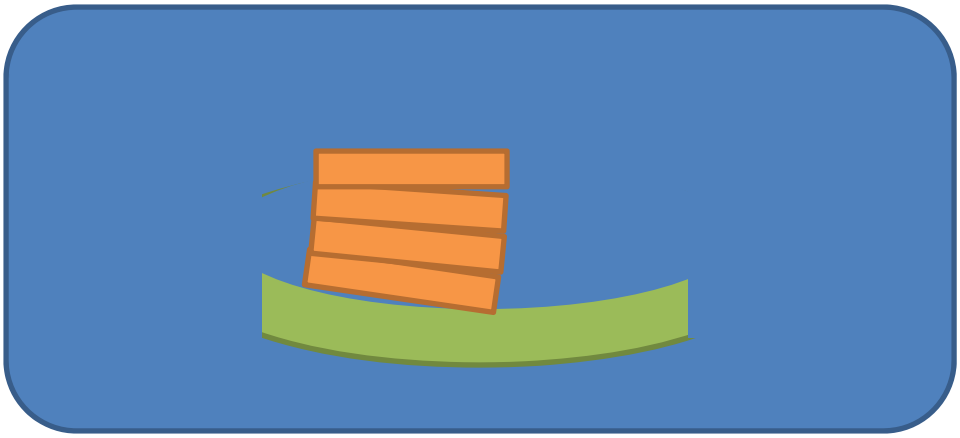

Figure 31. Illustration of warping effects on part geometry.

Possible sources of contamination in the build chamber stage and build plate are dust and debris on the consumable build plates and worn seals in the build chamber stage. Build plate contamination may be reduced or eliminated by cleaning and wiping down build plates immediately before placement in the LPBF machine, and stage seal contamination may be mitigated by routine inspection and replacement of seals.

3.1.3.2 Powder Hopper

QC of the powder hopper consists of vertical position control and preventing or minimizing contamination. After sieving, powder is either stored or immediately transferred to the LPBF machine. Transfer may occur by manual transference with a scoop, gravity feed from the bottom of a transfer container, or vacuum. Under no circumstances should unsieved powder be transferred to the powder hopper of the LPBF machine. All methods of transfer can result in contamination if general cleanliness is not observed. For example, contamination in manual transference can be prevented or minimized by wiping down scoops to remove any residue, dust, or metal powder (and preferably designating scoops for specific compositions), wearing clean disposable gloves, wiping down machine surfaces and windows prior to transference, working in undisturbed air, and mopping floors. Seals in the LPBF machine should also be periodically inspected and replaced to prevent contamination.

The only function of the powder hopper is to dose a specified amount of powder to the recoater by vertically raising the powder hopper as depicted in Figure 32. Typical dosing rates are 150 to 200% (i.e., 1.5 to 2 times the amount of powder needed to coat a layer) to ensure that sufficient powder is delivered to the recoater. Variation in the powder hopper position movement and thus dosing rate can be a concern if the hopper position variation is significant. “Overdosing” or delivering more powder than specified is only a concern if it interferes with the recoater or results in the powder hopper emptying before build completion. Detecting insufficient powder to complete a build is straightforward because the LPBF machine will halt the build and/or the top layers of the component will not be fabricated. Detecting short feeding, also known as incomplete spreading, can be significantly more challenging. An example of short feeding is depicted in Figure 32. Systematic short feeding can be detected by part delamination and severely incorrect part geometries. However, intermittent short feeding may or may not result in delamination; components may be successfully fabricated with intermittent short feeding with no visually observable defects. Manual operator observation can detect intermittent short feeding but is not a practical solution. One effective method to detect systematic and intermittent short feeding is placing a camera in the top of the build chamber or adjacent to the laser optics train as shown in Figure 32 (a); an image is captured after every layer of powder is spread which can be reviewed by humans or AI networks for short

feeding. An example neural network classification of anomalies is shown in Figure 32 (b) for reference. [159].

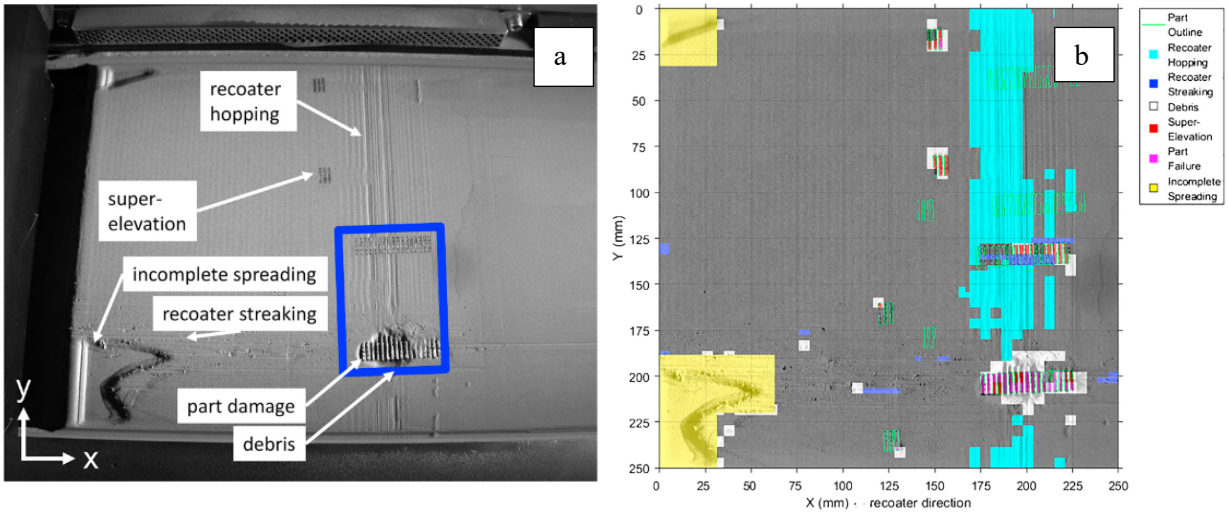

Figure 32. Embedded camera (a) raw image and (b) convolutional neural network classification of anomalies [159]**.**

3.1.3.3 Laser Optics

Three primary aspects of the laser optics system require calibration and certification: laser power, laser beam spot size, and mirror control. Laser power and spot size affect melt pool geometry and fabrication issues such as delamination as covered in Section 2.3.1. Mirror control affects the acceleration at the beginning and end of melt lines, the velocity of the laser under steady-state travel, and the geometric precision of the fabricated part.

LPBF laser power can be measured by two methods: calorimetric techniques and radiation pressure. Calorimetric techniques can measure laser power up to 100 kW [160,161] (which encompasses all commercial LPBF at the time of this publication), are accurate to ±3% [160,161], and are a method by which the same sensor can calibrate multiple LPBF systems. Two disadvantages of calorimetric techniques are that the sensors (1) have a maximum permissible power density in watts per square millimeter, which typically necessitates defocusing the laser beam at high (>300 W) wattages, and (2) can take discrete measurements only before and after fabricating a part. Reviews of calorimetric methods can be found from refs. [162,163]. Radiation pressure is a measurement technique in which the photon mass of light striking a surface is measured. NIST manufactures a standard-traceable radiation-pressure device that can measure laser power up to 100 kW [164] and, unlike calorimetric methods, does not have a power density restriction. Radiation-pressure techniques are accurate in the range of ±1.3 to 4.5% with accuracy improving with increasing power [164] and can take measurements anytime the laser is operational, including during a build. However, radiation-pressure sensors must directly integrate into the laser optics system; to the authors' knowledge, no commercial LPBF machines with integrated radiation-pressure sensors exist at the time of this publication. Reviews of radiation-pressure measurement theory can be found from refs. [165–167].

Three accurate methods to measure laser spot size have been developed: charged coupled devices (CCDs), apertures, and the knife-edge method. CCD measurements are obtained by diffracting the laser through a beam splitter; the majority of the beam is directed to a heat sink and a small fraction of the laser beam is directed to a CCD/camera where the diameter and power distribution of the laser are measured.

The reduction in laser power via the beam splitter ensures that the camera will not be destroyed or saturate the camera. In theory, CCD can also be used to calculate the laser power but requires precise calibration values to do so. Apertures determine laser spot size by firing the laser perpendicularly through either a series of circular apertures with varying diameters or a single aperture with a variable aperture onto a power measurement device. The portion of the laser beam greater than the diameter of the aperture is blocked, resulting in power measurements as a function of diameter. The laser beam's power is either assumed to follow a circular Gaussian distribution or an appropriate distribution based on empirical measurements, and the laser beam diameter is calculated as a best fit given the series of power-aperture diameter measurements. The knife-edge method is fundamentally similar to the aperture method, but rather than a series of apertures, a single flat edge is moved across the laser beam's path, and the measured power related to the knife-edge location. An illustration of the aperture and knife-edge methods is provided in Figure 33. Notably, the aperture and knife-edge methods provide information only on the mean laser beam diameter and do not describe variation in circularity or the power distribution. CCD methods can be used to determine the mean laser beam diameter as well as circularity and the power distribution. Accurate absolute power distribution values can be difficult to obtain from CCDs because of calibration precision requirements; however, qualitative measurements of the power distribution can be coupled with separate power measurements to determine precise absolute-value laser power distributions. All laser beam spot size measurement techniques (CCD, aperture, and knife-edge) are discrete measurements, can only be obtained prior to and after a build, and can only be measured perpendicular to the laser beam (i.e., in one location on the build plate directly below the laser).

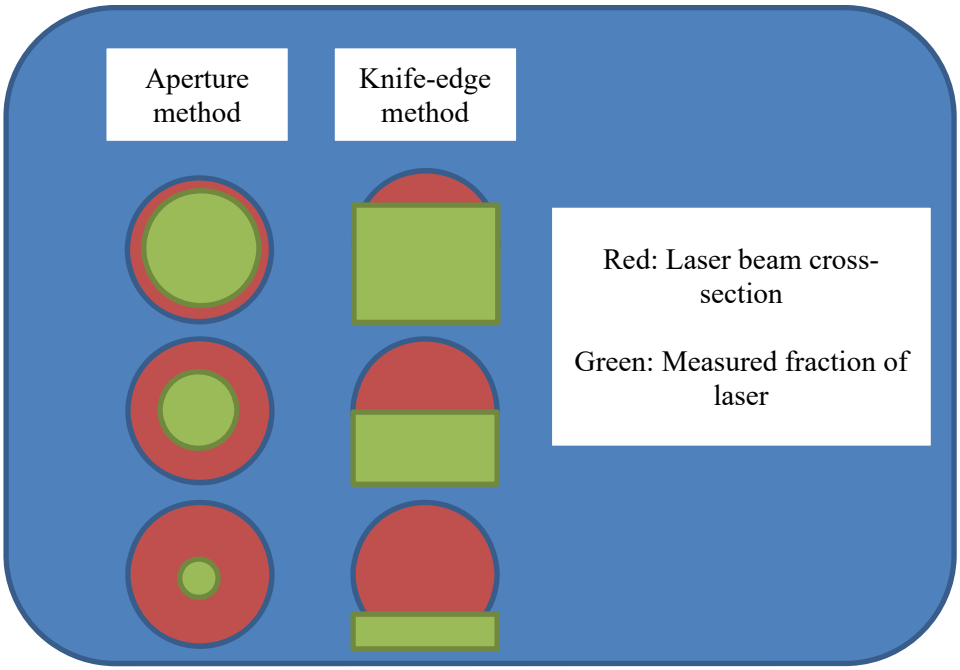

Figure 33. Illustration of aperture and knife-edge laser beam measurement methods.

LPBF uses a series of mirror galvanometers or "galvos" to direct the laser beam to the appropriate location on the build plate and an F-Theta lens to focus the beam to the specified spot size on the build plate; a representative diagram of a mirror control system is provided in Figure 34 [168]. Because the mirrors have mass and inertia, instantaneously changing laser beam travel direction, acceleration, or location is not possible. When discussing mirror control, the distinction between dimensional control and location control is important to note. "Dimensional control" refers to fabricating a component that is geometrically correct but not necessarily located at the specified X-Y coordinate on the build plate or with the correct rotation on the build plate. "Location control" refers to accurate placement of the laser beam

on the build plate. An example diagram showing location vs. dimensional control is provided in Figure 35. LPBF machines that use a single laser require accurate dimensional control but not accurate location control if the fabricated component is removed from the build plate. For example, if a 1 cm cube is fabricated with a single laser and is removed from the build plate, whether the cube is slightly translated in the X-Y plane or rotated on the build plate is not important; rather, the cube must be dimensionally accurate. Conversely, if a fabricated component is left on a build plate during service, accurate location control is important to achieve specified dimensional requirements. Accurate location calibration and control is also critical when multiple lasers are used to fabricate a single component; misalignment between lasers can result in interlayer shifts or intra-layer high-porosity "stitching" regions in parts where the lasers interface depending on the scan strategy used. Each laser melts a discrete area of a layer, and the interface between said areas is referred to as "stitching." If parameters and/or laser positional control are not carefully adjusted, the melt pool overlap between each laser's area will be insufficient and result in high porosity. Inter and intra-layer multi-laser misalignment is illustrated in Figure 36.

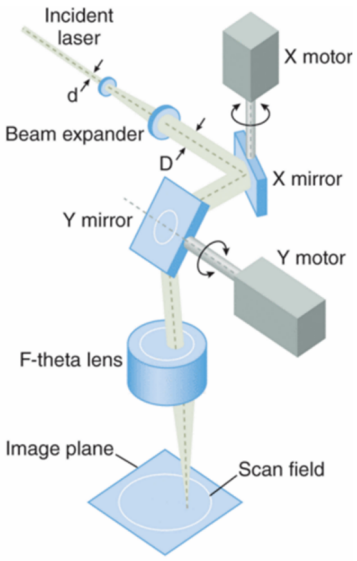

Figure 34. Illustration of LPBF mirror system [168]**.**

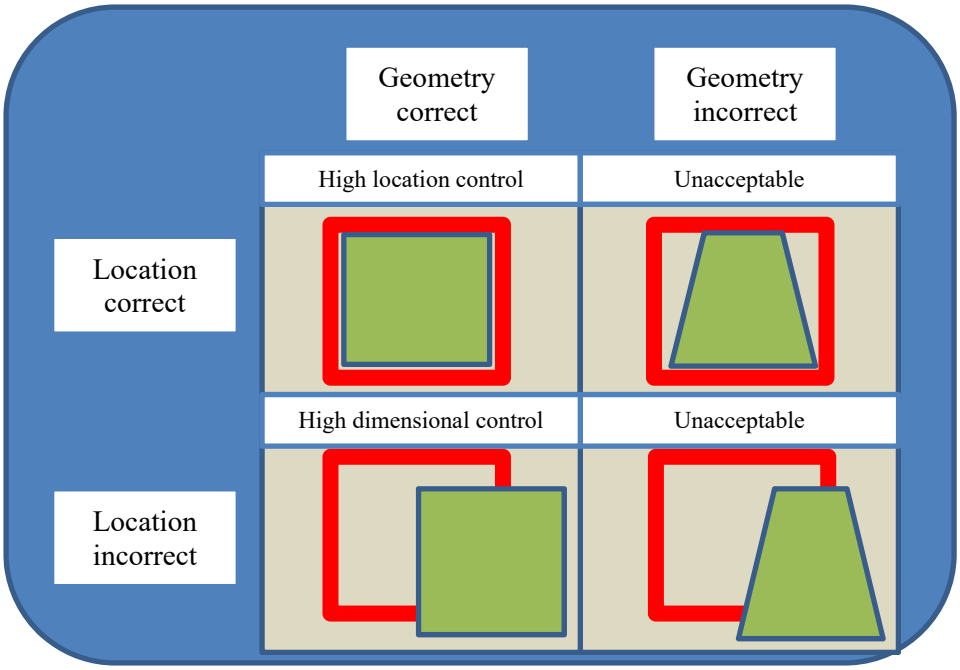

Figure 35. Illustration of dimensional vs. location control.

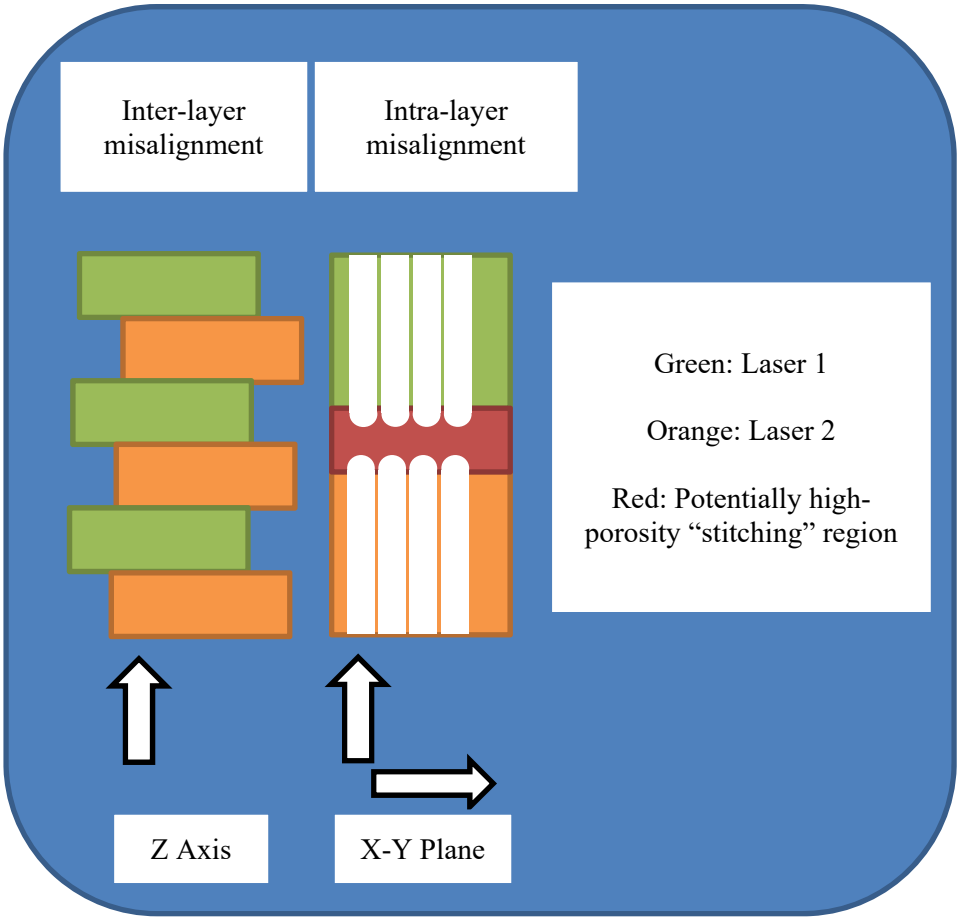

Figure 36. Illustration of multi-laser inter- and intra-layer misalignment.

Measurement of laser position control is an ongoing area of academic and commercial standardization and, to the authors' knowledge, no method that directly measures laser position exists at the time of this publication. Rather, laser alignment is indirectly determined by burning patterns into laser paper or a bare build plate and measuring the etched and burned patterns. The difficulty with this method is that highly accurate measurements are being attempted over comparatively large distances. Specialized optical systems are required to accurately measure parallel or perpendicular lines at the scales (>200 mm) required for LPBF, and the inherent stochastic variation in burn/etch lines adds to the measurement devices' uncertainty. A simpler and more direct method is to fabricate either the components to be used or standardized artifacts [169] and take measurements via traditional and established methods such as calipers, micrometers, shadowgraphs, coordinate measuring machines, and so on. One potential difficulty with direct measurement accuracy is component distortion due to residual stresses; conversely, direct component measurement may be desirable because deviation from specification can be detected before or after heat treatment and/or before or after removal from the build plate. A second and more serious difficulty with direct component measurement is that minor misalignments in multi-laser systems may only be detected as increased surface roughness (see Figure 36) and an internal high-porosity stitching region may be undetected. Depending on the degree of misalignment, the stitching region and pore size distribution may not be detectable in a computed tomography (CT) scan and instead require destructive microscopy methods to observe. Because of the complications discussed, using multiple lasers to fabricate a component will necessitate extensive demonstration of accurate laser alignment to ensure that a high-porosity stitching region does not exist within a component. Using multiple lasers where each laser fabricates a separate component on the build plate does not suffer from the same alignment complications.

Neither direct measurement of fabricated components nor indirect measurement of laser alignment via burn or etch patterns supply information on mirror acceleration or steady-state travel velocity. To the authors' knowledge, the only technique for determining mirror acceleration and travel velocity is ammeter measurement of the mirror motors. After a voltage is applied to the motor to move the mirror, an increase in amperage occurs until the mirror has moved to the correct location. The time difference between when the voltage is applied and the amperage decays to a specified threshold can be quantitatively coupled to mirror acceleration and velocity.

3.1.3.4 Atmosphere During the Build Process

Atmospheric control during the build process is significantly more critical than control during sieving and storage because of the rapid oxidation many metals exhibit when molten material is exposed to air. Monitoring and closed-loop control of oxygen levels during fabrication is industry-standard practice in LPBF; however, as with sieving and powder storage humidity, monitoring and control are not routinely performed. The inert gas environment in LPBF is used not only to minimize melt pool oxidation but also to remove fine "soot" particulate and prevent attenuation of the laser. Attenuation occurs when soot, smoke, or other particulates intersect the laser and cause loss of delivered power, spot size change, or power distribution change. During the fabrication process, inert gas is blown across the build chamber and removes soot particulate as illustrated in Figure 37. Determining the appropriate inert gas velocity is empirically determined by observation; velocities too low result in attenuation of the laser as soot is not removed, whereas velocities too high result in powder particles being lofted and attenuating the laser as well as result in nonuniform powder beds.

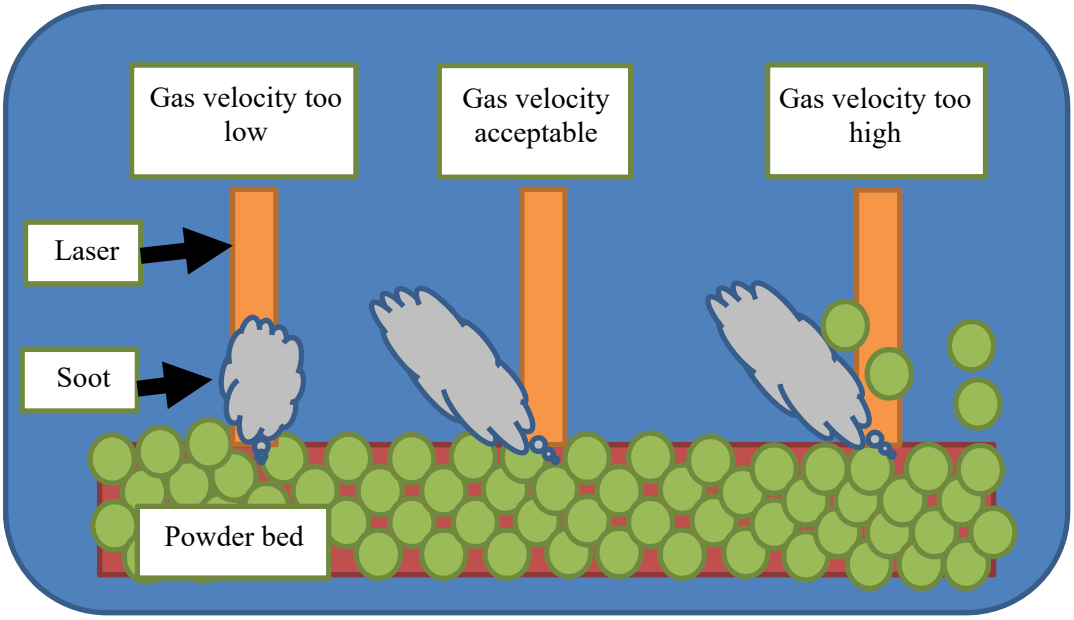

Figure 37. Illustration of effects of inert gas velocities in LPBF.

Variation of the gas velocity occurs in both the X-Z and X-Y planes; variation in the X-Z plane may occur because of manufacturer design and is illustrated in Figure 38. Manufacturers frequently use two laminar flow regions in the build chamber; the lower-flow upper region exists to reduce manufacturing costs as well as to minimally interfere with the higher-velocity lower region. X-Z plane gas velocity variation is not considered problematic provided that soot is effectively removed and powder is not lofted.

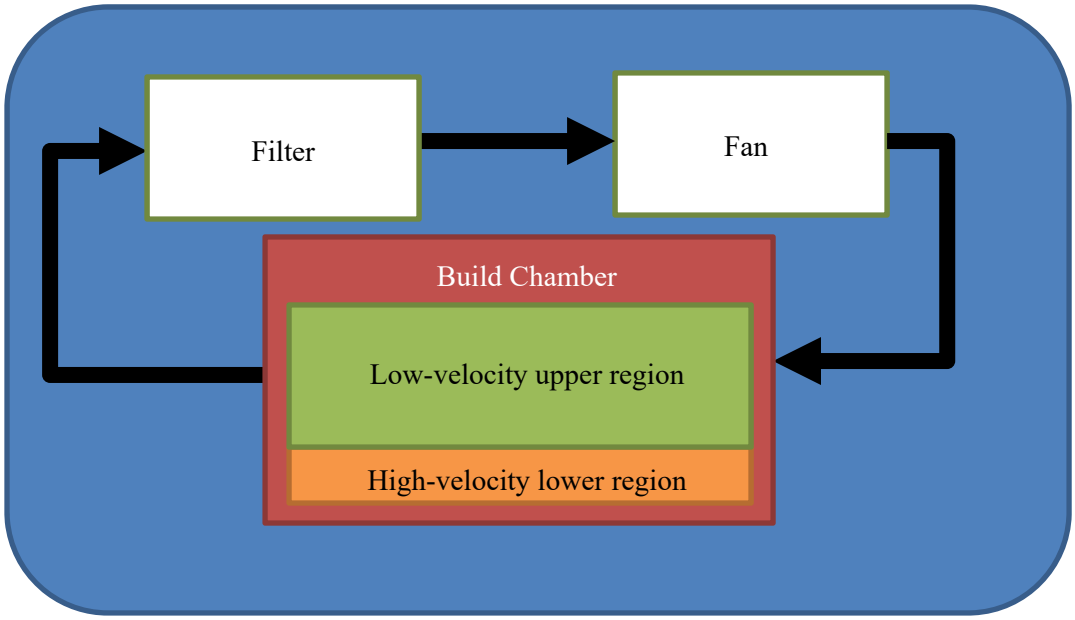

Figure 38. Illustration of LPBF ventilation system in the X-Z plane.

Whether gas flow variation in the X-Y plane is problematic is unknown. The build chambers of most LPBF machines place the chamber walls close to the powder bed to reduce manufacturing costs and

machine footprints. However, this arrangement results in significant gas velocity losses near the edge of the powder bed due to friction with the chamber walls as illustrated in Figure 39.

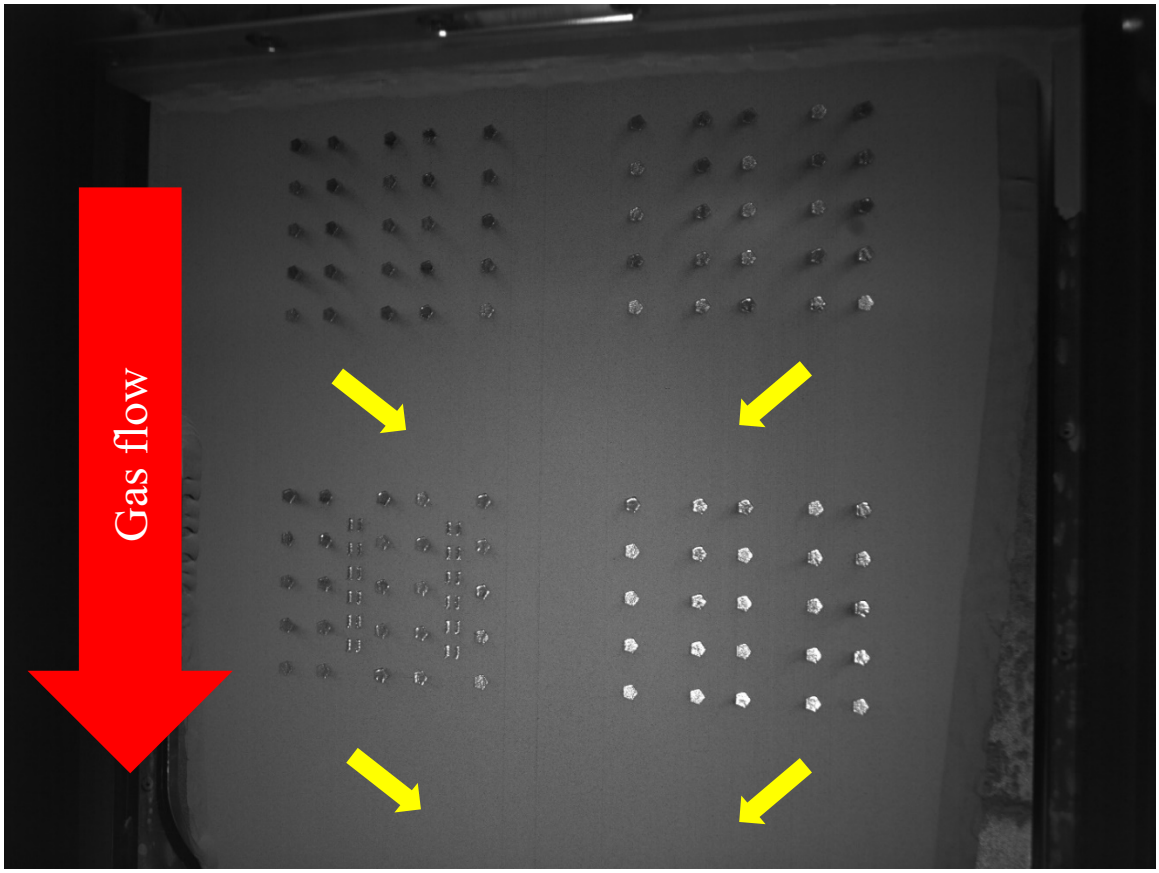

Figure 39. Directional soot deposition due to gas flow variation on a Concept Laser X Line 2000R. Yellow arrows indicate the direction of soot deposition from the fabrication process.

3.2 DURING FABRICATION

Several technical challenges remain in fabricating defect-free LPBF components and detecting discontinuities above an acceptable threshold. Component residual stress is an inevitable side effect of the fabrication process and may result in rejection due to warping outside of specified tolerances. If residual stress is sufficiently high, cracking and delamination may occur, which will automatically result in component rejection. At the time of this document's publication, scan strategies are typically calculated and set prior to fabrication rather than using feedback systems to adjust the process. An active area of research is in situ feedback loops to detect and correct process discontinuities such as recoater short feeding.

3.2.1 In Situ Feedback and Monitoring

One active area of research for AM QC is in situ process monitoring and closed-loop feedback systems. In situ monitoring captures information related to process quality (e.g., melt pool shape and size) as well as machine processing discontinuities (e.g., short feeding, streaking, and recoater chatter). In situ process monitoring has been identified as a critical obstacle to robust AM systems [170,171] because of the high number of process parameters and layer-wise nature of LPBF. One study identified more than 50 distinct process parameters for LPBF [172], and melt pool velocity, power density, and thermal energy dissipation

are well known to affect material properties and successful fabrication completion. A distinction exists between open-loop and closed-loop monitoring. Open-loop monitoring only collects data for post-fabrication review, whereas closed-loop monitoring sends commands to the LPBF machine (e.g., to reapply a powder layer or remelt a layer). Early drafts of ASME pressure vessel codes for AM components at the time of this publication suggest that closed-loop monitoring will not be accepted. Nevertheless, a review of closed-loop monitoring is included for completeness. In situ monitoring has previously been reviewed [173,174] and can be compared in many ways to the process monitoring in modern machining systems. As monitoring sensors collect data, the data can be input to a control algorithm that modifies key parameters to maintain desirable processing conditions.

Temperature and visual imaging are the two most common in situ methods; common monitoring devices are cameras operating in the visual, near-visual, or infrared wavelengths and pyrometers. Noncontact methods are preferred to minimize fabrication downtime in addition to the difficulties of using contact measurement methods. In-line cameras have been used to observe melt pool electromagnetic radiation and calculate the temperature and dimensions of the melt pool [175]. This method is patented by Concept Laser [176] and implemented in a closed loop to stabilize and control the melt pool. One acute difficulty of camera control of melt pools is the significant data accumulation due to high resolutions. Data must be collected and processed and commands returned in real time to be of value. Further compounding the difficulty is the need to incorporate macro thermal data of the entire powder bed environment with local melt pool information (i.e., multi-scale computing).

Pyrometers are frequently used for in situ temperature measurement [174,177–184] because they allow for in situ data collection with no adverse effects on the fabrication process. However, pyrometers and cameras are limited to measuring the powder bed surface, and accurate absolute measurements depend on accurate emissivity values for a given alloy at a given temperature. Cameras have also been used to detect defects such as porosity, cracks, and incomplete powder raking [185]. Laser displacement sensors are less commonly used for process monitoring but have measured in situ distortion [186] and layer height [187–189]. The only commonly used contact measurement device are thermocouples [186,190–192]. Thermocouples are inexpensive compared with pyrometers, high-speed cameras, and infrared cameras; however, they are limited to substrate measurement because of the nature of LPBF.

In situ data capture is primarily along the top surface of the build chamber and environmental sensors built into the LPBF machine. Environmental sensors may include inert gas flow rate [193,194], oxygen content [193,194], inert gas temperature [193], build chamber temperature [194], build chamber positive pressure [194], and build chamber preheating temperature [194] depending on manufacturer and machine options. Spikes in environmental data, such as oxygen, can inform investigation at specific layers for defects. In situ data of the top surface of the build chamber may consist of observing the melt pool size and morphology [195] and optical images of the build chamber [159,196–200]. Images of the build chamber may be after powder spreading and/or after fusion for a given layer, and each image type provides different information. Post-powder-spreading images inform the uniformity and quality of the powder layer and may reveal complications such as component swelling, short feeding, and worn recoater blade grooves. Post-fusion images may detect processing issues such as delaminated layers (commonly referred to as “shrapnel” or “debris” because of appearance), unmelted regions due to software errors, and soot patterns. Soot patterns in the unmelted powder of the build chamber provide qualitative information on the directional vectors and magnitude of the inert process gas flow. An example of a post-powder-spreading image with short feeding is provided in Figure 40; the short-feeding area extends from the center of the image to the left edge in a wedge shape. Figure 40 (a) is the original build chamber image, Figure 40 (b) is a thresholded version to highlight the short feeding to the human eye, and Figure 40 (c) is an example of AI detection and classification of defects. The vertical stripe in Figure 40 (b) is an artifact of thresholding and should be ignored.

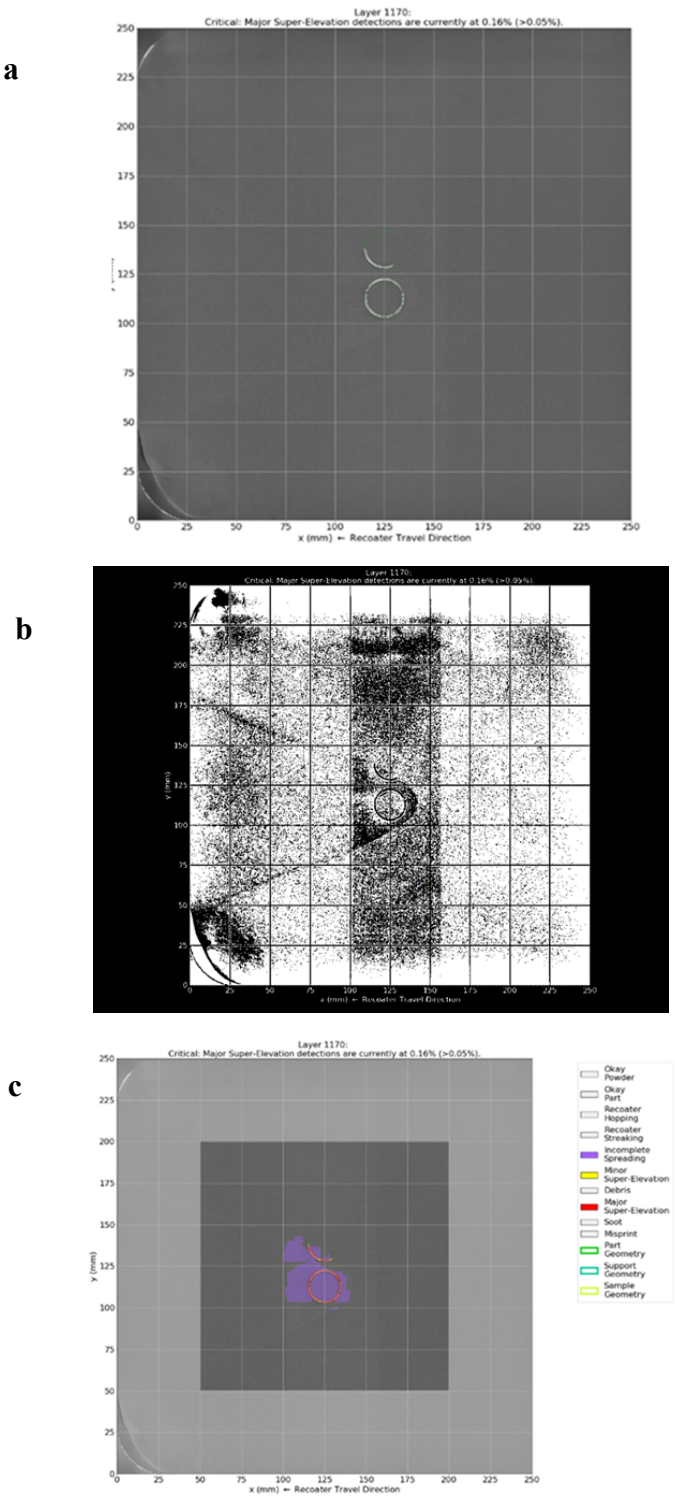

Figure 40. Powder short-feeding example of an (a) original image, (b) thresholded image, and (c) AI defect classification.

Because of the large (hundreds to thousands) number of images and granularity required to detect defects, AI has emerged as a prominent method of analyzing in situ images. The objective of AI analysis is not to recommend that a component is nominally good but rather to flag possible defects for human review. In

that regard, a lack of AI-flagged defects should not be interpreted as a recommendation that a component meets quality specifications but rather that possible defects were not detected. Build chamber images with AI analysis offer the possibility of intra-component defect detection and precise location in 3D space for multiple defect types. However, some AI network types are not agnostic to their training data. For example, if an AI is trained on a data set where nominally "defect-free" components are fabricated in the top left quadrant of the build chamber and "defect-intensive" components are fabricated in the bottom right corner, that AI may maintain a permanent bias to flag more defects in the bottom right corner. The only way to avoid such bias is to train an AI exclusively on the identical component, machine, build plate coordinates, and processing parameters that will be used for the final inspected component. In a production setting, this limitation may not be an issue because of the need to fabricate a series of proofing builds for destructive analysis; the AI may be trained on in situ data from the sacrificial startup builds. One significant drawback to AI is the difficulty of interpretability; AI and machine vision have demonstrated an impressive capability to accurately interpret vast quantities of data, but determining how and why outputs were calculated can be difficult.

Closed-loop monitoring has been explored by some commercial LPBF manufacturers such as Concept Laser. Concept Laser's QM (Quality Management) series is largely open-loop; however, the QM Coating software module uses optical images of the powder bed to detect short feeding and reapply a powder layer if necessary [201]. As reported in ref [202], Politecnico di Milano recently patented a hybrid method of defect detection and QC; if defects are detected via optical or infrared images, the entire layer is ground off and rebuilt. To date, in situ process monitoring has largely focused on categorical discontinuities due to the nature of AI, and is therefore better positioned to detect "black swan" events rather than estimating continuous outcomes such as tensile strength. "Black swan" events are defined as low-probability but high-impact occurrences; in the context of LPBF, incomplete spreading or delamination are prime examples. Development of closed-loop systems is ongoing; it is unclear at this time what types of closed-loop monitoring will prove effective, what role AI will play in closed-loop monitoring, and how closed-loop corrective actions will be documented and approved in a QC program.

One limitation of all build chamber surface monitoring methods is that only the top surface is observed. Defects below the surface of a layer (e.g., keyholing porosity) cannot be detected by line of sight methods. Theoretically, ultrasonic methods could produce a 3D reconstruction in semi-real time of a component undergoing fabrication, including defects such as porosity and cracks. However, in situ real-time ultrasonic monitoring has not proven successful as of the time of this document's publication [203,204].

3.2.2 Residual Stresses and Substrate Warping

Build plates are used in LPBF systems to adhere the first layers of a component [25] and to provide a planar starting surface. Substrates may be unheated or heated via internal heaters. Reasons for substrate heating include in situ stress relief, decreasing thermal gradients between the melt pool and previously deposited layers, or forming phases or microstructures that require specific thermal conditions [205]. Substrates may be composed of the same material as the component to minimize differences in coefficients of thermal expansion, cost-effective materials, or alloys that form brittle interfaces with deposited materials for easy removal (e.g., Ti-6Al-4V deposited on stainless steel 304). However, substrate warping may occur [206] if the thermally induced residual stresses exceed the YS of the substrate, thereby causing plastic deformation.

Thermally induced strains and residual stresses are an inherent aspect of LPBF because liquid metal is solidified on a comparatively cooler underlying material [205]. Residual stresses can cause delamination, cracking, and warping, all of which will result in failed fabrication. Accurately understanding and modeling thermal stresses and in situ heat transfer can facilitate optimal processing parameters and

placement of sacrificial heat dissipation supports attached to a component. Residual stresses in LPBF components tend to be concentrated near the substrate interface, tensile stresses near edges, and compressive stresses in the interior [99,207–209]. Mechanical support structures may be used to lift the component off the build plate and slightly reduce residual stresses due to the supports having reduced cross-sections that limit energy transfer to the build plate and result in higher mean component temperatures [205]. Residual stress may be relieved when a component is removed from the build plate via deformation [207], which would typically be undesirable. Therefore, stress-relieving heat treatments with the build plate attached are common in LPBF. Scanning strategy affects residual stress in LPBF, and the effect of island scanning on residual stress has been reported [206,210]. Directly comparing the effect of scan strategies is difficult because of incomplete fabrication parameter reporting in literature. As a reference point, residual stress in LPBF pure iron has been reported at 60 to 80% of the YS [41].

Characterization of residual stress may be achieved by several methods, including neutron diffraction [211,212], x-ray diffraction [205,213], contour [212,214], microhardness [215], and hole drilling [216]. Microhardness may be used for single phase alloys but only provides information about residual stress at the surface. The contour method uses deformation measurement after cutting a sample (i.e., EDM), which provides comparable data to neutron diffraction [217] with less influence from elemental composition but is a destructive measurement method. X-ray diffraction and neutron diffraction can both measure residual stress but require expensive specialized equipment. Finite element analysis modeling has been used to predict residual stresses in LPBF [218], and simplified thermal cycle modeling has been reported to qualitatively correlate with experimental substrate warping [219]. A thorough review of AM residual stress origins, modeling, and remediation has been published [115].

3.2.3 Cracking and Delamination

Two types of cracking have been observed in AM components [220] in addition to interlayer delamination. Solidification cracking occurs when the tensile stress in the solidified regions of the melt pool exceeds the material's YS, which is also observed in welding [31]. Solidification as well as thermally induced contraction in the solid-state results in local tensile stress, but displacement is inhibited by bonding with substrate layers. The second type of cracking is known as "liquation cracking or grain boundary cracking and is observed at grain boundaries in partially solidified regions of the melt pool. Upon solidification, some phases nucleate first and begin contracting before the remaining material has solidified, and the liquid inter-grain region can act as a crack nucleation site. Several material characteristics have been related to liquation cracking and include large differences between the solidus and liquidus temperatures (as with Ni superalloys [31]), large melt pools due to low thermal conductivity (as with Ti-6Al-4V), and large coefficients of thermal expansion (as with aluminum alloys) [221]. Literature has been published on the causes and mitigation of cracking in Ni superalloys [31].

Delamination occurs because of residual tensile stresses in the solidified region exceeding the layer interface YS [222] and is illustrated in Figure 12. Delamination can be caused by either incomplete melting of powder feedstock or insufficient remelting of underlying layers to achieve high interlayer strength. Incomplete melting of feedstock and the resulting internal porosity may be largely remediated by HIPing if pores are closed, but cracking and delamination cannot be remedied by post-processing. If porosity is sufficiently high, macroscopic cracking can occur because of stress concentrations, thereby causing the residual stress to exceed the strength of the material. Substrate heating has been demonstrated to reduce macroscopic cracking in LPBF [220].

3.3 POST-FABRICATION

Post-fabrication requirements and processes for LPBF components are more nuanced than for equivalent conventional components because LPBF material properties are affected by spatial orientation and

interactions between the scan strategy and component geometry. Therefore, samples for testing properties must be sourced from the final geometry and scan strategy used in production. LPBF components also typically contain internal porosity, which may need to be quantified via CT scans depending on component application.

3.3.1 Post-Process NDE Methods

Nondestructive post-process testing of LPBF components is a critical aspect of certification for NPP applications, and primarily consists of porosity detection and geometric measurement. In situ monitoring of AM fabrication can exploit the unique layer-wise nature of AM to create a 3D map of a component given a series of 2D data sets for each layer using the methods discussed in Section 3.2.1. Although in situ techniques can inform potential areas of porosity, for qualification, final porosity and geometry testing should occur after all post-processing treatments such as HIPing, heat treatments, and precision machining. However, the geometric complexity of AM components and frequent mixture of fine details with bulk structures add significant challenges to accurate measurement. Work on nondestructive testing of metal AM components has been published [223] and is an active area of research given commercial interest in fabricating critical components that require inspection and certification.

Porosity in a final component must be characterized with techniques that are sensitive to the size range and type that will impact mechanical properties, particularly fatigue strength. Existing standards for porosity such as ASTM E186 - 15 for cast steel walls may provide useful reference upon which to develop. Porosity can be characterized by average material density, number of pores, pore location, pore size distribution, and pore morphology. Comparing a component's actual density against theoretical density is the simplest characterization and can be achieved by the Archimedes principle [224]. Measurement of other aspects of porosity depend on the resolution desired, material properties (such as x-ray absorbance), and geometric considerations. CT is capable of pore resolution to 10 μm [225] and work has been published on CT pore measurement in laser welds [226,227]. Synchrotron radiation micro-tomography [228] has been used to detect pores with a resolution of 1.3 × 1.3 × 1.3 μm, but the measurement area was small at 1.3 × 1.3 × 10 mm. Although CT and synchrotron radiation micro-tomography are highly accurate, both methods are capital-intensive and may be unnecessary if a HIPing post-process treatment is standard for a component. In such a case, using the Archimedes principle to determine overall porosity and another method to detect large pores may be faster and more cost-effective.

Grain size and orientation can be characterized on the component surface via microscopy-based techniques such as electron backscatter diffraction [229]. Data on the internal microstructure are only possible with destructive methods. However, sacrificial startup specimens could be fabricated under the same processing conditions with the same feedstock and thereby offer a measure of assurance.

3.3.2 Witness Testing

"Witness testing" in the context of LPBF refers to the analysis of test specimens and coupons that are fabricated concurrently to end-use components. Witness coupons may be fabricated physically separate from end-use components or physically attached to end-use components (e.g., as a protrusion). Physically attached witness coupons may be left on end-use components in some applications and removed later to evaluate corrosion rates or irradiation embrittlement. Witness coupons are not required to be monolithic solid masses; hollow shapes allow for the capture of feedstock powder and effectively act as "time capsules." Theoretically, a hollow witness coupon may also provide data on the gaseous build chamber environment at the time it was sealed. Witness coupons may be spatially arranged in any manner around, above, or below end-use components, and may be located inside cavernous end-use components.

As discussed in Section 3.3.3.1.1, the microstructures of LPBF parts are a function of geometry and therefore, material properties are functions of geometry. Therefore, witness coupons should be carefully assessed and demonstrated to be representative of performance in end-use component geometries before being used for quantitative measurements such as fatigue life or fracture toughness. HIPing may or may not help address the microstructural and porosity concerns and facilitate the use of simplified test specimen geometry. For example, 316L may form ferrite, austenite, or a mixture of the two phases upon solidification depending on complex interactions of solidification velocity, thermal gradients, and heat transfer. Grain size and morphology are similarly affected by the same complex interactions. HIPing and/or solution annealing will completely transform the material to an austenite phase, but it is unclear at this time how the grain growth and final grain size distribution are affected by the initial phases and grain size. If the final grain size and morphology converges to a uniform distribution across the entirety of a component, then it is likely reasonable to substitute witness specimens or simplified geometries for sectioned end-use components. However, if recrystallization or grain growth vary with initial phases or grain size, then the grain size of the final HIPed microstructure will still be heterogeneous and a function of geometry. Such an evaluation will likely have to be conducted per alloy. In this example the strength of 316L is predominantly affected by grain size and the Hall-Petch relationship; however, the same fundamental concern of the initial microstructure affecting the final microstructure exists if the strengthening mechanism is lamella spacing, precipitate size, or solute trapping and is the motivation for scan strategy refinement to control and predict the as-fabricated microstructure. Another option when sectioning end-use geometries is not feasible is to perform functional evaluations of end-use geometries such as burst tests in conjunction with simplified test specimen geometries.

Witness coupons are suitable for build level measurements such as chemical composition and contamination (e.g., oxides) and for layer-specific measurements. Witness coupons may be used in conjunction with in situ monitoring as illustrated in Figure 41. In situ monitoring can inform investigation at specific locations, and witness coupons may provide empirical evidence of incomplete spreading, delamination, or other events that may result in component rejection. The optimization of witness coupons is not well understood at this time, and optimal witness coupon geometry, size, location, spatial orientation, and frequency have yet to be determined. Quantifying the efficacy of witness coupons and witness coupon/in situ monitoring synergy is an active area of research and a goal of ORNL's Transformational Challenge Reactor Program.

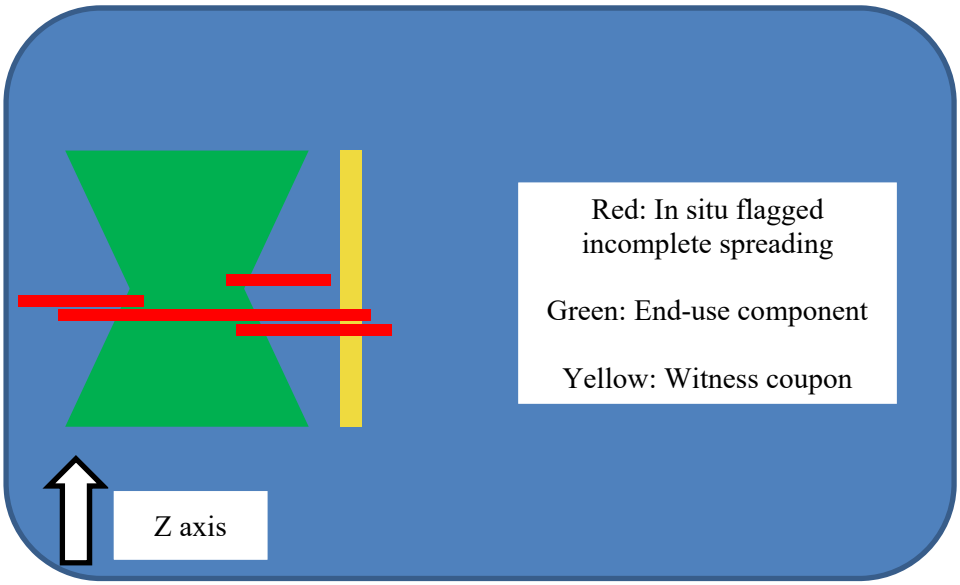

Figure 41. Illustration of in situ monitoring and witness coupon testing synergy.

3.3.3 Mechanical Testing

One of the most significant challenges with certifying and qualifying AM components is the variation and uncertainty associated with material performance. For many conventional manufacturing techniques, the material performance is extremely well understood. Larger blocks of material are produced that have very uniform, often isotropic material properties. The performance of this material can be easily tested with different methodologies. When specifically focusing on mechanical properties (but this is similar with all properties, including thermal, electrical, functional, structural, and others), samples can be easily extracted from the bulk material. Extraction can be done for large quantities of samples to ensure a high statistical repeatability. The challenge is not in understanding the material performance but forming the material into the geometry of the component being fabricated. In AM, the challenge is almost exactly opposite. The amount of geometric flexibility is significantly greater than conventional processes and assemblies such that nearly any geometry can be fabricated. However, the performance may be extremely difficult to quantify because of properties being a function of geometry. As representative specimens must be extracted from components rather than bulk ingots, limited testing can be performed. Because one must test the 3D printed material directly, the inherent cost per sample is typically greater than conventionally processed material and therefore, generating statistically significant quantities of data is expensive.

3.3.3.1 Conventional AM Microstructural Differences

Mechanical testing of LPBF 316L has revealed numerous differences compared with conventional 316L. LPBF 316L tends to form columnar grains oriented in the build direction (Z axis) [230] and frequently exhibits a preferred crystallographic orientation. This microstructure results in transversely isotropic material properties, and the as-fabricated and stress-relieved tensile properties of LPBF 316L are significantly higher than conventional 316L because of grain size refinement. Other properties such as fatigue, corrosion-assisted fatigue, and SCC have higher or lower performance relative to conventional 316L depending on orientation. HIPed and solution-annealed LPBF 316L typically performs comparably to conventional 316L but is superior in some properties such as SCC resistance for unknown reasons. Cellular sub-grains on the scale of 500 nm [231] have been observed in as-fabricated and stress-relieved LPBF 316L microstructures but are not observed in conventional 316L. Similarly, Si- and Mn-rich nanoscale oxide inclusions are observed in the microstructure of LPBF 316L but not in conventional 316L. Porosities of varying size and morphology distributions are also observed in LPBF 316L; porosity is not observed in conventionally machined and forged 316L but may be observed in cast components. The long-term effects of the LPBF 316L microstructure—in particular, the cellular sub-grain structure—on corrosion and irradiation resistance and its microstructural stability are largely unknown at this time.

3.3.3.1.1 Geometry Influence on AM Microstructure

In conventional manufacturing, material properties are independent of a component's geometry. Large quantities of homogeneous and uniform samples can be sourced from the same ingots or batches as components to form statistically significant quantities of test data. The challenge with conventional manufacturing is in forming material to the desired shape rather than in characterizing material properties. In AM, the problem is reversed. AM allows for virtually any geometry, and components can be designed with minimal stress concentrations or with internal cooling channels to name a few possibilities. However, geometry directly affects the microstructure formed and material properties caused by heat transfer. Understanding and quantifying how geometry and the size of a component affect material properties in 3D space is nontrivial and encompasses a vast area of research within AM.

Leicht et al. [232] fabricated vertical thin (0.2 to 3.0 mm) walls out of 316L. The authors observed that 0.2 mm thick walls formed small grain randomly textured microstructures. Large columnar grains with a

predominant 101 inverse pole direction were observed with increasing wall thickness, and were the dominant microstructure at a wall thickness of 3.0 mm. Figure 42 [49] illustrates the transformation in microstructure as wall thickness increases.

Leicht et al. also fabricated thin wall overhangs at 30° and 45° to horizontal. Despite being relatively thick, the microstructure formed was randomly textured and without the dominant 101 direction observed in the vertical walls. Figure 43 [232] illustrates the effect of an overhang angle on microstructure Tancogne-Dejean et al. [233] inadvertently observed qualitatively similar results when exploring LPBF-fabricated lattice structures of 316L.

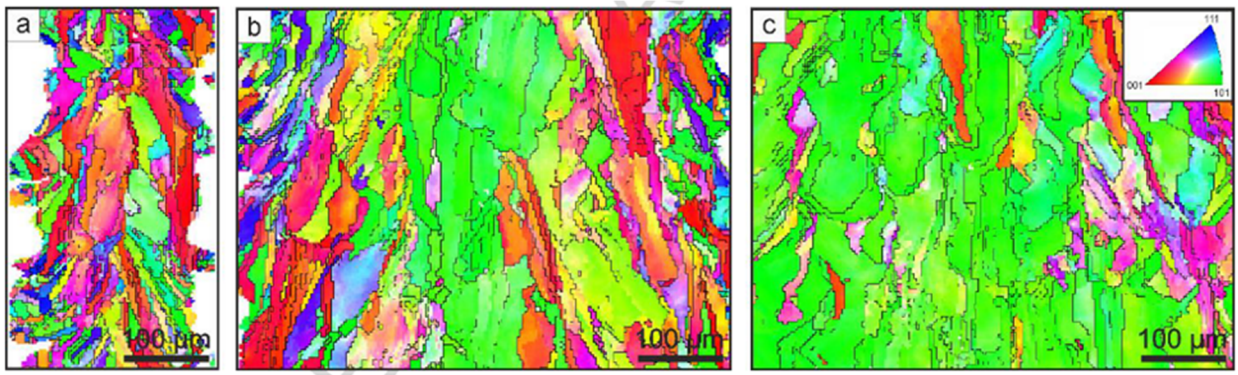

Figure 42. Electron backscattering diffraction orientation maps of (a) 0.2 mm, (b) 0.6 mm, and (c) 3.0 mm thick 316L walls [232]**.**

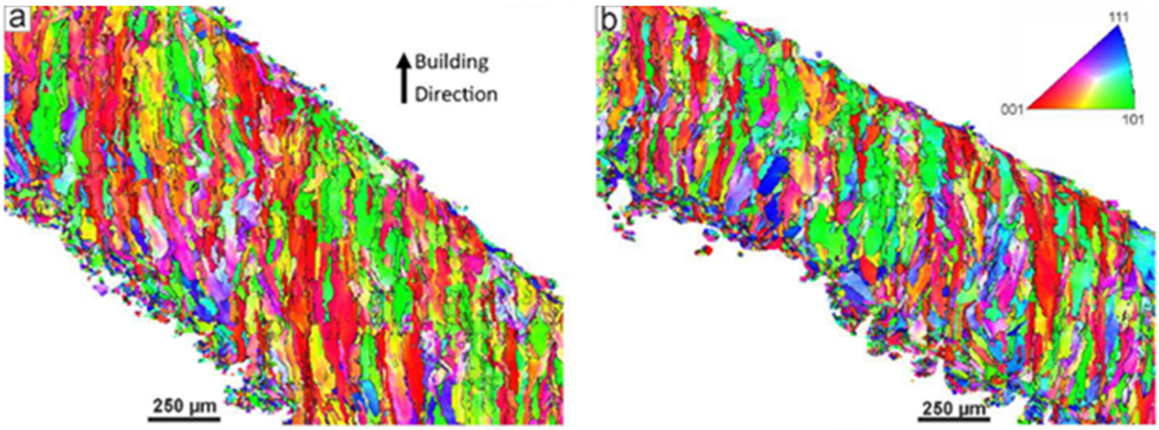

Figure 43. Electron backscattering diffraction orientation maps of (a) 45° overhang and (b) 30° overhang [232]**.**

The microstructure directly relates to the thermal history of each sub-portion of a component, and the thermal history directly relates to the processing parameters and geometry of a component. Multi-physics simulations can offer approximations of solidifications rates and expected microstructures but are computationally expensive and take significant amounts of time to run. A simpler method that offers a higher factor of safety is to use the lowest property values from each microstructure observed. Areas that are predicted to experience higher stress loadings or are more difficult to inspect in service could be qualified with the true material properties of the local microstructure and undergo more stringent testing, whereas areas with low demands on material performance could use the lowest values of mechanical properties. Such a flexible mixed method would allow for qualification based on empirical data while reducing sampling requirements on low requirement components and allowing true higher performance values to be used in critical components.

ORNL staff have also identified the potential for systematic differences in porosity in the skin and interior regions of components. For example, a cylinder may be fabricated such that the interior of the cylinder has a porosity average of 0.1% and the 50 µm outermost surface or "skin" has an average porosity of 1%. Provided that the cylinder is sufficiently large, the high porosity in the skin region will not significantly affect the ductility of highly malleable materials such as 316L—even without machining. However, if the same scan strategy is used to fabricate a 100 µm thick wall for a heat exchanger, the entire cross-section will exhibit an average porosity of 1% and material properties will not be equivalent to test data. Figure 44 illustrates such an occurrence. Such occurrences are frequently due to different processing parameters for the skin and interior regions of a component.

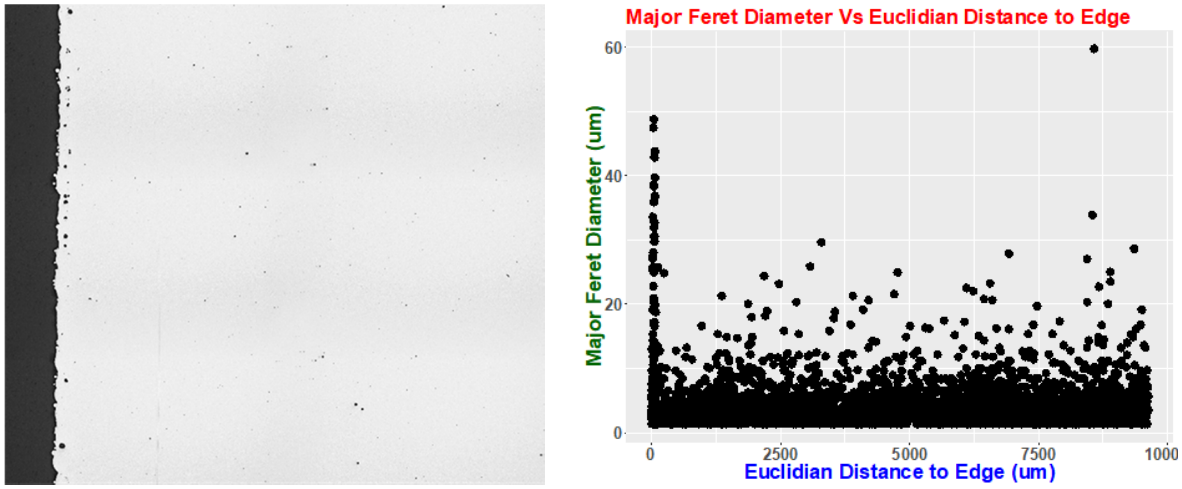

Figure 44. Example of systematic porosity variation in skin and interior regions of LPBF components.

3.3.3.1.2 Processing Influence on AM Microstructure

The microstructure of LPBF materials is affected by the processing parameters of the LPBF machine (e.g., laser powder, velocity, spot size), by the geometry of the component, and by post-processing heat treatments. Of these three factors, the effects of heat treatments on microstructures is the most predictable for 316L. Little microstructural change is observed up to 800°C when melt pool boundaries begin disappearing because of diffusion, and grain growth appears to be limited below 1,040°C [231]. Solidified microstructures depend on the size and geometry of a component as well as the processing parameters due to heat transfer. Generalized effects of geometry on 316L microstructure are discussed in Section 3.3.3.1.1. Meaningful empirical comparisons of LPBF machine processing parameters are extremely difficult because of the lack of an accepted standard geometry, inter-vendor hardware variation, inter-vendor software variation, and incomplete reporting, to name a few complications. However, there are two broad methods of empirical comparisons: direct parameter modeling and reduced-order surrogate models. Numerical simulations of solidification structures and melt pool characteristics have been published, but accurate modeling is complicated by the need for multi-scale simulation methods to reduce computational expense. Therefore, determining the effect of a particular processing parameter combination on a given geometry is frequently most accurately and quickly accomplished by fabricating and destructively evaluating the microstructure.

Direct parameter modeling attempts to create process parameter maps directly from independent variables such as laser powder, velocity, beam spot size, layer thickness, or hatch spacing and is borrowed from welding literature and practice. The most common direct mapping combination is laser power vs. velocity, as illustrated in Figure 45[49].The difficulty with direct mapping is that only two or three variables can be illustrated at once and any change to other variables necessitates additional graphs. An alternative is reduced-order surrogate models, which approximate process outcomes. Two of the most common surrogate models are linear energy density (LED) and volume energy density (VED), which respectively are power per length and power per volume ratios. Disagreement exists as to whether spot size or hatch spacing should be used in calculating VED; LED and the two forms of VED are respectively presented in equations 1-3. Increasing VED has been broadly associated with reduced lack of fusion porosity [70,234–236]. However, VED and LED have limitations in applicability [237,238] as illustrated in Figure 46 [238]. To the authors' knowledge, the only reported as-fabricated microstructure of LPBF 316L is the cellular structure observed in Figure 20. Variations of LPBF machine parameters all appear to form the same microstructure [231,239,240]; however, the cellular grain size appears to relate to LED with higher power to velocity ratios resulting in larger cells [239].

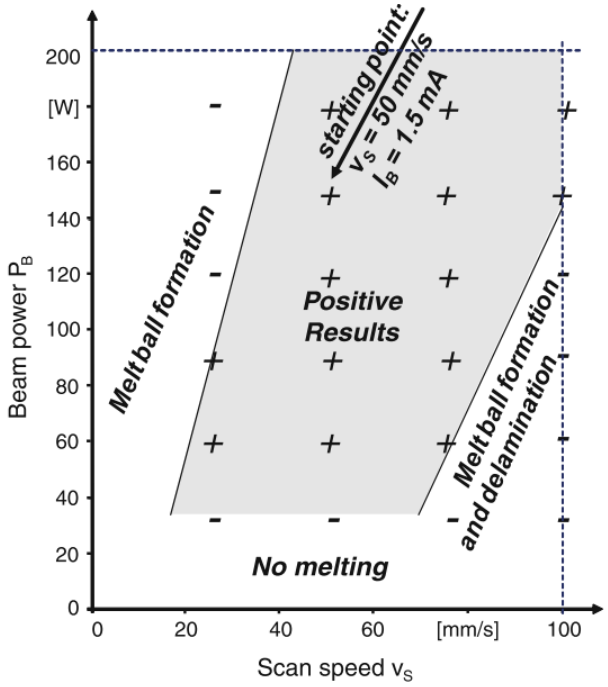

Figure 45. Example of direct parameter modeling [49]**.**

$$LED = \frac{P}{V} \tag{1}$$

$$VED_{Hatch} = \frac{P}{VLH} \tag{2}$$

$$VED_{Spot\ Size} = \frac{P}{VLS} \tag{3}$$

Where P is power (W), V is velocity (mm/s), S is spot size (μm), H is hatch spacing (μm), and L is layer thickness (μm).

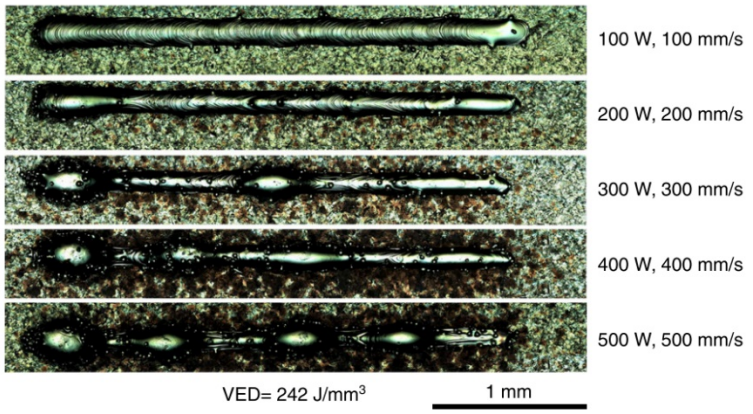

Figure 46. Example of melt pool variation for constant VED and LED [238]**.**

3.3.3.2 Microstructural Influence on AM Performance

Reduced grain size in LPBF 316L results in higher UTS and YS relative to conventional 316L as predicted by the Hall-Petch relationship. The elongated grains of LPBF 316L result in a transversely isotropic material where the build direction (Z axis) exhibits decreased UTS and YS and increased elongation relative to the X-Y plane [129]. Fatigue properties of stress-relieved LPBF 316L are superior for cracks growing in the X-Y plane relative to cracks growing in the X-Z or Y-Z planes. Fatigue cracks growing in the build direction (Z axis) propagate along grain boundaries, whereas fatigue cracks in the X-Y plane grow through grains as illustrated in Figure 15. Section 2.4.1 discusses the behavior of fatigue crack growth in LPBF 316L in depth and provides experimental results. Larger grains in solution-treated LPBF 316L relative to stress-relieved LPBF 316L have been reported to reduce SCC crack growth rates; however, it is unclear whether the reduced crack growth rate directly results from larger grains or is influenced by the confounding effect of fewer grain boundaries resulting in fewer oxide inclusions at grain boundaries.

The effects of cellular sub-grains observed in as-fabricated and stress-relieved LPBF 316L on material properties are not clear at this time. Conflicting experimental results of increased vs. decreased resistance to void swelling in as-fabricated and stress-relieved LPBF 316L relative to conventional 316L have been reported [146,148,153]. Curiously, HIPed + solution HT LPBF 316L has been reported to exhibit significantly higher void swelling resistance relative to conventional 316L [146,152]; however, the heat treatment of the conventional 316L in the study was not specified. At this time, it is unclear whether the difference is due to incomplete reporting of the conventional sample's heat treatment or an uncharacterized difference in microstructures between solution-treated LPBF 316L and solution-treated conventional 316L. Solution-treated LPBF 316L is expected to have a microstructure nominally similar to conventional 316L and without cellular sub-grains.

Nanoscale oxide inclusions in LPBF 316L have been documented to significantly accelerate SCC crack growth rates [146]. Oxide inclusions are likely formed by species preferential oxygen scavenging of particles heated but unmelted by the laser or melt pool. Reducing Si, and possibly Mn, content in powder feedstock may reduce oxide formation to acceptable levels.

Porosity in LPBF 316L detrimentally affects tensile properties—most noticeably, ductility [129–132] and fatigue—because of acting as crack nucleation sites, and SCC crack growth rates [146]. At the time of this document's publication, clear relationships have not been established between material properties and pore frequency, pore size, pore morphology, or total void fraction.

3.3.4 Environmental Testing

Prescribing qualifications and testing procedures for environmental degradation of LPBF components is difficult given the lack of studies on the topic, particularly for SCC and IASCC as encountered in NPP environments. To date, the only study published on the topics of SCC and IASCC is GE's report to DOE [146], which has also been republished in other forms [152,241]. GE reported that cold working (without subsequent heat treatments), high porosity, and nanoscale oxide inclusions increased SCC crack growth rates [146]. HIPing + solution heat treatment was observed to reduce SCC crack growth rates, but the primary cause is unclear between intra-crystal changes and a volume reduction of grain boundaries (and therefore oxide inclusions at grain boundaries). HIPed + solution-treated LPBF 316L and stress-relieved LPBF 316L in the build plane (X-Y) were observed to have crack growth rates comparable to conventional 316L. Stress-relieved LPBF with cracks in the build direction (X-Z and Y-Z planes) was observed to have significantly higher (~3×) crack growth rates due to cracks propagating at grain boundaries rather than through grains.

A thorough critique of GE's report is presented at the end of Section 2.4.1; however, a summary of further needed research for 316L is as follows. Oxide inclusions, specifically SiO_2, accelerate SCC crack growth rates. Therefore, minimizing Si content in feedstock beyond the ASTM F3184 - 16 maximum allowable concentration of 1% Si may be necessary to reduce the frequency of Si-rich oxide inclusions. Inspection of virgin feedstock powder for SiO_2 inclusions may be required, and SiO_2 may limit the number of reuses a powder batch can undergo. Mn content may also be a concern, but it is unclear at this time because of the preferential formation of SiO_2. The effect of cellular sub-grains observed in as-fabricated and stress-relieved LPBF 316L on material properties is unclear at this time, as is sub-grain stability over time and temperature. GE's study evaluated IASCC under isostatic strain; isostatic stress IASCC testing is recommended to determine whether crack propagation varies by loading type.

3.3.5 Joining and Welding of LPBF Components

At the time of this document's publication, most LPBF machines have a build volume of approximately 250 to 300 mm cubed, limiting the size of fabricated components. To assemble larger AM components or join AM components to conventionally manufactured parts, welding is required. A limited number of studies have been published on welding LPBF metal to LPBF metal [242], LPBF metal to conventional metal [243], and the effects of heat-treating LPBF components before welding [243]. In general, LPBF 316L can be welded to other LPBF 316L components or to conventional components with acceptable performance, but the weld shape, welding parameters, and HAZ size and microstructure are not directly transferable from the current knowledge base of conventional 316L.

3.3.5.1 LPBF to LPBF

Matilainen et al. [242] evaluated a factorial design of laser welding parameters on both conventional cold-rolled and as-fabricated LPBF 316L. It was observed that LPBF 316L–LPBF 316L formed welds with more uniform cross-sections than conventional 316L for many parameter combinations; conventional 316L formed hourglass cross-sections under many combinations whereas LPBF 316L tended to form columnar welds. Multiple parameter combinations were observed to fully penetrate when LPBF 316L was welded but only partially penetrate when conventional 316L was welded. Matilainen et al. postulated that the higher surface roughness of LPBF 316L resulted in higher absorptivity rates and therefore more energy transfer to the weld. LPBF 316L demonstrated a tendency to form porosity in welds with a laser power of 1.5 kW and centerline cracks in welds with a laser power of 4 kW; conventional 316L did not demonstrate the tendency for centerline cracking or porosity. Qualitatively, LPBF 316L may form more uniform welds with deeper penetration but in narrower welding parameter ranges than for conventional 316L. HAZ were not reported by Matilainen et al.

3.3.5.2 LPBF to Conventional

Laitinen [244] investigated welding conventional 316L to as-fabricated LPBF 316L and observed that the weld shape sharply contrasted depending on the base material. The half of the weld adjacent to the conventional 316L base material consistently took on an hourglass shape whereas the half of the weld adjacent to the LPBF 316L base material took on a columnar shape (i.e., the weld bead was uniform in diameter) consistent with the research from Matilainen et al. [242]. Critically, the weld microstructure also differed with base material. LPBF 316L propagated a dendritic microstructure in adjacent weld material whereas conventional 316L propagated a mixed dendritic/planar microstructure. Ferrite content in the range of 0.8 to 3 wt % was reported in all welds, but accuracy was questionable because a feritscope was used, which requires manual probe tip placement. Therefore, it is unclear at this time whether the dendritic weld microstructures were austenite or ferrite, as well as the phase of the planar microstructure observed. Depending on whether ferrite is formed in the weld, a solutionizing heat treatment may be necessary.

Kuryntsev [243] tested welding LPBF stainless steel PH1 and conventional cold-rolled stainless steel 321 under two welding laser powers, three heat treatments for the LPBF PH1, and as-fabricated PH1 as a control. The compositions of PH1, 321, and 316L are presented in Table 9 for reference. The pre-welding heat treatments of LPBF PH1 (1,050°C for 90 min, 650°C for 90 min, 500°C for 90 min, and no heat treatment) did not significantly affect the size or morphology of welds, and in all welds, the weld preferentially expanded into the conventional cold-rolled 321. The conventional 321 did not exhibit a HAZ and retained its original austenite phase whereas the LPBF PH1 formed a HAZ of martensite, troostite, or bainite. The weld phases formed were a mixture of austenite and the PH1 HAZ phase. Tensile testing of the weld joints revealed that only solution HT PH1 failed, and did so in the PH1 HAZ. All other heat treatments and the as-fabricated state plastically deformed out of the testing fixture rather than failing. The tensile test was not per ASTM E8 with a machined neck but rather a custom fixture. Because of the significant compositional variation between 316L and PH1, the results are not directly comparable. However, the results suggest that traditional welding concerns such as the YS, ductility, and phase(s) of the base material are still relevant and are affected by pre-welding heat treatments. To the authors' knowledge, no studies have been published to date on pre-welding heat treatments of LPBF 316L.

Table 9. Weight percent compositions of stainless steel 321, PH1, and 316L.

Alloy	C	N	Si	Mn	Mo	Nb	S	P	Cr	Ni	Ti	Cu	Fe
321	<0.08	<0.10	<0.75	<2.00	—	—	<0.03	<0.045	17–19	9–12	<0.70	—	Bal
PH1	<0.07	—	<1.00	<1.00	<0.50	0.15–0.45	<0.03	<0.04	14–15.5	3.5–5.5	—	2.5–4.5	Bal
316L	<0.08	<0.10	<0.75	<2.00	2–3	—	<0.03	<0.045	16–18	10–14	—	—	Bal

3.3.6 In-Service Considerations

Two primary considerations for the in-service lifespan of a component are inspections and component aging. At this time, few case examples exist of age-related LPBF component failure to guide recommendations on either topic, and none in nuclear environments. Nevertheless, a review of the capabilities of LPBF and differences in microstructures between conventional and LPBF microstructures offers some insight toward developing inspection protocols and predicting component lifespans.

3.3.6.1 Inspection

In general, components in NPPs do not fail from mechanical overloading but rather age-related degradation such as corrosion, cracking (e.g., fatigue, SCC), and effects related to irradiation

embrittlement. Therefore, inspection should focus primarily on preventing, detecting, and monitoring age-related degradation. Developing inspection protocols for new technologies requires a reevaluation of assumptions and existing procedures, perhaps best performed through the Socratic method: what, how, when, where, and why measurements should be taken.

Determining what measurement should be taken is impossible without knowing the function of a component; however, surface roughness has long been known to affect fatigue strength, SiO_2 inclusions have been identified to detrimentally affect SCC (see Section 2.4.1), porosity is known to affect fatigue life, and Cr depletion at grain boundaries is known to accelerate SCC. Metallographic samples may be cut from built-in component coupons or "witness" parts from the same build and inspected for inclusions and grain boundary Cr depletion with the assumption that the witness part is representative of the component chemistry. Surface roughness may similarly be determined from witness parts or via white light or laser scanning of the actual component. White light or laser scanning will also inform dimensional accuracy of components. Porosity averages and size distributions may be assumed via sacrificial startup parts, but CT scans of components will only detect large or concentrated porosity in final components. In situ monitoring can inform higher resolution targeted CT inspection of specific locations that have been flagged for possible manufacturing discontinuities.

How measurements should be taken is a question of techniques and depends on the techniques available and required resolution. Unpublished work by the authors indicates via a first principles derivation that the uncertainty of volumetric porosity measurement techniques such as the Archimedes method and pycnometry increases with decreasing porosity, whereas cross-sectional porosity measurement methods have decreasing uncertainty with decreasing porosity [245].

The remaining three questions of when, where, and why are best answered together. Geometric flexibility is AM's greatest advantage and also its greatest difficulty in performance quantification. Organic shapes, internal channels, and design flexibility frequently allow for minimization of stress concentrations in LPBF components. In some instances, reducing assemblies of dozens of parts into single components may be possible, as with GE aviation's fuel nozzle [7], and when assembly is still required, locating bolts or welds in more accessible locations may be possible. However, component microstructure and therefore performance varies with geometry. Therefore, the maximum stress specification in an overhang may be different than in a vertical section of a component. For as-fabricated and stress-relieved 316L, the variation in microstructure due to geometry also informs the direction cracks (fatigue and SCC) are most likely to travel should they nucleate (i.e., in the build direction). Without post-process machining or shot peening, the underside of overhangs has the highest surface roughness and may nucleate cracks at a faster rate than vertical or top surfaces of LPBF components. At this time, how frequently LPBF components should be inspected is unclear; however, preliminary results by Rebak et al. [146] indicate that high-cycle corrosion fatigue cracks in LPBF 316L grow at an accelerated rate relative to conventional 316L and low-cycle corrosion fatigue cracks grow comparably to conventional 316L. Results by Riemer et al. [140] suggest that un-corroded fatigue crack growth rates are predictable and have defined fatigue limits given the orientation and heat treatment of a component.

3.3.6.2 Aging Management

Planning for aging management of LPBF components in NPPs is currently conceptual as no additively manufactured components have seen service and therefore no empirical observations of age-related degradation exist. However, the limited testing that has been published to date on time-dependent failure mechanisms such as SCC and corrosion fatigue suggests that degradation modes in LPBF components do not fundamentally differ from conventionally manufactured components; rather, the rate at which degradation occurs differs between conventional and LPBF manufacturing. Some degradation modes, such as irradiation void accumulation, appear to occur significantly slower in LPBF material than in

conventional material [146], whereas other degradation modes, such as high cycle corrosion fatigue, are accelerated in LPBF material relative to conventional material [146]. One potential advantage of LPBF components is the geometric ability to build in redundancy such as spare internal channels for fouling and clogging, designing to minimize welds, placing welds in accessible locations, and built-in sensors such as thermocouples.

A potential concern for as-fabricated and stress-relieved LPBF 316L is growth in the size of cellular sub-grains at elevated temperatures. As discussed in Sections 2.4.2 and 3.3.3.2, a consensus on the effects of cellular sub-grains on LPBF 316L material properties has not been reached. Cellular sub-grains in stress-relieved LPBF 316L have been reported to be stable after 30 min at 400°C [153]; however, it is also unclear at what rates sub-grains grow at temperatures above 400°C. Therefore, the material properties may change as a function of time and/or temperature if the reactor design operates above 400°C; more studies are needed to explore this possible microstructural phenomenon.

3.4 TECHNICAL GAP ANALYSIS

The following technical gap analysis is written with a focus on the performance of a final component produced for a nuclear application. The importance of each topic is rated according to its potential impact on material properties and does not correspond to a specific material property or failure mode. For example, contamination management is rated as highly important because contamination may adversely affect SCC resistance, ductility, or the as-fabricated microstructure in unpredictable ways. Feedstock contamination would be an adverse influence regardless of whether a component experienced radiation or a corrosive environment.

Table 10:LPBF Fabrication Gaps

Importance	Topic	
High	Software and File Control	
	Related In-Document Sections	3.1.1
	Ranking Rationale	Significant potential to alter material properties, porosity, and geometric accuracy
	Discussion	The scan strategy used to fabricate a component and the software controlling the LPBF machine has an extremely important role in geometric accuracy, warping, material properties, and the probability of successfully completing a build. It is critically important that the exact same file, LPBF software version, and LPBF software settings be used to fabricate replicates of a given qualified component. As a result, cybersecurity, database traceability, disabling automatic software updates and similar items are highly important to ensuring end use component quality.
High	Material Property Sampling Methodology	
	Related In-Document Sections	3.5.1 3.5.2
	Ranking Rationale	Significant risk of overestimating material properties or underestimating variability.
	Discussion	Heterogeneous LPBF microstructures and material properties have been documented in literature and are functions of the scan strategy, feedstock, component geometry, and LPBF machine. Heterogeneity in material properties should be assumed until sufficient empirical evidence is presented otherwise. The sampling methodology for quantifying the mean, variance, skew, and kurtosis of

		LPBF material properties in four-dimensional space (X,Y,Z, orientation) is significantly more involved than in conventional materials.
High	Planned and Unplanned Build Interruptions	
	Related In-Document Sections	3.5.1 3.5.2
	Ranking Rationale	May adversely affect material properties or component geometry.
	Discussion	Build interruptions may affect the thermal distribution within the build chamber by cooling, which may result in non-negligible component warping prior to restarting the build. Depending on the cause of the interruption, several adverse events may occur. Exhaustion of inerting gas may result in oxidation of multiple layers, electrical power outages may require recalibration of the laser optics, and laser overheating may result in build failure to name a few possibilities.
High	Geometry-Scan Strategy Interactions	
	Related In-Document Sections	3.3.3.1.1
	Ranking Rationale	May result in incorrect geometry, adversely affect material properties, or produce manufacturing defects.
	Discussion	Geometry-scan strategy interactions may significantly change the meltpool solidification rate and local thermal profile. Components with mixtures of monolithic and fine features and significantly changing cross-sectional areas in the build direction are at highest risk of adverse interactions.
High	Contamination Management	
	Related In-Document Sections	2.2.1.1 3.1.2
	Ranking Rationale	Significant potential to alter material properties
	Discussion	Contamination of feedstock powder is a serious concern as contamination may adversely affect material properties. Contamination can typically be reduced to acceptable levels by general cleanliness and dedicating LPBF machines to specific alloys. Documenting a lack of contamination may be accomplished in parallel with quantifying powder characteristics. The authors recommend sampling sieved powder prior to each build and storing said powder sample for the lifespan of related components as security should further feedstock analysis be warranted.
Medium	LPBF Environmental Sensor Data	
	Related In-Document Sections	3.1.3.4
	Ranking Rationale	May detect layer-wise component defects
	Discussion	Data from environmental sensors in the LPBF machine (e.g. oxygen sensors), do not provide information as spatially specific as in-situ monitoring, but are typically more accurate and the underlying technologies thoroughly documented. Events during fabrication that are captured by environmental sensors are likely to affect entire layers. The authors recommend analysis of environmental sensor data for all builds; determination of what environmental data is relevant to 316L in NPP applications must be empirically resolved as data becomes available.
Medium	Powder Characterization	
	Related In-Document Sections	2.2.1

	Ranking Rationale	Affects powder application uniformity, which in turn affects incomplete spreading, recoater chatter, and recoater streaking.
	Discussion	Powder feedstock characterization includes size distribution, morphology, internal porosity, and flowability. Said characteristics qualitatively affect the uniformity of powder layers, which in turn may result in incomplete spreading, lack of fusion porosity, and delamination. Such detrimental events occur probabilistically but can frequently be empirically correlated to feedstock characteristics. Relevant feedstock characteristics depend on the LPBF machine, component geometry, and scan strategy used. Powder re-use acceptance/rejection depends on routinely sampling and characterizing powder after sieving.
Medium	Witness Specimens	
	Related In-Document Sections	3.3.2 3.3.6.1
	Ranking Rationale	May detect layer-wise and chemical composition defects.
	Discussion	Witness specimens afford the possibility of capturing layer-wise defects such as incomplete spreading via destructive metallographic sectioning and can reasonably be assumed to share the same chemical composition as end-use components from the same build. Hollow witness specimens may be used to encapsulate powder samples for later investigation if warranted.
Medium	LPBF Machine Calibration	
	Related In-Document Sections	3.1.3
	Ranking Rationale	Potential to alter material properties and geometric accuracy.
	Discussion	LPBF machines must be calibrated in order to operate at specified parameters (e.g., laser power, spot size) in order to repeatably fabricate components, particularly when using the same scan strategy for multiple machines. It is unclear at this time how precisely machines must be calibrated.
Low	Residual Stress – Warping, Cracking, and Delamination	
	Related In-Document Sections	2.3.2 3.2.2 3.2.3
	Ranking Rationale	Potential for geometric inaccuracy and catastrophic part failure prior to entering service.
	Discussion	All LPBF components experience significant as-fabricated residual stress which must be removed via post-processing heat treatments. Residual stress is not problematic provided that an appropriate heat treatment is applied prior to entering service; however, high residual stress can result in geometric inaccuracy which may result in component rejection. High residual stress may also result in cracking and delamination, however, these events are not commonly associated with 316L and may typically be visually detected.
Low	Sieving System	
	Related In-Document Sections	3.1.2
	Ranking Rationale	Little risk of adverse effects provided sieves are inspected and contamination prevented.

	Discussion	Sieving feedstock is a necessary aspect of LPBF to recover feedstock. Sieves must be periodically inspected and replaced and steps taken to prevent feedstock contamination during the sieving process.
No-Feedback – Low Feedback – High	In-Situ Monitoring and Feedback	
	Related In-Document Sections	3.2.1
	Ranking Rationale	In-Situ monitoring with no feedback poses no risk, in-situ monitoring with feedback control may adversely affect material properties.
	Discussion	In-situ monitoring without feedback control may inform more targeted CT inspection of components but poses no risk. In-situ monitoring with feedback control may adversely affect material properties. At this time, it is unclear how risk varies with the type of feedback (e.g., reapplying a powder layer, adjusting laser parameters, adjusting environmental parameters) and how corrective actions should be documented.
Application-Specific	Porosity Measurement	
	Related In-Document Sections	2.2.1.2 2.3.2 2.4.1 2.4.2
	Ranking Rationale	Porosity directly and adversely affects multiple material properties. The importance of porosity quantification depends on whether the affected properties are required during component service.
	Discussion	The importance of porosity measurement depends on component application. Porosity is known to adversely affects fatigue life, SCC, and IASCC. High (>1%) porosity adversely affects ductility in 316L. The Archimedes method may be used to determine the average density, and CT may be used to locate pores >10μm diameter.
Application-Specific	LPBF Design Considerations	
	Related In-Document Sections	2.2.3 3.1.1.2
	Ranking Rationale	Potential for creating stress concentrators and heterogeneous microstructures.
	Discussion	The greatest strength of LPBF is the geometric freedom to create simplified assemblies, organic shapes, and optimize load paths. However, design reviews must be conducted to prevent unintentional defects. For example, assume that a conventional component with a machined through hole is replaced with a LPBF component. The hole path in the LPBF component may be made serpentine, non-uniform in diameter or similarly non-conventional to optimize pressure head losses, etc. However, a non-line of sight hole will prevent milling to improve surface roughness and the 45 degree overhang limitation of LPBF may result in diamond or triangular shape holes, which will create significant stress concentrations. Designs must also consider the inspectability of such features. These design byproducts do not prevent the use of LPBF components, but special consideration must be given to designs in light of the limitations of the LPBF process.

The following material property and performance gap analysis is written with the conventionally manufactured version of the alloy as a comparison. Ranking is assessed on whether the LPBF version of

the alloy exceeds the conventionally manufactured material properties and the frequency of a given failure mode. For example, tensile properties of LPBF 316L are assessed as low importance because LPBF YS and UTS are typically higher than in conventionally manufactured 316L. Additionally, failure due to mechanical overloading is not a common failure mechanism in NPP applications.

Table 11: Material Property and Performance Gaps

Importance	Topic	
High	Heterogeneity	
	Related In-Document Sections	3.3.3.1.1
	Ranking Rationale	Significant risk of overestimating material properties.
	Discussion	"Microstructural heterogeneity" refers to 3D nonuniformity in the microstructure of a component and is not to be confused with anisotropy. "Anisotropy" refers to whether material properties are uniform in all directions (as in common in conventional metallic materials) or are transversely isotropic (as is common in columnar microstructures). Simple blocky geometries are less likely to suffer from heterogeneity; however, such geometries do not take advantage of the geometric flexibility afforded by LPBF. Heterogeneity may appear in multiple forms singularly or in groups. For example, a component with equiaxed grains is heterogeneous if the grain size varies significantly from one region to another within a component. A second example is if a component exhibits columnar grains in one region and equiaxed in a different region. A third example is if porosity varies significantly within a component with respect to pore size, counts per volume, pore morphology or volume percent. In all examples, the average material properties change as a function of location within a component. Heterogeneity may affect a single material property or may affect multiple properties simultaneously. It is necessary, at a minimum, to characterize the minimum property values within a heterogeneous component. Depending on component application and requirements for a failure modes and effects analysis, it may be necessary to quantify the heterogeneity of a component in four-dimensional space (X, Y, Z, orientation).
High	Irradiation-Assisted Degradation	
	Related In-Document Sections	2.4.2
	Ranking Rationale	Irradiation embrittlement and void formation are potential concerns in NPP applications. However, it is unclear at this time at what rate LPBF 316L ages relative to conventional 316L.
	Discussion	Irradiation embrittlement and particularly loss of fracture toughness is a concern in NPP applications. Studies to date have reported conflicting results on LPBF 316L irradiation void and loop formation rates and is it unclear how the dendritic microstructure of stress relieved 316L affects aging and how thermally stable the dendritic microstructure is.
High	SCC and IASCC	
	Related In-Document Sections	2.4.1 2.4.2
	Ranking Rationale	SCC and IASCC are two potentially significant failure modes in NPP applications.
	Discussion	Preliminary studies indicate that LPBF 316L may offer significantly higher SCC and IASCC resistance relative to conventional 316L given appropriate processing

		parameters and post-processing treatments. Porosity, grain size, and Si oxide inclusions have been identified as highly correlated to crack growth rates.
Low	Tensile Properties	
	Related In-Document Sections	2.4.1 2.4.2
	Ranking Rationale	Tensile properties of LPBF 316L are typically comparable or superior to conventional 316L. Failure due to mechanical overloading is also not a common failure mode in NPP applications.
	Discussion	Yield and ultimate tensile strength of LPBF 316L is typically superior to conventional 316L due to grain size refinement and moderately depends on post processing heat treatments. The uniform elongation of LPBF 316L is approximately 50-60% but may be reduced by high (>1%) levels of porosity.
Medium	Fatigue	
	Related In-Document Sections	2.4.1 2.4.2
	Ranking Rationale	Fatigue failure is abrupt and LPBF 316L has been documented to have lower high cycle fatigue life (corroded and uncorroded) relative to conventional 316L.
	Discussion	The fatigue strength of LPBF 316L strongly depends on the post-processing heat treatment, load path, and component porosity. Low cycle fatigue life has been reported as comparable to conventional 316L, but high cycle fatigue life is reduced relative to conventional 316L. Surface roughness adversely affects fatigue life similarly to conventional 316L. Stress relieved LPBF 316L shows anisotropic fatigue strength and preferential crack growth directions due to the columnar microstructure.
Medium	Fracture Toughness	
	Related In-Document Sections	2.4.1 2.4.2
	Ranking Rationale	LPBF 316L fracture toughness has been reported as ~40% lower to ~50% higher relative to conventional 316L depending upon post-processing heat treatments.
	Discussion	The fracture toughness of LPBF 316L has been reported over a wide range of values and strongly correlated to porosity and post-processing heat treatments. Preliminary results indicate that LPBF 316L may have significantly higher fracture toughness relative to conventional 316L given appropriate processing parameters and post-processing treatments.
Low	Weldability	
	Related In-Document Sections	3.3.5
	Ranking Rationale	Relatively little literature has been published on welding LPBF 316L to date.
	Discussion	Existing studies have indicated that the welding behavior (penetration depth, weld cross-section, solidified microstructure) of LPBF 316L differs from conventional 316L all else equal. Optimal pre and post heat treatments are not characterized at this time, nor is the phase and chemical composition distribution of LPBF 316L welds. To the authors' knowledge, the aging rate and irradiation resistance of LPBF 316L welds has not been reported to date.

3.5 CODES AND STANDARDS GAP ANALYSIS

3.5.1 Overview of Codes and Standards Relevant to LPBF

At the time of this document's publication, ASTM has extensively collaborated with ISO in the creation of joint standards and specifications for AM processes, terminologies, and component requirements. Table 12 lists the ASTM and ISO prefabrication standards published at the time of this document's release. However, many AM-specific standards do not contain relevant original technical specifications but rather simply reference existing technical specification documents for conventionally fabricated materials, provide generic background information or terminology, or provide recommendations for procurement specifications. For example, ASTM F3184 specifies "Processing shall be conducted in accordance with applicable standards or as agreed upon by the component supplier and purchaser," "Condition and finish of the components shall be agreed upon by the component supplier and purchaser," and "Inspection criteria shall be agreed upon by the component supplier and purchaser." Further refinement of existing technical specifications for AM is needed, particularly for unique demanding applications such as NPP environments. For example, ASTM F3184 – 16 for LPBF 316L specifies an acceptable maximum Si content of 1.00 wt %; as discussed in Sections 2.4.1 and 2.4.2, the Si content of 316L used in NPP SCC-susceptible environments may need to be reduced to the range of 0.05 to 0.1 wt % to prevent Si oxide inclusions in the microstructure.

Standards not published by organizations not typically referenced is US procurement documents (e.g., ASTM, ISO, AWS, or NASA) are italicized and in red print; such standards are included for completeness and as potential starting points in developing NPP applicable standards. To the authors' knowledge, no codes or standards exist on joining and welding LPBF components. Table 12 through Table 19 document current codes and standards on LPBF or that are closely related (e.g., ASTM E11 for sieves).

Table 12. LPBF general prefabrication codes and standards.

Topic	Standard	Full name	Status
Terminology	ISO/ASTM 52900:2015	Additive manufacturing – General principles – Terminology	Existing
	ISO / ASTM52921 – 13(2019)	Standard Terminology for Additive Manufacturing—Coordinate Systems and Test Methodologies	Existing
Design	ISO/ASTM 52910:2018	Additive manufacturing — Design — Requirements, guidelines and recommendations	Existing
	ISO/ASTM52911-1: 2019	Additive manufacturing — Design — Part 1: Laser-based powder bed fusion of metals	Existing
Software requirements	ISO/ASTM52915: 2016	Specification for additive manufacturing file format (AMF) Version 1.2	Existing
Geometry capability assessment	ISO/ASTM52902: 2019	Additive manufacturing — Test artifacts — Geometric capability assessment of additive manufacturing systems	Existing

Table 13. LPBF feedstock codes and standards.

Topic	Standard	Full name	Status
Characterization	ASTM E2589	Standard Terminology Relating to Nonsieving Methods of Powder Characterization	Existing

	ASTM B822	Standard Test Method for Particle Size Distribution of Metal Powders and Related Compounds by Light Scattering	Existing
	ISO/ASTM 52907:2019	Additive manufacturing — Feedstock materials — Methods to characterize metal powders	Existing
	ASTM F3049 – 14	Standard Guide for Characterizing Properties of Metal Powders Used for Additive Manufacturing Processes	Existing
Internal Porosity specifications	No existing standards		—
Powder geometry specifications	No existing standards		—
316L chemical composition specifications	ASTM F3184-16	Standard Specification for Additive Manufacturing Stainless Steel Alloy (UNS S31603) with Powder Bed Fusion	Existing
316L phase specifications	No existing standards		—
Reuse specifications	No existing standards		—

Table 14. LPBF sieving system codes and standards.

Topic	Standard	Full name	Status
Terminology	ASTM E1638	Standard Terminology Relating to Sieves, Sieving Methods, and Screening Media	Existing
Mesh specifications	ASTM E2016	Standard Specification for Industrial Woven Wire Cloth	Existing
	ASTM E11	Standard Specification for Woven Wire Test Sieve Cloth and Test Sieves	Existing
	ISO 3310-1	Test sieves — Technical requirements and testing — Part 1: Test sieves of metal wire cloth	Existing
Initial testing methods	ASTM E2427	Standard Test Method for Acceptance by Performance Testing for Sieves	Existing
Atmosphere specifications	No existing standards		—
Mesh inspection specifications	No existing standards		—

Table 15. LPBF machine codes and standards.

Topic	Standard	Full name	Status
Process control	MSFC-SPEC-3717	Specification for Control and Qualification of Laser Powder Bed Fusion Metallurgical Processes	Existing
	AWS D20.1M	Specification for Fabrication of Metal Components using Additive Manufacturing	Existing
	ASTM/ISO 52904:2019	Additive manufacturing — Process characteristics and performance — Practice for metal powder bed fusion process to meet critical applications	Existing
	JSA JIS C 6180	*Measuring methods for laser output power*	Existing

Laser power measurement	*SAC GB/T 6360-95*	*Specification for laser radiation power and energy measuring equipment*	Existing
	GOST 25811	*Means measuring laser output average power – Types – Basic parameters – Measuring methods*	Existing
Laser spot size measurement	ISO 11146-1	Lasers and laser-related equipment — Test methods for laser beam widths, divergence angles and beam propagation ratios — Part 1: Stigmatic and simple astigmatic beams	Existing
	SAC GB/T 13741-92	*Testing method of beam diameter of laser radiation*	Existing
Laser power distribution measurement	ISO 13694	Optics and photonics — Lasers and laser-related equipment — Test methods for laser beam power (energy) density distribution	Existing
Process gases	ANSI/AWS A5.32M	Specification for Welding Shielding Gases	Existing
Laser dimensional control measurement	No existing standards		—
Atmosphere specifications	No existing standards		—

Table 16. LPBF in situ feedback and monitoring codes and standards.

Topic	Standard	Full name	Status
Feedback monitoring	ASTM WK62181	New Guide for Standard Guide for In-Situ Monitoring (IPM) of Metal Additively Manufactured Aerospace Parts	Draft

Table 17. NDE codes and standards.

Topic	Standard	Full name	Status
CT inspection specifications	ISO 15708-4	Non-destructive testing — Radiation methods for computed tomography — Parts 1 to 4	Existing
Weld inspection methods	DIN EN ISO 17635	Non-destructive testing of welds – General rules for metallic materials	Existing

Table 18. LPBF material properties codes and standards.

Topic	Standard	Full name	Status
Material property evaluation specifications	MSFC-STD-3716	Standard for Additively Manufactured Spaceflight Hardware by Laser Powder Bed Fusion in Metals	Existing
316L tensile specifications	ASTM F3184 – 16	Standard Specification for Additive Manufacturing Stainless Steel Alloy (UNS S31603) with Powder Bed Fusion	Existing
316L for nuclear applications	ASME Code Case	HIP and solution annealed UNS S31603 stainless steel produced using the LPBF Process	Draft

Testing methods	ASTM F3122	Standard Guide for Evaluating Mechanical Properties of Metal Materials Made via Additive Manufacturing Processes	Existing
Reporting requirements	ASTM F2971	Standard Practice for Reporting Data for Test Specimens Prepared by Additive Manufacturing	Existing
Recommended purchasing requirements	ISO / ASTM52901 - 16	Standard Guide for Additive Manufacturing – General Principles – Requirements for Purchased AM Parts	Existing

Table 19. LPBF post-processing codes and standards.

Topic	Standard	Full name	Status
Heat treatments	ASTM F3301 - 18a	Standard for Additive Manufacturing – Post Processing Methods – Standard Specification for Thermal Post-Processing Metal Parts Made Via Powder Bed Fusion	Existing
Welding	No existing standards		—

Many ASTM/International Organization for Standardization (ISO) joint standards for AM presently do not contain pertinent technical specifications but rather define general terminology or provide reference lists to existing standards on powder characterization, mechanical testing, document control, and so on. One reason for this is the considerable variation in industry goals; some manufacturers are more concerned with fatigue properties, others with geometric tolerances, and others with throughput. For the fabrication of NPP components, several technical requirements beyond current ASTM standards must be developed.

Quantitative powder recycling and sieving specifications must be developed to determine when used powder can no longer be reprocessed as well as how recycling occurs. Mesh size(s), mesh inspection, and sieving atmosphere oxygen and water content affect the rate of powder surface oxidation and content of fines and spatter present in feedstock material. Electron backscatter diffraction and/or x-ray diffraction of sieved powder may be necessary to verify that feedstock chemical composition and phases are within specification. Caution should be used in specifying chemical compositions identical to conventional manufacturing, as evidenced by the observation of SiO_2 inclusions in LPBF 316L.

Prefabrication build chamber and stage requirements for build plate flatness, levelness, and height control are recommended to ensure geometric tolerances are met, and specifications for post-fabrication build plate warping may be similarly necessary to prevent geometric distortion.

Laser calibration and alignment are critical for ensuring that the intended processing parameters are used during fabrication as well as for the geometric accuracy of components. Some aspects of laser calibration are unclear at this time. For example, lasers would ideally be calibrated at multiple locations across the build plate; however, the knife-edge and aperture methods for determining laser spot size require the laser beam to be perpendicular to the sensor, which would require complex rotational positioning of the sensor when the laser fires into corners of the build plate. Therefore, only calibrating lasers directly below the laser module is currently realistic.

Minimum requirements for material properties are undoubtedly the most critical and technically challenging specifications to be developed. To date, ASTM's approach has been to specify isotropic minimum requirements for additively manufactured components; this approach is conceptually simple and greatly simplifies designing. However, isotropic material properties are typically not realistic in

LPBF and accurate anisotropic properties are required for realistic simulations. It is unclear at this time whether porosity specifications should be documented separately or are de facto incorporated into minimum material property specifications such as fatigue life.

3.5.2 Analysis of Selected Highly Relevant Existing Codes and Standards

Multiple standards shown in Tables 12-19 supporting LPBF (e.g., sieve mesh specifications and feedstock characterization) have been applied in industry outside of NPP applications for decades and are well established. Standards and industry organizations have published standards and documents specific to LPBF in recent years, all of which have been identified as highly relevant to the development of LPBF standards for NPP applications and shown below in Table 20.

Table 20. LPBF documents highly relevant to establishing NPP codes and standards.

Organization	Document	Full name
NASA	MSFC-SPEC-3717	Specification for Control and Qualification of Laser Powder Bed Fusion Metallurgical Processes
NASA	MSFC-STD-3716	Standard for Additively Manufactured Spaceflight Hardware by Laser Powder Bed Fusion in Metals
AWS	AWS D20.1M	Specification for Fabrication of Metal Components using Additive Manufacturing
ISO	ISO/ASTM 52904:2019	Additive manufacturing — Process characteristics and performance — Practice for metal powder bed fusion process to meet critical applications
ASTM	ASTM F3184 - 16	Standard Specification for Additive Manufacturing Stainless Steel Alloy (UNS S31603) with Powder Bed Fusion
America Makes	Standardization Roadmap for Additive Manufacturing VERSION 2.0	

America Makes is the leading AM industry standards collaboration organization in the United States; in 2016, America Makes and the American National Standards Institute (ANSI) launched a collaborative effort to coordinate development of standards and address technical difficulties. Version 2.0 of the America Makes “Standardization Roadmap for Additive Manufacturing” was published in 2018 and includes an extensive gap analysis of AM codes and standards incorporating perspectives as diverse as the US Food and Drug Administration, US Department of Defense, NASA, Society of Automotive Engineers (SAE International), Institute of Electrical and Electronics Engineers (IEEE), Underwriters Laboratories, Ford Motor Company, GE Additive, Boeing, Caterpillar, DuPont, and Honeywell, to name a few. In addition to measurement, machine calibration, machine qualification, and material properties, the document’s gap analysis includes topics such as cybersecurity and anti-counterfeiting measures and identifies standards currently under draft. “Standardization Roadmap for Additive Manufacturing” is a recommended reference for its thorough analysis, action plan recommendations, and breadth of industry participation.

The remaining five documents are published by three organizations and address two topics: process qualification and material property certification. ASTM 52904 and F3184 are informative only to the extent of listing relevant ASTM and ISO standards (e.g., ASTM E8) and partially listing documentation requirements. Some details are specified, such as permissible chemical composition ranges; however, many technical details are left to purchaser/supplier contract specifications. Contract specifications are

presumed to include criteria for contaminated powder, part inspection criteria, and frequency of used powder sampling and testing. Furthermore, critical acceptance criteria for homogeneous vs. heterogeneous microstructures, transversely isotropic vs. isotropic behavior, and acceptable porosity measurement methods are not provided in these standards. Witness specimens are also not discussed in either standard, nor are procedures to evaluate the effects of planned and unplanned build interruptions (e.g., electrical power outages).

AWS D20.1M addresses numerous shortcomings of ASTM 52904, such as preproduction build layouts with thick- and thin-walled specimens in multiple orientations (see Section 3.3.3.1.1 for relevance); quantity, size, and positioning of witness specimens; procedures for planned and unplanned build interruptions; and the percentage of production builds that must be radiographically examined. All three standards organizations (i.e., AWS, ASTM, and ISO) define various classes of end-use component qualifications; The AWS and NASA standards define classes based upon the criticality of a component and a failure modes and effects analysis, whereas ASTM defines classes solely based on heat treatments. The intent of the AWS and NASA standards in requiring varying levels of qualification and reporting based upon the component's failure modes and effects analysis is to facilitate manufacturer burdens to levels commensurate with the criticality of a component.

MSFC-SPEC-3717 and MSFC-STD-3716, both published by NASA, provide three significant contributions not found in AWS D20.1M: statistically sound testing requirements, procedures for setting design property values, and best practice guidance. MSFC-STD-3716 specifies test specimen quantity requirements to address powder lot variability, orientation variability, geometry variability, and surface finish variability with sufficient residual degrees of freedom for statistical significance. Each source of variability may then be quantified using analysis of variance or similarly appropriate method, and design values be determined based on quantified variability. This method is in direct contrast to ASTM, which has assigned static minimum property requirements and therefore design values. By determining design values based on empirical evidence and allowing for different design values to be used based on LPBF machine, powder vendor, and scan strategies, MSFC-STD-3716 facilitates the development and incorporation of improved hardware, feedstock, and scan strategies without requiring continual revision of codes and regulations. Finally, both NASA documents include significant best practice commentary, which may be applicable to the development of codes and standards for LPBF components in NPP applications.

One explicit contradiction in codes was found; AWS D20.1M explicitly recommends not using powder reuse cycles as a metric for rejecting recycled powder, whereas MSFC-SPEC-3717 and MSFC-STD-3716 suggest using the number of reuse cycles as a metric if the number of reuse cycles has a quantitatively adverse effect on performance.

Recommendations for Use of Relevant Codes and Standards in NPP Applications

Because of the shortcomings identified above, the authors recommend that ISO/ASTM 52904:2019 and ASTM F3184 - 16 not be used in developing codes and standards for LPBF components in NPP applications or referenced as guiding documents. AWS D20.1M, MSFC-STD-3717, and MSFC-STD-3716 provide a more sound basis for machine, process, and component inspection qualification procedures. The statistical methodology outlined in MSFC-STD-3716 is recommended both for quantifying sources of variability as well as determining design values. Contrary to AWS D20.1M requirements, however, the authors recommend that test specimens initially be sectioned from replicates of the end-use component after all post-processing when possible rather than cylinders or rectangular bars. Simplified geometries may not be representative of the microstructures found in complex shapes such as thin-walled heat exchangers or debris filters, and the material properties of the end-use component may therefore vary significantly from the simplified geometry. As discussed previously in Section

3.3.3.1.1, the potential for systematic differences in the porosity in the skin and interior region of the components can create greater issues in very thin sections than thicker sections. If sufficient empirical evidence is presented on an alloy-specific basis to demonstrate equivalence or generalized correlations between the material properties of end-use components and witness coupons, then the recommendation to section and test end-use components may be relaxed. HIPing and/or scan strategy refinement may help address the microstructural and porosity concerns and facilitate the use of simplified test specimen geometry as discussed earlier in greater detail in Section 3.3.2. Gap Analysis

AWS D20.1M, MSFC-STD-3717, and MSFC-STD-3716 provide suitable standards and procedures for most aspects of feedstock, machine, process, and NDE qualification; however, four topics have been identified as insufficiently addressed in scientific literature and within current codes and standards. Topics were identified via scientific literature indicating a need for further research, a lack of scientific literature on some topics, and a lack of codes and standards specifically addressing some topics. Topics were ranked according to the breadth of their influence. For example, topic 1—microstructural heterogeneity—may affect all LPBF components irrespective of whether a component is welded, irradiated, or exposed to corrosive environments. Conversely, topic 3—technical understanding of LPBF microstructure and pre- and post-welding in the context of light water reactors—is only pertinent to welded components. All topics are ranked and discussed in Table 2121.

The topic ranked #1 (i.e., most important) addresses technical difficulties with accurately measuring material property heterogeneity, which is not covered in existing codes and standards. Topics ranked 2a and 2b are identified knowledge gaps on the long-term interactions of the LPBF microstructure and feedstock composition with irradiation response and corrosion rates. Ranked topic 3 has been identified because no standards currently exist on said topic.

Table 21. Critical gaps in codes and standards related to LPBF 316L in NPP applications.

Rank		
1	Microstructural heterogeneity	
	Codes and standards	MSFC-STD-3716 section 5.4.2.4
	Discussion	The risk of heterogeneity lies in incorrectly assuming homogeneity or incorrectly estimating the average property as a function of location. Section 5.4.2.4 of MSFC-STD-3716 specifies that components must be evaluated to determine whether a component is heterogeneous and the effect of the heterogeneity on material properties but does not specify the form of such an evaluation. From a codes and standards perspective, a quantifiable definition of heterogeneity and statistically driven requirements for the locations of specimens, the orientation of specimens, the number of specimens per component, and the number of replicate components are needed to quantify the effects of heterogeneity. Such testing requirements may not be static but instead scale with the number of regions suspected of having varying microstructures. It is unclear at this time whether such test specimens, sourced from the final end-use geometry, need be mechanical test specimens or Bakelite-mounted metallographic specimens. Heterogeneous microstructures are not necessarily detrimental. Heterogeneity may be strategically used to improve specific material properties in the locations needed. For example, by deliberately increasing the average grain size in a specific region of a component, the ductility of said region will be improved. Alternatively, heterogeneity may be used to produce comparatively inferior material properties in specific locations to concentrate crack propagation within those specific locations with the intent that with both inspections and cracks being concentrated in specific regions, a higher percentage of all cracks are detected and components replaced promptly. Crack concentration via geometry

		has long been technically feasible; controlled heterogeneity via the LPBF process may offer similar opportunities with microstructures.
2	Technical understanding of effects of elemental composition and powder reuse cycles in context of light water reactors	
	Codes and standards	MSFC-STD-3716 section 5.4.2.2 MSFC-STD-3717 section 4.1.2.2 AWS D20.1/D20.1M appendix C.5.4.2 ASTM F3184-16 section 7
	Discussion	Powder degradation due to powder recycling and reuse is a known phenomenon, which can significantly impact final component performance; however, the economics of LPBF heavily rely on powder reuse to be cost effective. AWS D20.1/D20.1M appendix C.5.4.2 specifies tracking several quantitative powder characteristics such as size distribution, chemical composition, and flowability; additional quantitative criteria may be added as appropriate to the alloy and / or component application. Acceptance or rejection of recycled powder is then based upon said characteristics. MSFC-STD-3716 section 5.4.2.2 and MSFC-STD-3717 section 4.1.2.2 specify that quantitative powder metrics correlating to component performance be identified, quantified, and tracked, but do not specify metrics as alloy specific standards are needed. All three standards clearly state that additional powder criteria unique to the alloy may be added as appropriate. Silicon oxide has been identified in both feedstock 316L and fabricated components and has been documented as detrimentally affecting SCC crack growth rates. The authors recommend that silicon oxide content be included as an additional criterion for powder acceptance/rejection in both virgin and recycled feedstock. It is unclear at this time whether such a specification should take the form of weight percent, oxide particle size, counts per volume, or a combination of such metrics. Future efforts to develop a low–silicon oxide variation of 316L specifically for LPBF may result in other oxides being preferentially formed (e.g., manganese oxide) with similarly adverse effects; therefore, additional oxides may need to be included in feedstock metrics. In addition to silicon oxide content standards, studies are needed to identify whether the 316L chemical composition ranges specified in ASTM F3184-16 are acceptable for light water reactor applications. Specific items for investigation include as-fabricated phases, oxides other than silicon oxide, and dendritic microstructures.
3	Technical understanding of LPBF weld microstructure and pre- and post-welding heat treatments in the context of light water reactors	
	Codes and standards	No standards
	Discussion	As discussed in Section 3.3.5**Error! Reference source not found.**, weld shape, penetration, and phases in LPBF 316L differ from conventional 316L. Existing literature suggests that uniform low-porosity welds are achievable in LPBF 316L with careful welding parameter selection; however, the microstructure of LPBF 316L welds has not been well characterized. In particular, the weld phase(s) and potential elemental segregation have not been quantified. To the authors' knowledge, only as-fabricated LPBF 316L welds have been reported to date; therefore, a knowledge gap also exists with respect to heat treatments prior to and post welding. The authors recommend that the LPBF 316L weld microstructure and effect of pre- and post-welding heat treatments be investigated before forming applicable codes and standards.

CONCLUSIONS

Conventional subtractive manufacturing starts with an ingot of homogeneous and isotropic material and shapes it into the desired object with constraints on tooling paths and lines of sight. LPBF sequentially melts layers of metal powder into the desired shape with constraints on overhangs and unsupported features. QC in conventional manufacturing primarily revolves around testing statistically significant quantities of specimens sourced from the same ingot as a component with the reasonable assumption that the material properties are indistinguishable. The technical challenge in conventional manufacturing is typically removing material and geometric accuracy. In LPBF the primary QC concern is quantifying and controlling variability in the fabricated component's microstructure and therefore material properties. While progress has been made in demonstrating repeatable manufacturing processes and codifying requirements in standards, several technical and codes and standards gaps should be addressed prior to the use of LPBF components in NPP applications. Major technical gaps include software and file control, sampling methodologies for determining material properties, procedures for planned and unplanned build interruptions, understanding geometry-scan strategy interactions, and minimizing feedstock contamination. Major gaps in codes and standards include definitions and procedures to quantify microstructural heterogeneity, acceptable chemical composition ranges, and pre and post-welding heat treatment requirements. Each identified gap has the potential to adversely affect material properties in a probabilistic manner if not addressed. Fabricating components for NPP applications with LPBF will require the above gaps to be addressed, but offers significant advantages relative to conventional manufacturing such as reduced lead times, reduced component inventory, potentially superior material properties, improved geometries, simplified assemblies, and the ability to reproduce nearly any "obsolete" component from vendors that have gone out of business.

REFERENCES

[1] T. Zacharia, Statement of Thomas Zacharia Director , Oak Ridge National Laboratory Hearing on the Future of Nuclear Power : Advanced Reactors, (2019) 1–9.

[2] A. Schwarber, Congress and DOE Look to Spur New Nuclear Reactor Designs, Am. Inst. Phys. (n.d.). https://www.aip.org/fyi/2019/congress-and-doe-look-spur-new-nuclear-reactor-designs.

[3] Nuclear Energy Institute, Addressing the Challenges with Establishing the Infrastructure for the front- end of the Fuel Cycle for Advanced Reactors, (2018). https://images.magnetmail.net/images/clients/NEI_/attach/NEI-WhitePaper_FrontEndFuelCycle_Jan-2018.pdf.

[4] Nuclear Energy Institute, Roadmap for Regulatory Acceptance of Advanced Manufacturing Methods in the Nuclear Energy Industry, (2019).

[5] Boeing 787, (n.d.). https://www.reuters.com/article/us-norsk-boeing-idUSKBN17C264 (accessed March 18, 2019).

[6] Boeing SES-15, (n.d.). https://www.boeing.com/features/innovation-quarterly/nov2017/feature-thought-leadership-3d-printing.page (accessed March 18, 2019).

[7] GE Fuel Nozzel, (n.d.). https://www.ge.com/reports/epiphany-disruption-ge-additive-chief-explains-3d-printing-will-upend-manufacturing/ (accessed March 18, 2019).

[8] D. Herzog, V. Seyda, E. Wycisk, C. Emmelmann, Additive manufacturing of metals, Acta Mater. 117 (2016) 371–392. https://doi.org/10.1016/j.actamat.2016.07.019.

[9] W.E. Frazier, Metal additive manufacturing: A review, J. Mater. Eng. Perform. 23 (2014) 1917–1928. https://doi.org/10.1007/s11665-014-0958-z.

[10] D.I. Wimpenny, P.M. Pandey, L.J. Kumar, eds., Advances in 3D Printing and Additive Manufacturing Technologies, Springer US, 2017.

[11] G. Allaire, C. Dapogny, R. Estevez, A. Faure, G. Michailidis, Structural optimization under overhang constraints imposed by additive manufacturing technologies, J. Comput. Phys. 351 (2017) 295–328. https://doi.org/10.1016/j.jcp.2017.09.041.

[12] Y. Zhang, L. Wu, X. Guo, S. Kane, Y. Deng, Y.G. Jung, J.H. Lee, J. Zhang, Additive Manufacturing of Metallic Materials: A Review, J. Mater. Eng. Perform. 27 (2018) 1–13. https://doi.org/10.1007/s11665-017-2747-y.

[13] L. Cordova, M. Campos, T. Tinga, Revealing the Effects of Powder Reuse for Selective Laser Melting by Powder Characterization, Jom. 71 (2019) 1062–1072. https://doi.org/10.1007/s11837-018-3305-2.

[14] O.A. Quintana, J. Alvarez, R. Mcmillan, W. Tong, C. Tomonto, Effects of Reusing Ti-6Al-4V Powder in a Selective Laser Melting Additive System Operated in an Industrial Setting, Jom. 70 (2018) 1863–1869. https://doi.org/10.1007/s11837-018-3011-0.

[15] S.K. Kennedy, A.M. Dalley, G.J. Kotyk, Additive Manufacturing: Assessing Metal Powder Quality Through Characterizing Feedstock and Contaminants, J. Mater. Eng. Perform. 28 (2019) 728–740. https://doi.org/10.1007/s11665-018-3841-5.

[16] A. Santomaso, P. Lazzaro, P. Canu, Powder flowability and density ratios: The impact of granules packing, Chem. Eng. Sci. 58 (2003) 2857–2874. https://doi.org/10.1016/S0009-2509(03)00137-4.

[17] A.T. Sutton, C.S. Kriewall, M.C. Leu, J.W. Newkirk, Powder characterisation techniques and effects of powder characteristics on part properties in powder-bed fusion processes, Virtual Phys. Prototyp. 12 (2016) 3–29. https://doi.org/10.1080/17452759.2016.1250605.

[18] W.J. Sames, F.A. List, S. Pannala, R.R. Dehoff, S.S. Babu, The metallurgy and processing science of metal additive manufacturing, Int. Mater. Rev. 61 (2016) 315–360.

https://doi.org/10.1080/09506608.2015.1116649.

[19] J. Lei, J. Xie, S. Zhou, H. Song, X. Song, X. Zhou, Comparative study on microstructure and corrosion performance of 316 stainless steel prepared by laser melting deposition with ring-shaped beam and Gaussian beam, Opt. Laser Technol. 111 (2019) 271–283. https://doi.org/10.1016/j.optlastec.2018.09.057.

[20] A. Klassen, T. Scharowsky, C. Körner, Evaporation model for beam based additive manufacturing using free surface lattice Boltzmann methods, J. Phys. D. Appl. Phys. 47 (2014). https://doi.org/10.1088/0022-3727/47/27/275303.

[21] A. Klassen, V.E. Forster, C. Körner, A multi-component evaporation model for beam melting processes, Model. Simul. Mater. Sci. Eng. 25 (2017). https://doi.org/10.1088/1361-651X/aa5289.

[22] H.P. Tang, M. Qian, N. Liu, X.Z. Zhang, G.Y. Yang, J. Wang, Effect of Powder Reuse Times on Additive Manufacturing of Ti-6Al-4V by Selective Electron Beam Melting, Jom. 67 (2015) 555–563. https://doi.org/10.1007/s11837-015-1300-4.

[23] G. Jacob, C. Brown, A. Donmez, S. Watson, J. Slotwinski, Effects of powder recycling on stainless steel powder and built material properties in metal powder bed fusion processes, NIST Adv. Manuf. Ser. 100–6 (2017). https://doi.org/10.6028/NIST.AMS.100-6.

[24] M.J. Heiden, L.A. Deibler, J.M. Rodelas, J.R. Koepke, D.J. Tung, D.J. Saiz, B.H. Jared, Evolution of 316L stainless steel feedstock due to laser powder bed fusion process, Addit. Manuf. 25 (2019) 84–103. https://doi.org/10.1016/j.addma.2018.10.019.

[25] W.J. Sames, F. Medina, W.H. Peter, S.S. Babu, R.R. Dehoff, Effect of Process Control and Powder Quality on Inconel 718 Produced Using Electron Beam Melting, 8th Int. Symp. Superalloy 718 Deriv. (2014) 409–423. https://doi.org/10.1002/9781119016854.ch32.

[26] H. Qi, M. Azer, A. Ritter, Studies of standard heat treatment effects on microstructure and mechanical properties of laser net shape manufactured INCONEL 718, Metall. Mater. Trans. A Phys. Metall. Mater. Sci. 40A (2009) 2410–2422. https://doi.org/10.1007/s11661-009-9949-3.

[27] X. Zhao, J. Chen, X. Lin, W. Huang, Study on microstructure and mechanical properties of laser rapid forming Inconel 718, Mater. Sci. Eng. A. 478 (2008) 119–124. https://doi.org/10.1016/j.msea.2007.05.079.

[28] F. Medina, Reducing Metal Alloy Powder Costs for Use in Powder Bed Fusion Additive Manufacturing: Improving the Economics for Production, University of Texas at El Paso, 2013.

[29] P.A. Kobryn, E.H. Moore, S.L. Semiatin, Effect of laser power and traverse speed on microstructure, porosity, and build height in laser-deposited Ti-6Al-4V, Scr. Mater. 43 (2000) 299–305. https://doi.org/10.1016/S1359-6462(00)00408-5.

[30] J. Robinson, I. Ashton, P. Fox, E. Jones, C. Sutcliffe, Determination of the effect of scan strategy on residual stress in laser powder bed fusion additive manufacturing, Addit. Manuf. 23 (2018) 13–24. https://doi.org/10.1016/j.addma.2018.07.001.

[31] L. N. Carter, M. M. Attallah, R. C. Reed, Laser powder bed fabrication of nickel-base superalloys: influence of parameters; characterisation, quantification and mitigation of cracking, in: Superalloys 2012 12th Int. Symp. Superalloys, 2012: pp. 577--586.

[32] A.F.H. Kaplan, J. Powell, Spatter in laser welding, J. Laser Appl. 23 (2011) 032005. https://doi.org/10.2351/1.3597830.

[33] E.C. Santos, M. Shiomi, K. Osakada, T. Laoui, Rapid manufacturing of metal components by laser forming, Int. J. Mach. Tools Manuf. 46 (2006) 1459–1468. https://doi.org/10.1016/j.ijmachtools.2005.09.005.

[34] K.A. Mumtaz, N. Hopkinson, Selective Laser Melting of thin wall parts using pulse shaping, J. Mater. Process. Technol. 210 (2010) 279–287. https://doi.org/10.1016/j.jmatprotec.2009.09.011.

[35] M.J. Matthews, G. Guss, S.A. Khairallah, A.M. Rubenchik, P.J. Depond, W.E. King, Denudation

of metal powder layers in laser powder bed fusion processes, Acta Mater. 114 (2016) 33–42. https://doi.org/10.1016/j.actamat.2016.05.017.

[36] S.A. Khairallah, A.T. Anderson, A. Rubenchik, W.E. King, Laser powder-bed fusion additive manufacturing: physics of complex melt flow and formation mechanisms of pores, spatter, and denudation zones Saad, Acta Mater. 108 (2016) 36–45. https://doi.org/10.3139/9783446461338.003.

[37] H. Chen, W. Yan, Spattering and denudation in laser powder bed fusion process: Multiphase flow modelling, Acta Mater. 196 (2020) 154–167. https://doi.org/10.1016/j.actamat.2020.06.033.

[38] GE Unveils First Beta Machine from Project ATLAS Program, (2017) https://www.additivemanufacturing.media/products/g.

[39] A. Hussein, L. Hao, C. Yan, R. Everson, P. Young, Advanced lattice support structures for metal additive manufacturing, J. Mater. Process. Technol. 213 (2013) 1019–1026. https://doi.org/10.1016/j.jmatprotec.2013.01.020.

[40] J. Cao, F. Liu, X. Lin, C. Huang, J. Chen, W. Huang, Effect of overlap rate on recrystallization behaviors of Laser Solid Formed Inconel 718 superalloy, Opt. Laser Technol. 45 (2013) 228–235. https://doi.org/10.1016/j.optlastec.2012.06.043.

[41] B. Song, S. Dong, Q. Liu, H. Liao, C. Coddet, Vacuum heat treatment of iron parts produced by selective laser melting: Microstructure, residual stress and tensile behavior, Mater. Des. 54 (2014) 727–733. https://doi.org/10.1016/j.matdes.2013.08.085.

[42] C. Körner, H. Helmer, A. Bauereiß, R.F. Singer, Tailoring the grain structure of IN718 during selective electron beam melting, MATEC Web Conf. 14 (2014). https://doi.org/10.1051/matecconf/20141408001.

[43] J.D. Hunt, Steady state columnar and equiaxed growth of dendrites and eutectic, Mater. Sci. Eng. 65 (1984) 75–83. https://doi.org/10.1016/0025-5416(84)90201-5.

[44] L. Nastac, J.J. Valencia, M.L. Tims, F.R. Dax, Advances in the Solidification of IN718 and RS5 Alloys, in: TMS, 2001: pp. 103–112. https://doi.org/10.7449/2001/superalloys_2001_103_112.

[45] Joy Gockel and Jack Beuth, Understanding Ti-6Al-4V Microstructure Control in Additive Manufacturing via Process Maps, in: 24th Int. SFF Symp. - An Addit. Manuf. Conf., 2013: pp. 666–674. https://doi.org/10.1007/s11837-005-0029-x.

[46] X. Wang, M. Jiang, Z. Zhou, J. Gou, D. Hui, 3D printing of polymer matrix composites: A review and prospective, Compos. Part B Eng. 110 (2017) 442–458. https://doi.org/10.1016/j.compositesb.2016.11.034.

[47] D. Dye, O. Hunziker, R.C. Reed, Numerical analysis of the weldability of superalloys, Acta Mater. 49 (2001) 683–697. https://doi.org/10.1016/S1359-6454(00)00361-X.

[48] G. Casalino, S.L. Campanelli, N. Contuzzi, A.D. Ludovico, Experimental investigation and statistical optimisation of the selective laser melting process of a maraging steel, Opt. Laser Technol. 65 (2015) 151–158. https://doi.org/10.1016/j.optlastec.2014.07.021.

[49] M.F. Zäh, S. Lutzmann, Modelling and simulation of electron beam melting, Prod. Eng. 4 (2010) 15–23. https://doi.org/10.1007/s11740-009-0197-6.

[50] A. V. Gusarov, I. Yadroitsev, P. Bertrand, I. Smurov, Heat transfer modelling and stability analysis of selective laser melting, Appl. Surf. Sci. 254 (2007) 975–979. https://doi.org/10.1016/j.apsusc.2007.08.074.

[51] M.F. Zaeh, M. Kahnert, The effect of scanning strategies on electron beam sintering, Prod. Eng. 3 (2009) 217–224. https://doi.org/10.1007/s11740-009-0157-1.

[52] M. Kahnert, S. Lutzmann, M.F. Zaeh, Layer formations in electron beam sintering, Proc. 18th Solid Free. Fabr. Symp. (2007) 88–99. https://doi.org/10.3386/w2977.

[53] T.D. McLouth, G.E. Bean, D.B. Witkin, S.D. Sitzman, P.M. Adams, D.N. Patel, W. Park, J.M. Yang, R.J. Zaldivar, The effect of laser focus shift on microstructural variation of Inconel 718 produced by selective laser melting, Mater. Des. 149 (2018) 205–213. https://doi.org/10.1016/j.matdes.2018.04.019.

[54] M. Tang, P.C. Pistorius, J.L. Beuth, Prediction of lack-of-fusion porosity for powder bed fusion, Addit. Manuf. 14 (2017) 39–48. https://doi.org/10.1016/j.addma.2016.12.001.

[55] A. Foroozmehr, M. Badrossamay, E. Foroozmehr, S. Golabi, Finite Element Simulation of Selective Laser Melting process considering Optical Penetration Depth of laser in powder bed, Mater. Des. 89 (2016) 255–263. https://doi.org/10.1016/j.matdes.2015.10.002.

[56] B. Cheng, L. Loeber, H. Willeck, U. Hartel, C. Tuffile, Computational Investigation of Melt Pool Process Dynamics and Pore Formation in Laser Powder Bed Fusion, J. Mater. Eng. Perform. 28 (2019) 6565–6578. https://doi.org/10.1007/s11665-019-04435-y.

[57] H. KYOGOKU, T.-T. IKESHOJI, A review of metal additive manufacturing technologies: Mechanism of defects formation and simulation of melting and solidification phenomena in laser powder bed fusion process, Mech. Eng. Rev. 7 (2020) 19-00182-19–00182. https://doi.org/10.1299/mer.19-00182.

[58] H. Gu, C. Wei, L. Li, Q. Han, R. Setchi, M. Ryan, Q. Li, Multi-physics modelling of molten pool development and track formation in multi-track, multi-layer and multi-material selective laser melting, Int. J. Heat Mass Transf. 151 (2020) 119458. https://doi.org/10.1016/j.ijheatmasstransfer.2020.119458.

[59] M. Bayat, A. Thanki, S. Mohanty, A. Witvrouw, S. Yang, J. Thorborg, N.S. Tiedje, J.H. Hattel, Keyhole-induced porosities in Laser-based Powder Bed Fusion (L-PBF) of Ti6Al4V: High-fidelity modelling and experimental validation, Addit. Manuf. 30 (2019) 100835. https://doi.org/10.1016/j.addma.2019.100835.

[60] Y. Geng, N. Harrison, Functionally graded bimodal Ti6Al4V fabricated by powder bed fusion additive manufacturing: Crystal plasticity finite element modelling, Mater. Sci. Eng. A. 773 (2020) 138736. https://doi.org/10.1016/j.msea.2019.138736.

[61] A. Jammal, G. Wang, Z. JiaXin, H. Yang, S. Yang, Y. Zhong, Y. Rong, Multi-scale modelling of solidification and microstructure evolution in laser-deposition of T15 high speed steel, J. Manuf. Process. 50 (2020) 24–33. https://doi.org/10.1016/j.jmapro.2019.12.024.

[62] M. Letenneur, A. Kreitcberg, V. Brailovski, Optimization of Laser Powder Bed Fusion Processing Using a Combination of Melt Pool Modeling and Design of Experiment Approaches: Density Control, J. Manuf. Mater. Process. 3 (2019) 21. https://doi.org/10.3390/jmmp3010021.

[63] X. Gong, T. Anderson, K. Chou, Review on Powder-Based Electron Beam Additive Manufacturing Technology, in: ASME/ISCIE 2012 Int. Symp. Flex. Autom., 2012. https://doi.org/10.1115/ISFA2012-7256.

[64] P.L. Blackwell, The mechanical and microstructural characteristics of laser-deposited IN718, J. Mater. Process. Technol. 170 (2005) 240–246. https://doi.org/10.1016/j.jmatprotec.2005.05.005.

[65] M. Seifi, A.A. Salem, D.P. Satko, R. Grylls, J.J. Lewandowski, Effects of Post-processing on Microstructure and Mechanical Properties of SLM-Processed IN-718, in: E. Ott, X. Liu, J. Andersson, Z. Bi, K. Bockenstedt, I. Dempster, J. Groh, K. Heck, P. Jablonski, M. Kaplan, D. Nagahama, C. Sudbrack (Eds.), Proc. 9th Int. Symp. Superalloy 718 Deriv. Energy, Aerospace, Ind. Appl., Springer International Publishing, Cham, 2018: pp. 515–526.

[66] S. Goel, J. Olsson, M. Ahlfors, U. Klement, S. Joshi, The Effect of Location and Post-treatment on the Microstructure of EBM-Built Alloy 718, in: E. Ott, X. Liu, J. Andersson, Z. Bi, K. Bockenstedt, I. Dempster, J. Groh, K. Heck, P. Jablonski, M. Kaplan, D. Nagahama, C. Sudbrack (Eds.), Proc. 9th Int. Symp. Superalloy 718 Deriv. Energy, Aerospace, Ind. Appl., Springer International Publishing, Cham, 2018: pp. 115–129.

[67] B. Shassere, D. Greeley, A. Okello, M. Kirka, P. Nandwana, R. Dehoff, Correlation of Microstructure to Creep Response of Hot Isostatically Pressed and Aged Electron Beam Melted Inconel 718, Metall. Mater. Trans. A Phys. Metall. Mater. Sci. 49A (2018) 5107–5117. https://doi.org/10.1007/s11661-018-4812-z.

[68] A.R. Balachandramurthi, J. Moverare, S. Mahade, R. Pederson, Additive manufacturing of alloy 718 via electron beam melting: Effect of post-treatment on the microstructure and the mechanical properties, Materials (Basel). 12 (2018). https://doi.org/10.3390/ma12010068.

[69] G. Marchese, E. Bassini, A. Aversa, M. Lombardi, D. Ugues, P. Fino, S. Biamino, Microstructural Evolution of Post-Processed Hastelloy X Alloy Fabricated by Laser Powder Bed Fusion, Materials (Basel). 12 (2019) 486. https://doi.org/10.3390/ma12030486.

[70] K. Moussaoui, W. Rubio, M. Mousseigne, T. Sultan, F. Rezai, Effects of Selective Laser Melting additive manufacturing parameters of Inconel 718 on porosity, microstructure and mechanical properties, Mater. Sci. Eng. A. 735 (2018) 182–190. https://doi.org/10.1016/j.msea.2018.08.037.

[71] E. Sadeghi, P. Karimi, S. Momeni, M. Seifi, A. Eklund, J. Andersson, Influence of thermal post treatments on microstructure and oxidation behavior of EB-PBF manufactured Alloy 718, Mater. Charact. 150 (2019) 236–251. https://doi.org/10.1016/j.matchar.2019.02.016.

[72] V.A. Popovich, E. V. Borisov, A.A. Popovich, V.S. Sufiiarov, D. V. Masaylo, L. Alzina, Impact of heat treatment on mechanical behaviour of Inconel 718 processed with tailored microstructure by selective laser melting, Mater. Des. 131 (2017) 12–22. https://doi.org/10.1016/j.matdes.2017.05.065.

[73] A. Mostafa, I. Picazo Rubio, V. Brailovski, M. Jahazi, M. Medraj, Structure, Texture and Phases in 3D Printed IN718 Alloy Subjected to Homogenization and HIP Treatments, Metals (Basel). 7 (2017). https://doi.org/10.3390/met7080315.

[74] B. Ruttert, M. Ramsperger, L. Mujica Roncery, I. Lopez-Galilea, C. Körner, W. Theisen, Impact of hot isostatic pressing on microstructures of CMSX-4 Ni-base superalloy fabricated by selective electron beam melting, Mater. Des. 110 (2016) 720–727. https://doi.org/10.1016/j.matdes.2016.08.041.

[75] S. Goel, M. Ahlfors, F. Bahbou, S. Joshi, Effect of Different Post-treatments on the Microstructure of EBM-Built Alloy 718, J. Mater. Eng. Perform. 28 (2019) 673–680. https://doi.org/10.1007/s11665-018-3712-0.

[76] R. Wauthle, B. Vrancken, B. Beynaerts, K. Jorissen, J. Schrooten, J.P. Kruth, J. Van Humbeeck, Effects of build orientation and heat treatment on the microstructure and mechanical properties of selective laser melted Ti6Al4V lattice structures, Addit. Manuf. 5 (2015) 77–84. https://doi.org/10.1016/j.addma.2014.12.008.

[77] S.L. Lu, H.P. Tang, Y.P. Ning, N. Liu, D.H. StJohn, M. Qian, Microstructure and Mechanical Properties of Long Ti-6Al-4V Rods Additively Manufactured by Selective Electron Beam Melting Out of a Deep Powder Bed and the Effect of Subsequent Hot Isostatic Pressing, Metall. Mater. Trans. A Phys. Metall. Mater. Sci. 46A (2015) 3824–3834. https://doi.org/10.1007/s11661-015-2976-3.

[78] N. Perevoshchikova, C.R. Hutchinson, X. Wu, The design of hot-isostatic pressing schemes for Ti-5Al-5Mo-5V-3Cr (Ti-5553), Mater. Sci. Eng. A. 657 (2016) 371–382. https://doi.org/10.1016/j.msea.2016.01.082.

[79] A.B. Spierings, K. Dawson, K. Kern, F. Palm, K. Wegener, SLM-processed Sc- and Zr- modified Al-Mg alloy: Mechanical properties and microstructural effects of heat treatment, Mater. Sci. Eng. A. 701 (2017) 264–273. https://doi.org/10.1016/j.msea.2017.06.089.

[80] Y. Zhai, B. Huang, X. Mao, M. Zheng, Effect of hot isostatic pressing on microstructure and mechanical properties of CLAM steel produced by selective laser melting, J. Nucl. Mater. 515 (2019) 111–121. https://doi.org/10.1016/j.jnucmat.2018.12.028.

[81] M. Åsberg, G. Fredriksson, S. Hatami, W. Fredriksson, P. Krakhmalev, Influence of post treatment on microstructure, porosity and mechanical properties of additive manufactured H13 tool steel, Mater. Sci. Eng. A. 742 (2019) 584–589. https://doi.org/10.1016/j.msea.2018.08.046.

[82] M. M, R. J, F. D, Handbook of laser materials processing, Magnolia Publishing Inc, Orlando, USA, 2001.

[83] T.D. Ngo, A. Kashani, G. Imbalzano, K.T.Q. Nguyen, D. Hui, Additive manufacturing (3D printing): A review of materials, methods, applications and challenges, Compos. Part B Eng. 143 (2018) 172–196. https://doi.org/10.1016/j.compositesb.2018.02.012.

[84] D.D. Gu, W. Meiners, K. Wissenbach, R. Poprawe, Laser additive manufacturing of ceramic components: Materials, processes, and mechanisms, Int. Mater. Rev. 57 (2012) 133–164. https://doi.org/10.1016/B978-0-08-100433-3.00006-3.

[85] Y. Hu, F. Ning, X. Wang, H. Wang, B. Zhao, W. Cong, Y. Li, Laser deposition-additive manufacturing of in situ TiB reinforced titanium matrix composites: TiB growth and part performance, Int. J. Adv. Manuf. Technol. 93 (2017) 3409–3418. https://doi.org/10.1007/s00170-017-0769-0.

[86] J. Vaithilingam, S. Kilsby, R.D. Goodridge, S.D.R. Christie, S. Edmondson, R.J.M. Hague, Functionalisation of Ti6Al4V components fabricated using selective laser melting with a bioactive compound, Mater. Sci. Eng. C. 46 (2015) 52–61. https://doi.org/10.1016/j.msec.2014.10.015.

[87] H. Attar, M. Calin, L.C. Zhang, S. Scudino, J. Eckert, Manufacture by selective laser melting and mechanical behavior of commercially pure titanium, Mater. Sci. Eng. A. 593 (2014) 170–177. https://doi.org/10.1016/j.msea.2013.11.038.

[88] I. Yadroitsev, L. Thivillon, P. Bertrand, I. Smurov, Strategy of manufacturing components with designed internal structure by selective laser melting of metallic powder, Appl. Surf. Sci. 254 (2007) 980–983. https://doi.org/10.1016/j.apsusc.2007.08.046.

[89] I. Rosenthal, A. Stern, N. Frage, Strain rate sensitivity and fracture mechanism of AlSi10Mg parts produced by Selective Laser Melting, Mater. Sci. Eng. A. 682 (2017) 509–517. https://doi.org/10.1016/j.msea.2016.11.070.

[90] P. Vora, K. Mumtaz, I. Todd, N. Hopkinson, AlSi12 in-situ alloy formation and residual stress reduction using anchorless selective laser melting, Addit. Manuf. 7 (2015) 12–19. https://doi.org/10.1016/j.addma.2015.06.003.

[91] H.D. Carlton, A. Haboub, G.F. Gallegos, D.Y. Parkinson, A.A. MacDowell, Damage evolution and failure mechanisms in additively manufactured stainless steel, Mater. Sci. Eng. A. 651 (2016) 406–414. https://doi.org/10.1016/j.msea.2015.10.073.

[92] J. Mazumder, J. Choi, K. Nagarathnam, J. Koch, D. Hetzner, The Direct Metal Deposition of H13 Tool Steel for 3-D Components, JOM. 49 (1997) 55–60. https://link.springer.com/content/pdf/10.1007%2FBF02914687.pdf.

[93] L.E. Murr, E. Martinez, J. Hernandez, S. Collins, K.N. Amato, S.M. Gaytan, P.W. Shindo, Microstructures and properties of 17-4 PH stainless steel fabricated by selective laser melting, J. Mater. Res. Technol. 1 (2012) 167–177. https://doi.org/10.1016/S2238-7854(12)70029-7.

[94] J.S. Zuback, T. DebRoy, The Hardness of Additively Manufactured Alloys, Materials (Basel). 11 (2018) 2070. https://doi.org/10.3390/ma11112070.

[95] S. Magar, N.K. Khedkar, S. Kumar, Review of the effect of built orientation on mechanical Properties of metal-plastic composite parts fabricated by Additive Manufacturing Technique, Mater. Today Proc. 5 (2018) 3926–3935. https://doi.org/10.1016/j.matpr.2017.11.649.

[96] Y. Kok, X.P. Tan, P. Wang, M.L.S. Nai, N.H. Loh, E. Liu, S.B. Tor, Anisotropy and heterogeneity of microstructure and mechanical properties in metal additive manufacturing: A critical review, Mater. Des. 139 (2018) 565–586. https://doi.org/10.1016/j.matdes.2017.11.021.

[97] P. Edwards, M. Ramulu, Fatigue performance evaluation of selective laser melted Ti-6Al-4V, Mater. Sci. Eng. A. 598 (2014) 327–337. https://doi.org/10.1016/j.msea.2014.01.041.

[98] Z. Wang, K. Guan, M. Gao, X. Li, X. Chen, X. Zeng, The microstructure and mechanical properties of deposited-IN718 by selective laser melting, J. Alloys Compd. 513 (2012) 518–523. https://doi.org/10.1016/j.jallcom.2011.10.107.

[99] L.M. Sochalski-Kolbus, E.A. Payzant, P.A. Cornwell, T.R. Watkins, S.S. Babu, R.R. Dehoff, M. Lorenz, O. Ovchinnikova, C. Duty, Comparison of Residual Stresses in Inconel 718 Simple Parts Made by Electron Beam Melting and Direct Laser Metal Sintering, Metall. Mater. Trans. A Phys. Metall. Mater. Sci. 46A (2015) 1419–1432. https://doi.org/10.1007/s11661-014-2722-2.

[100] K.N. Amato, S.M. Gaytan, L.E.E. Murr, E. Martinez, P.W. Shindo, J. Hernandez, S. Collins, F. Medina, Microstructures and mechanical behavior of Inconel 718 fabricated by selective laser melting, Acta Mater. 60 (2012) 2229–2239. https://doi.org/10.1016/j.actamat.2011.12.032.

[101] R.R. Dehoff, M.M. Kirka, W.J. Sames, H. Bilheux, A.S. Tremsin, L.E. Lowe, S.S. Babu, Site specific control of crystallographic grain orientation through electron beam additive manufacturing, Mater. Sci. Technol. 31 (2015) 931–938. https://doi.org/10.1179/1743284714y.0000000734.

[102] S. Liu, Y.C. Shin, Additive manufacturing of Ti6Al4V alloy: A review, Mater. Des. 164 (2019) 107552. https://doi.org/10.1016/j.matdes.2018.107552.

[103] J.J. Lewandowski, M. Seifi, Metal Additive Manufacturing: A Review of Mechanical Properties, Annu. Rev. Mater. Res. 46 (2016) 151–186. https://doi.org/10.1146/annurev-matsci-070115-032024.

[104] Q. Liu, Y. Wang, H. Zheng, K. Tang, L. Ding, H. Li, S. Gong, Microstructure and mechanical properties of LMD-SLM hybrid forming Ti6Al4V alloy, Mater. Sci. Eng. A. 660 (2016) 24–33. https://doi.org/10.1016/j.msea.2016.02.069.

[105] T.M. Mower, M.J. Long, Mechanical behavior of additive manufactured, powder-bed laser-fused materials, Mater. Sci. Eng. A. 651 (2016) 198–213. https://doi.org/10.1016/j.msea.2015.10.068.

[106] C. Qiu, N.J.E. Adkins, M.M. Attallah, Microstructure and tensile properties of selectively laser-melted and of HIPed laser-melted Ti-6Al-4V, Mater. Sci. Eng. A. 578 (2013) 230–239. https://doi.org/10.1016/j.msea.2013.04.099.

[107] H.K. Rafi, N.V. Karthik, T.L. Starr, B.E. Stucker, Mechanical property evaluation of Ti-6Al-4V parts made using Electron Beam Melting, 23rd Annu. Int. Solid Free. Fabr. Symp. - An Addit. Manuf. Conf. (2012) 526–535.

[108] N. Hrabe, T. Quinn, Effects of processing on microstructure and mechanical properties of a titanium alloy (Ti-6Al-4V) fabricated using electron beam melting (EBM), Part 2: Energy input, orientation, and location, Mater. Sci. Eng. A. 573 (2013) 271–277. https://doi.org/10.1016/j.msea.2013.02.065.

[109] H. Galarraga, D.A. Lados, R.R. Dehoff, M.M. Kirka, P. Nandwana, Effects of the microstructure and porosity on properties of Ti-6Al-4V ELI alloy fabricated by electron beam melting (EBM), Addit. Manuf. 10 (2016) 47–57. https://doi.org/10.1016/j.addma.2016.02.003.

[110] T. Vilaro, C. Colin, J.D. Bartout, As-fabricated and heat-treated microstructures of the Ti-6Al-4V alloy processed by selective laser melting, Metall. Mater. Trans. A Phys. Metall. Mater. Sci. 42A (2011) 3190–3199. https://doi.org/10.1007/s11661-011-0731-y.

[111] C. Romero, F. Yang, L. Bolzoni, Fatigue and fracture properties of Ti alloys from powder-based processes – A review, Int. J. Fatigue. 117 (2018) 407–419. https://doi.org/10.1016/j.ijfatigue.2018.08.029.

[112] S. Leuders, M. Thöne, A. Riemer, T. Niendorf, T. Tröster, H.A. Richard, H.J. Maier, On the mechanical behaviour of titanium alloy TiAl6V4 manufactured by selective laser melting: Fatigue

resistance and crack growth performance, Int. J. Fatigue. 48 (2013) 300–307. https://doi.org/10.1016/j.ijfatigue.2012.11.011.

[113] X. W, B. M, S. S, E. J, L. Q, L. K, X. K, Q. M, Additive manufacturing of strong and ductile Ti–6Al–4V by selective laser melting via in situ martensite decomposition, Acta Mater. 85 (2015) 74–84.

[114] D. MJ, D. SJ., Superalloys: a technical guide, ASM International, Materials Park (OH), 2002.

[115] T. DebRoy, H.L. Wei, J.S. Zuback, T. Mukherjee, J.W. Elmer, J.O. Milewski, A.M. Beese, A. Wilson-Heid, A. De, W. Zhang, Additive manufacturing of metallic components – Process, structure and properties, Prog. Mater. Sci. 92 (2018) 112–224. https://doi.org/10.1016/j.pmatsci.2017.10.001.

[116] Zuback JS, D. T., Unpublished research, (2017).

[117] B. V, K. P, P. V, K. S, G. K, S. R, A review on powder bed fusion technology of metal additive manufacturing, in: 4th Int. Conf. Exhib. Addit. Manuf. Technol., 2014: pp. 1–2.

[118] Z. Sun, X. Tan, S.B. Tor, W.Y. Yeong, Selective laser melting of stainless steel 316L with low porosity and high build rates, Mater. Des. 104 (2016) 197–204. https://doi.org/10.1016/j.matdes.2016.05.035.

[119] Z. Wang, T.A. Palmer, A.M. Beese, Effect of processing parameters on microstructure and tensile properties of austenitic stainless steel 304L made by directed energy deposition additive manufacturing, Acta Mater. 110 (2016) 226–235. https://doi.org/10.1016/j.actamat.2016.03.019.

[120] R.L. Plaut, C. Herrera, D.M. Escriba, P.R. Rios, A.F. Padilha, A Short review on wrought austenitic stainless steels at high temperatures: processing, microstructure, properties and performance, Mater. Res. 10 (2007) 453–460. https://doi.org/10.1590/S1516-14392007000400021.

[121] R.G. Thomas, D. Yapp, The Effect of Heat Treatment on Type 316 Stainless Steel Weld Metal, in: AWS 59th Annu. Meet., New Orleans, 1978: pp. 361–366.

[122] V.S. Raghunathan, V. Seetharaman, S. Venkadesan, P. Rodriguez, The influence of post weld heat treatments on the structure, composition and the amount of ferrite in type 316 stainless steel welds, Metall. Trans. A. 10A (1979) 1683–1689. https://doi.org/10.1007/BF02811701.

[123] A. Etienne, B. Radiguet, N.J. Cunningham, G.R. Odette, R. Valiev, P. Pareige, Comparison of radiation-induced segregation in ultrafine-grained and conventional 316 austenitic stainless steels, Ultramicroscopy. 111 (2011) 659–663. https://doi.org/10.1016/j.ultramic.2010.12.026.

[124] T.R. Smith, J.D. Sugar, J.M. Schoenung, C.S. Marchi, Anomalous Annealing Response of Directed Energy Deposited Type 304L Austenitic Stainless Steel, JOM. 70 (2018) 358–363.

[125] K. Saeidi, F. Akhtar, Subgrain-controlled grain growth in the laser-melted 316 L promoting strength at high temperatures, R. Soc. Open Sci. 5 (2018). https://doi.org/10.1098/rsos.172394.

[126] K. Zhang, S. Wang, W. Liu, X. Shang, Characterization of stainless steel parts by Laser Metal Deposition Shaping, Mater. Des. 55 (2014) 104–119. https://doi.org/10.1016/j.matdes.2013.09.006.

[127] M. Ziętala, T. Durejko, M. Polański, I. Kunce, T. Płociński, W. Zieliński, M. Łazińska, W. Stępniowski, T. Czujko, K.J. Kurzydłowski, Z. Bojar, The microstructure, mechanical properties and corrosion resistance of 316 L stainless steel fabricated using laser engineered net shaping, Mater. Sci. Eng. A. 677 (2016) 1–10. https://doi.org/10.1016/j.msea.2016.09.028.

[128] M. Ma, Z. Wang, D. Wang, X. Zeng, Control of shape and performance for direct laser fabrication of precision large-scale metal parts with 316L Stainless Steel, Opt. Laser Technol. 45 (2013) 209–216. https://doi.org/10.1016/j.optlastec.2012.07.002.

[129] I. Tolosa, F. Garciandía, F. Zubiri, F. Zapirain, A. Esnaola, Study of mechanical properties of AISI 316 stainless steel processed by “selective laser melting”, following different manufacturing

strategies, Int. J. Adv. Manuf. Technol. 51 (2010) 639–647. https://doi.org/10.1007/s00170-010-2631-5.

[130] A. Mertens, S. Reginster, Q. Contrepois, T. Dormal, O. Lemaire, J. Lecomte-Beckers, Microstructures and Mechanical Properties of Stainless Steel AISI 316L Processed by Selective Laser Melting, Mater. Sci. Forum. 783–786 (2014) 898–903. https://doi.org/10.4028/www.scientific.net/msf.783-786.898.

[131] B. Zhang, L. Dembinski, C. Coddet, The study of the laser parameters and environment variables effect on mechanical properties of high compact parts elaborated by selective laser melting 316L powder, Mater. Sci. Eng. A. 584 (2013) 21–31. https://doi.org/10.1016/j.msea.2013.06.055.

[132] A. Röttger, K. Geenen, M. Windmann, F. Binner, W. Theisen, Comparison of microstructure and mechanical properties of 316 L austenitic steel processed by selective laser melting with hot-isostatic pressed and cast material, Mater. Sci. Eng. A. 678 (2016) 365–376. https://doi.org/10.1016/j.msea.2016.10.012.

[133] J. Li, D. Deng, X. Hou, X. Wang, G. Ma, D. Wu, G. Zhang, Microstructure and performance optimisation of stainless steel formed by laser additive manufacturing, Mater. Sci. Technol. (United Kingdom). 32 (2016) 1223–1230. https://doi.org/10.1080/02670836.2015.1114774.

[134] A. Mertens, S. Reginster, H. Paydas, Q. Contrepois, T. Dormal, O. Lemaire, J. Lecomte-Beckers, Mechanical properties of alloy Ti–6Al–4V and of stainless steel 316L processed by selective laser melting: influence of out-of-equilibrium microstructures, Powder Metall. 57 (2014) 184–189. https://doi.org/10.1179/1743290114Y.0000000092.

[135] C.S. Hamza Hassn Alsalla, L. Hao, Effect of build orientation on the surface quality, microstructure and mechanical properties of selective laser melting 316L stainless steel, Rapid Prototyp. J. 24 (2018) 9–17. https://www.emerald.com/insight/content/doi/10.1108/RPJ-04-2016-0068/full/html.

[136] P. Eriksson, Evaluation of mechanical and microstructural properties for laser powder-bed fusion 316L, Uppsala Universitet, 2018. http://www.teknat.uu.se/student.

[137] P.A. Kuznetsov, A.A. Zisman, S.N. Petrov, I.S. Goncharov, Structure and mechanical properties of austenitic 316L steel produced by selective laser melting, Russ. Metall. 2016 (2016) 930–934. https://doi.org/10.1134/S0036029516100104.

[138] R.M. Horn, M. Connor, D. Webber, J. Jackson, F. Bolger, Evaluation of additively manufactured materials for nuclear plant components, Miner. Met. Mater. Ser. (2019) 1009–1020. https://doi.org/10.1007/978-3-030-04639-2_63.

[139] S.A. Maloy, M.R. James, G. Willcutt, W.F. Sommer, M. Sokolov, L.L. Snead, M.L. Hamilton, F. Garner, The mechanical properties of 316L/304L stainless steels, Alloy 718 and Mod 9Cr-1Mo after irradiation in a spallation environment, J. Nucl. Mater. 296 (2001) 119–128. https://doi.org/10.1016/S0022-3115(01)00514-1.

[140] A. Riemer, S. Leuders, M. Thöne, H.A. Richard, T. Tröster, T. Niendorf, On the fatigue crack growth behavior in 316L stainless steel manufactured by selective laser melting, Eng. Fract. Mech. 120 (2014) 15–25. https://doi.org/10.1016/j.engfracmech.2014.03.008.

[141] A.B. Spierings, T.L. Starr, K. Wegener, Fatigue performance of additive manufactured metallic parts, Rapid Prototyp. J. 19 (2013) 88–94. https://doi.org/10.1108/13552541311302932.

[142] S. Afkhami, M. Dabiri, S.H. Alavi, T. Björk, A. Salminen, Fatigue characteristics of steels manufactured by selective laser melting, Int. J. Fatigue. 122 (2019) 72–83. https://doi.org/10.1016/j.ijfatigue.2018.12.029.

[143] B. Blinn, F. Krebs, M. Ley, R. Teutsch, T. Beck, Determination of the influence of a stress-relief heat treatment and additively manufactured surface on the fatigue behavior of selectively laser melted AISI 316L by using efficient short-time procedures, Int. J. Fatigue. 131 (2020) 105301.

https://doi.org/10.1016/j.ijfatigue.2019.105301.

[144] K. Solberg, S. Guan, S.M.J. Razavi, T. Welo, K.C. Chan, F. Berto, Fatigue of additively manufactured 316L stainless steel: The influence of porosity and surface roughness, Fatigue Fract. Eng. Mater. Struct. 42 (2019) 2043–2052. https://doi.org/10.1111/ffe.13077.

[145] R. Shrestha, J. Simsiriwong, N. Shamsaei, Fatigue behavior of additive manufactured 316L stainless steel parts: Effects of layer orientation and surface roughness, Addit. Manuf. 28 (2019) 23–38. https://doi.org/10.1016/j.addma.2019.04.011.

[146] R.B. Rebak, X. Lou, P.W. Emigh, M.A. Othon, P.L. Andresen, M. Song, M. Wang, Environmental Cracking and Irradiation Resistant Stainless Steels by Additive Manufacturing, 2018.

[147] X. Lou, M. Song, P.W. Emigh, M.A. Othon, P.L. Andresen, On the stress corrosion crack growth behaviour in high temperature water of 316L stainless steel made by laser powder bed fusion additive manufacturing, Corros. Sci. 128 (2017) 140–153. https://doi.org/10.1016/j.corsci.2017.09.017.

[148] X. Sun, F. Chen, H. Huang, J. Lin, X. Tang, Effects of interfaces on the helium bubble formation and radiation hardening of an austenitic stainless steel achieved by additive manufacturing, Appl. Surf. Sci. 467–468 (2019) 1134–1139. https://doi.org/10.1016/j.apsusc.2018.10.268.

[149] H.R. Brager, The effects of cold working and pre-irradiation heat treatment on void formation in neutron-irradiated type 316 stainless steel, J. Nucl. Mater. (1975). https://doi.org/10.1016/0022-3115(75)90184-1.

[150] J.A. Evans, S.A. Anderson, E.J. Faierson, D. Perez-Nunez, S.M. McDeavitt, Anisotropic Radiation-Induced Changes in Type 316L Stainless Steel Rods Built by Laser Additive Manufacturing, Nucl. Technol. 205 (2019) 563–581. https://doi.org/10.1080/00295450.2018.1502001.

[151] G. Meric de Bellefon, K.M. Bertsch, M.R. Chancey, Y.Q. Wang, D.J. Thoma, Influence of solidification structures on radiation-induced swelling in an additively-manufactured austenitic stainless steel, J. Nucl. Mater. 523 (2019) 291–298. https://doi.org/10.1016/j.jnucmat.2019.06.012.

[152] M. Song, M. Wang, X. Lou, R.B. Rebak, G.S. Was, Radiation damage and irradiation-assisted stress corrosion cracking of additively manufactured 316L stainless steels, J. Nucl. Mater. 513 (2019) 33–44. https://doi.org/10.1016/j.jnucmat.2018.10.044.

[153] Z. Shang, C. Fan, S. Xue, J. Ding, J. Li, T. Voisin, Y.M. Wang, H. Wang, X. Zhang, Response of solidification cellular structures in additively manufactured 316 stainless steel to heavy ion irradiation: an in situ study, Mater. Res. Lett. 7 (2019) 290–297. https://doi.org/10.1080/21663831.2019.1604442.

[154] E.P. Marco Tarini, Nico Pietroni, Paolo Cignoni, Daniele Panozzo, Practical Quad Mesh Simplification, (n.d.). http://meshlabstuff.blogspot.com/2009/12/practical-quad-mesh-simplification.html (accessed March 20, 2020).

[155] K.T. Makiewicz, Development of simultaneous transformation kinetics microstructure model with application to laser metal deposited Ti-6Al-4V and alloy 718, 2013. http://rave.ohiolink.edu/etdc/view?acc_num=osu1366023857%5Cnhttps://drive.google.com/open?id=0B0fTxDBXtHZMWjVpQXdEVzgxRG8.

[156] K. Makiewicz, S.S. Babu, M. Keller, A. Chaudhary, Microstructure evolution during laser additive manufacturing of Ti6Al4V alloy, ASM Proc. Int. Conf. Trends Weld. Res. (2013) 970–977.

[157] J.C. Haley, B. Zheng, U.S. Bertoli, A.D. Dupuy, J.M. Schoenung, E.J. Lavernia, Working distance passive stability in laser directed energy deposition additive manufacturing, Mater. Des. (2019). https://doi.org/10.1016/j.matdes.2018.11.021.

[158] V.D. Manvatkar, A.A. Gokhale, G.J. Reddy, A. Venkataramana, A. De, A.V. G. J. Reddy, A. De,

Estimation of Melt Pool Dimensions, Thermal Cycle, and Hardness Distribution in the Laser-Engineered Net Shaping Process of Austenitic Stainless Steel, Metall. Mater. Trans. A. 42A (2011) 4080–4087.

[159] L. Scime, J. Beuth, A multi-scale convolutional neural network for autonomous anomaly detection and classification in a laser powder bed fusion additive manufacturing process, Addit. Manuf. 24 (2018) 273–286. https://doi.org/10.1016/j.addma.2018.09.034.

[160] Ophir Laser Power Measurement Sensors, (n.d.). https://www.ophiropt.com/laser--measurement/laser-power-energy-meters/products/Laser-Thermal-Power-Sensors/High-Power-Water-Cooled-Thermal-Laser-Measurement-Sensors-And-Power-Pucks (accessed March 19, 2020).

[161] Gentec Laser Power Measurement Sensors, (n.d.). https://www.gentec-eo.com/laser-power-meter (accessed March 19, 2020).

[162] S. Gunn, Calorimetric measurements of laser energy and power, J. Phys. E-SCIENTIFIC INSTRUMENTS. 6 (1973) 105–114.

[163] J. D.A., W. E.D., E. K.M., R. A.L., S. W.R., Laser Power and Energy Measurements, Boulder, Colorado, 1969.

[164] SRI 6009 Radiation Pressure Power Meter, 2018.

[165] V.S. Letokhov, V.G. Minogin, Laser radiation pressure on free atoms, Phys. Rep. 73 (1981) 1–65. https://doi.org/10.1016/0370-1573(81)90116-2.

[166] A. Mahrle, E. Beyer, Theoretical evaluation of radiation pressure magnitudes and effects in laser material processing, Phys. Scr. 94 (2019). https://doi.org/10.1088/1402-4896/ab04c3.

[167] Applications of Laser Radiation Pressure, 210 (2010) 1081–1088.

[168] C. Kevin, Optical Materials: Silicon carbide mirrors benefit high-speed laser scanning, (2008). https://www.laserfocusworld.com/optics/article/16554962/optical-materials-silicon-carbide-mirrors-benefit-highspeed-laser-scanning (accessed March 12, 2020).

[169] S. Moylan, J. Slotwinski, A. Cooke, K. Jurrens, M.A. Donmez, An additive manufacturing test artifact, J. Res. Natl. Inst. Stand. Technol. 119 (2014) 429–459. https://doi.org/10.6028/jres.119.017.

[170] R. Quarshie, S. Machachlan, P. Reeves, D. Whittaker, R. Blake, Shaping Our National Competency in Additive Manufacturing, 2012. https://interact.innovateuk.org/documents/1524978/1866952/Shaping our national competency in additive manufacturing.

[171] NIST, Measurement Science Roadmap for Metal-Based Additive Manufacturing, (2013) 86. https://doi.org/10.1007/s13398-014-0173-7.2.

[172] M. Van Elsen, Complexity of Selective Laser Melting: a new optimisation approach, KATHOLIEKE UNIVERSITEIT LEUVEN, 2007. https://doi.org/10.1111/jre.12251.

[173] S.K. Everton, M. Hirsch, P.I. Stavroulakis, R.K. Leach, A.T. Clare, Review of in-situ process monitoring and in-situ metrology for metal additive manufacturing, Mater. Des. 95 (2016) 431–445. https://doi.org/10.1016/j.matdes.2016.01.099.

[174] G. Tapia, A. Elwany, A Review on Process Monitoring and Control in Metal-Based Additive Manufacturing, J. Manuf. Sci. Eng. 136 (2014). https://doi.org/10.1115/1.4028540.

[175] S. Berumen, F. Bechmann, S. Lindner, J.P. Kruth, T. Craeghs, Quality control of laser- and powder bed-based Additive Manufacturing (AM) technologies, Phys. Procedia. 5 (2010) 617–622. https://doi.org/10.1016/j.phpro.2010.08.089.

[176] F. Herzog, F. Bechmann, S. Berumen, J.P. Kruth, T. Craeghs, Method for Producing a Three-Dimensional Component, WO1996008749 A3, 1995.

[177] A. Fathi, E. Toyserkani, A. Khajepour, M. Durali, Prediction of melt pool depth and dilution in laser powder deposition, J. Phys. D. Appl. Phys. 39 (2006) 2613–2623. https://doi.org/10.1088/0022-3727/39/12/022.

[178] M. Mani, B.M. Lane, M.A. Donmez, S.C. Feng, S.P. Moylan, A review on measurement science needs for real-time control of additive manufacturing metal powder bed fusion processes, Int. J. Prod. Res. 55 (2017) 1400–1418. https://doi.org/10.1080/00207543.2016.1223378.

[179] A. Fathi, A. Khajepour, M. Durali, E. Toyserkani, Geometry Control of the Deposited Layer in a Nonplanar Laser Cladding Process Using a Variable Structure Controller, J. Manuf. Sci. Eng. 130 (2008) 031003. https://doi.org/10.1115/1.2823085.

[180] D. Salehi, M. Brandt, Melt pool temperature control using LabVIEW in Nd:YAG laser blown powder cladding process, Int. J. Adv. Manuf. Technol. 29 (2006) 273–278. https://doi.org/10.1007/s00170-005-2514-3.

[181] T.A. Davis, Y.C. Shin, Vision-based clad height measurement, Mach. Vis. Appl. 22 (2011) 129–136. https://doi.org/10.1007/s00138-009-0240-9.

[182] E. Rodriguez, J. Mireles, C.A. Terrazas, D. Espalin, M.A. Perez, R.B. Wicker, Approximation of absolute surface temperature measurements of powder bed fusion additive manufacturing technology using in situ infrared thermography, Addit. Manuf. 5 (2015) 31–39. https://doi.org/10.1016/j.addma.2014.12.001.

[183] G. Bi, C.N. Sun, A. Gasser, Study on influential factors for process monitoring and control in laser aided additive manufacturing, J. Mater. Process. Technol. 213 (2013) 463–468. https://doi.org/10.1016/j.jmatprotec.2012.10.006.

[184] M. Islam, T. Purtonen, H. Piili, A. Salminen, O. Nyrhilä, Temperature profile and imaging analysis of laser additive manufacturing of stainless steel, Phys. Procedia. 41 (2013) 835–842. https://doi.org/10.1016/j.phpro.2013.03.156.

[185] S. Barua, F. Liou, J. Newkirk, T. Sparks, Vision-based defect detection in laser metal deposition process, Rapid Prototyp. J. 20 (2014) 77–85. https://doi.org/10.1108/RPJ-04-2012-0036.

[186] J.C. Heigel, P. Michaleris, E.W. Reutzel, Thermo-mechanical model development and validation of directed energy deposition additive manufacturing of Ti-6Al-4V, Addit. Manuf. 5 (2015) 9–19. https://doi.org/10.1016/j.addma.2014.10.003.

[187] M. Zeinali, A. Khajepour, Height Control in Laser Cladding Using Adaptive Sliding Mode Technique: Theory and Experiment, J. Manuf. Sci. Eng. 132 (2010) 041016. https://doi.org/10.1115/1.4002023.

[188] L. Tang, R.G. Landers, Melt Pool Temperature Control for Laser Metal Deposition Processes—Part I: Online Temperature Control, J. Manuf. Sci. Eng. 132 (2010) 011010–1. https://doi.org/10.1115/1.4000883.

[189] L. Tang, R.G. Landers, Melt Pool Temperature Control for Laser Metal Deposition Processes—Part II: Layer-to-Layer Temperature Control, J. Manuf. Sci. Eng. 132 (2010) 011011. https://doi.org/10.1115/1.4000883.

[190] E.R. Denlinger, Residual Stress and Distortion Modeling of Electron Beam Direct Manufacturing Ti-6Al-4V, in: M. Gouge, P. Michaleris (Eds.), Thermo-Mechanical Model. Addit. Manuf., Butterworth-Heinemann, 2018: pp. 153–166. https://doi.org/https://doi.org/10.1016/B978-0-12-811820-7.00011-2.

[191] E.R. Denlinger, J.C. Heigel, P. Michaleris, T.A. Palmer, Effect of inter-layer dwell time on distortion and residual stress in additive manufacturing of titanium and nickel alloys, J. Mater. Process. Technol. 215 (2015) 123–131. https://doi.org/10.1016/j.jmatprotec.2014.07.030.

[192] A.J. Dunbar, E.R. Denlinger, J. Heigel, P. Michaleris, P. Guerrier, R. Martukanitz, T.W. Simpson, Development of experimental method for in situ distortion and temperature measurements during

the laser powder bed fusion additive manufacturing process, Addit. Manuf. 12 (2016) 25–30. https://doi.org/10.1016/j.addma.2016.04.007.

[193] General Electric Product Documentation, (2018).

[194] AddUp Manager User Manual - Version 2.16, (2018).

[195] L. Scime, J. Beuth, Using machine learning to identify in-situ melt pool signatures indicative of flaw formation in a laser powder bed fusion additive manufacturing process, Addit. Manuf. 25 (2019) 151–165. https://doi.org/10.1016/j.addma.2018.11.010.

[196] T. Craeghs, S. Clijsters, E. Yasa, J.-P. Kruth, Online Quality Control of Selective Laser Melting, Solid Free. Fabr. Proc. 13 (2011) 212–226.

[197] S. Kleszczynski, J. Zur Jacobsmühlen, J.T. Sehrt, G. Witt, Error detection in laser beam melting systems by high resolution imaging, 23rd Annu. Int. Solid Free. Fabr. Symp. - An Addit. Manuf. Conf. SFF 2012. (2012) 975–987.

[198] M. Aminzadeh, A Machine Vision System for In-Situ Quality Inspection in Metal Powder-Bed Additive Manufacturin, 2016. https://smartech.gatech.edu/handle/1853/56291.

[199] J. Zur Jacobsmuhlen, S. Kleszczynski, G. Witt, D. Merhof, Detection of elevated regions in surface images from laser beam melting processes, IECON 2015 - 41st Annu. Conf. IEEE Ind. Electron. Soc. (2015) 1270–1275. https://doi.org/10.1109/IECON.2015.7392275.

[200] J. Zur Jacobsmuhlen, S. Kleszczynski, D. Schneider, G. Witt, High resolution imaging for inspection of Laser Beam Melting systems, Conf. Rec. - IEEE Instrum. Meas. Technol. Conf. (2013) 707–712. https://doi.org/10.1109/I2MTC.2013.6555507.

[201] ConceptLaser, Achieve the highest possible quality in series production thanks to LaserCUSING ®, (2017). https://www.concept-laser.de/fileadmin/user_upload/1603_QM_Prospect_EN.pdf.

[202] B.M. Colosimo, E. Grossi, F. Caltanissetta, M. Grasso, Penelope: A Novel Prototype for In Situ Defect Removal in LPBF, Jom. 72 (2020) 1332–1339. https://doi.org/10.1007/s11837-019-03964-0.

[203] Z. Prevorovsky, J. Krofta, J. Kober, M. Chlada, A. Kirchner, Non-linear Ultrasonic Spectroscopy of 3d Printed Metallic Samples, Insight - Non-Destructive Test. Cond. Monit. 61 (2019) 157–161. https://doi.org/10.1784/insi.2019.61.3.157.

[204] S. Everton, P. Dickens, C. Tuck, B. Dutton, Evaluation of laser ultrasonic testing for inspection of metal additive manufacturing, Laser 3D Manuf. II. 9353 (2015) 935316. https://doi.org/10.1117/12.2078768.

[205] P. Mercelis, J.-P. Kruth, Residual stresses in Selective Laser Sintering and Selective Laser Melting, 16th Solid Free. Fabr. Symp. SFF 2005. 12 (2005) 109–131.

[206] A. Wu, M.M. LeBlanc, M. Kumar, G.F. Gallegos, D.W. Brown, W.E. King, Effect of laser scanning pattern and build direction in additive manufacturing on anisotropy, porosity and residual stress, in: 2014 TMS Annu. Meet. Exhib., San Diego, CA, 2014.

[207] T. Gnäupel-Herold, J. Slotwinski, S. Moylan, Neutron measurements of stresses in a test artifact produced by laser-based additive manufacturing, in: AIP Conf. Proc., 2014: pp. 1205–1212. https://doi.org/10.1063/1.4864958.

[208] P. Rangaswamy, T. M Holden, R. Rogge, M. L Griffith, Residual stresses in components formed by the laser-engineered net shaping (LENS (R)) process, J. Strain Anal. Eng. Des. 38 (2003). https://doi.org/10.1243/030932403770735881.

[209] C.A. Brice, W.H. Hofmeister, Determination of bulk residual stresses in electron beam additive-manufactured aluminum, Metall. Mater. Trans. A Phys. Metall. Mater. Sci. 44A (2013) 5147–5153. https://doi.org/10.1007/s11661-013-1847-z.

[210] A.S. Wu, D.W. Brown, M. Kumar, G.F. Gallegos, W.E. King, An Experimental Investigation into

Additive Manufacturing-Induced Residual Stresses in 316L Stainless Steel, Metall. Mater. Trans. A Phys. Metall. Mater. Sci. 45A (2014) 6260–6270. https://doi.org/10.1007/s11661-014-2549-x.

[211] T. Watkins, H. Bilheux, K. An, A. Payzant, R.R. Dehoff, C. Duty, W. Peter, C. Blue, C.A. Brice, Neutron Characterization for Additive Manufacturing, Adv. Mater. Process. 171 (2013) 23–27.

[212] P. Rangaswamy, M.L. Griffith, M.B. Prime, T.M. Holden, R.B. Rogge, J.M. Edwards, R.J. Sebring, Residual stresses in LENS® components using neutron diffraction and contour method, Mater. Sci. Eng. A. 399 (2005) 72–83. https://doi.org/10.1016/j.msea.2005.02.019.

[213] J.M. Robinson, B.A. Van Brussel, J.T.M. De Hosson, R.C. Reed, X-ray measurement of residual stresses in laser surface melted Ti-6Al-4V alloy, Mater. Sci. Eng. A. 208 (1996) 143–147. https://doi.org/10.1016/0921-5093(95)10158-6.

[214] M.B. Prime, Cross-Sectional Mapping of Residual Stresses by Measuring the Surface Contour After a Cut, J. Eng. Mater. Technol. 123 (2001) 162. https://doi.org/10.1115/1.1345526.

[215] S. Suresh, A.E. Giannakopoulos, A new method for estimating residual stresses by instrumented sharp indentation, Acta Mater. 46 (1998) 5755–5767. https://doi.org/https://doi.org/10.1016/S1359-6454(98)00226-2.

[216] M.. Griffith, M.. Schlienger, L.. Harwell, M.. Oliver, M.. Baldwin, M.. Ensz, M. Essien, J. Brooks, C.. Robino, J.. Smugeresky, W.. Hofmeister, M.. Wert, D.. Nelson, Understanding thermal behavior in the LENS process, Mater. Des. 20 (1999) 107–113. https://doi.org/10.1016/s0261-3069(99)00016-3.

[217] R.J. Moat, A.J. Pinkerton, L. Li, P.J. Withers, M. Preuss, Residual stresses in laser direct metal deposited Waspaloy, Mater. Sci. Eng. A. 528 (2011) 2288–2298. https://doi.org/https://doi.org/10.1016/j.msea.2010.12.010.

[218] M.F. Zaeh, G. Branner, Investigations on residual stresses and deformations in selective laser melting, Prod. Eng. 4 (2010) 35–45. https://doi.org/10.1007/s11740-009-0192-y.

[219] P. Prabhakar, W.J. Sames, R. Dehoff, S.S. Babu, Computational modeling of residual stress formation during the electron beam melting process for Inconel 718, Addit. Manuf. 7 (2015) 83–91. https://doi.org/https://doi.org/10.1016/j.addma.2015.03.003.

[220] L. Kempen, L. Thijs, B. Vrancken, S. Buls, J. Van Humbeeck, J.-P. Kruth, Producing crack-free, high density M2 HSS parts by Selective Laser Melting: Pre-heating the baseplate, Proc. 24th Int. Solid Free. Fabr. Symp. (2013) 131–139.

[221] S. Kou, Welding Metallurgy, 2nd ed., John Wiley and Sons, Hoboken, New Jersey, 2003. http://www.amazon.com/Welding-Metallurgy-Sindo-Kou/dp/0471434914.

[222] T. Mukherjee, W. Zhang, T. DebRoy, An improved prediction of residual stresses and distortion in additive manufacturing, Comput. Mater. Sci. 126 (2017) 360–372. https://doi.org/10.1016/j.commatsci.2016.10.003.

[223] L.W. Koester, H. Taheri, T.A. Bigelow, P.C. Collins, L.J. Bond, Nondestructive Testing for Metal Parts Fabricated Using Powder-Based Additive Manufacturing, Mater. Eval. (2018).

[224] J.A. Slotwinski, E.J. Garboczi, K.M. Hebenstreit, Porosity Measurements and Analysis for Metal Additive Manufacturing Process Control, J. Res. Natl. Inst. Stand. Technol. 119 (2014) 494. https://doi.org/10.6028/jres.119.019.

[225] E. Girardin, C. Renghini, J. Dyson, V. Calbucci, F. Moroncini, G. Albertini, Characterization of Porosity in a Laser Sintered MMCp Using X-Ray Synchrotron Phase Contrast Microtomography, Mater. Sci. Appl. 02 (2011) 1322–1330. https://doi.org/10.4236/msa.2011.29180.

[226] J.W. Elmer, J. Vaja, H.D. Carlton, The effect of reduced pressure on laser keyhole weld porosity and weld geometry in commercially pure titanium and nickel, Weld. J. 94. 95 (2016) 419–430.

[227] J.W. Elmer, J. Vaja, H.D. Carlton, R. Pong, The Effect of Ar and N2 Shielding Gas on Laser Weld Porosity in Steel, Stainless Steel, and Nickel, Weld. J. 94 (2015) 313–325.

[228] W.E. King, H.D. Barth, V.M. Castillo, G.F. Gallegos, J.W. Gibbs, D.E. Hahn, C. Kamath, A.M. Rubenchik, Observation of keyhole-mode laser melting in laser powder-bed fusion additive manufacturing, J. Mater. Process. Technol. 214 (2014) 2915–2925. https://doi.org/10.1016/j.jmatprotec.2014.06.005.

[229] L.L. Parimi, G. Ravi, D. Clark, M.M. Attallah, Microstructural and texture development in direct laser fabricated IN718, Mater. Charact. 89 (2014) 102–111. https://doi.org/10.1016/j.matchar.2013.12.012.

[230] M.L. Montero-Sistiaga, M. Godino-Martinez, K. Boschmans, J.P. Kruth, J. Van Humbeeck, K. Vanmeensel, Microstructure evolution of 316L produced by HP-SLM (high power selective laser melting), Addit. Manuf. 23 (2018) 402–410. https://doi.org/10.1016/j.addma.2018.08.028.

[231] T. Ronneberg, C.M. Davies, P.A. Hooper, Revealing relationships between porosity, microstructure and mechanical properties of laser powder bed fusion 316L stainless steel through heat treatment, Mater. Des. 189 (2020) 108481. https://doi.org/10.1016/j.matdes.2020.108481.

[232] A. Leicht, U. Klement, E. Hryha, Effect of build geometry on the microstructural development of 316L parts produced by additive manufacturing, Mater. Charact. 143 (2018) 137–143. https://doi.org/10.1016/j.matchar.2018.04.040.

[233] T. Tancogne-Dejean, A.B. Spierings, D. Mohr, Additively-manufactured metallic micro-lattice materials for high specific energy absorption under static and dynamic loading, Acta Mater. 116 (2016) 14–28. https://doi.org/10.1016/j.actamat.2016.05.054.

[234] T. Nakamoto, N. Shirakawa, Y. Miyata, H. Inui, Selective laser sintering of high carbon steel powders studied as a function of carbon content, J. Mater. Process. Technol. 209 (2009) 5653–5660. https://doi.org/10.1016/j.jmatprotec.2009.05.022.

[235] R. Li, H. Chen, C. Chen, H. Zhu, M. Wang, T. Yuan, B. Song, Selective Laser Melting of Gas Atomized Al–3.02Mg–0.2Sc–0.1Zr Alloy Powder: Microstructure and Mechanical Properties, Adv. Eng. Mater. 1800650 (2018) 1–15. https://doi.org/10.1002/adem.201800650.

[236] H. Ali, H. Ghadbeigi, K. Mumtaz, Effect of scanning strategies on residual stress and mechanical properties of Selective Laser Melted Ti6Al4V, Mater. Sci. Eng. A. 712 (2018) 175–187. https://doi.org/10.1016/j.msea.2017.11.103.

[237] A.Y. Alfaify, J. Hughes, K. Ridgway, Critical evaluation of the pulsed selective laser melting process when fabricating Ti64 parts using a range of particle size distributions, Addit. Manuf. 19 (2018) 197–204. https://doi.org/10.1016/j.addma.2017.12.003.

[238] U. Scipioni Bertoli, A.J. Wolfer, M.J. Matthews, J.P.R. Delplanque, J.M. Schoenung, On the limitations of Volumetric Energy Density as a design parameter for Selective Laser Melting, Mater. Des. 113 (2017) 331–340. https://doi.org/10.1016/j.matdes.2016.10.037.

[239] A. Keshavarzkermani, E. Marzbanrad, R. Esmaeilizadeh, Y. Mahmoodkhani, U. Ali, P.D. Enrique, N.Y. Zhou, A. Bonakdar, E. Toyserkani, An investigation into the effect of process parameters on melt pool geometry, cell spacing, and grain refinement during laser powder bed fusion, Opt. Laser Technol. 116 (2019) 83–91. https://doi.org/10.1016/j.optlastec.2019.03.012.

[240] B. Barkia, P. Aubry, P. Haghi-Ashtiani, T. Auger, L. Gosmain, F. Schuster, H. Maskrot, On the origin of the high tensile strength and ductility of additively manufactured 316L stainless steel: Multiscale investigation, J. Mater. Sci. Technol. 41 (2020) 209–218. https://doi.org/10.1016/j.jmst.2019.09.017.

[241] X. Lou, M.A. Othon, R.B. Rebak, Corrosion fatigue crack growth of laser additively-manufactured 316L stainless steel in high temperature water, Corros. Sci. 127 (2017) 120–130. https://doi.org/10.1016/j.corsci.2017.08.023.

[242] V.P. Matilainen, J. Pekkarinen, A. Salminen, Weldability of additive manufactured stainless steel, Phys. Procedia. 83 (2016) 808–817. https://doi.org/10.1016/j.phpro.2016.08.083.

[243] S. V. Kuryntsev, The influence of pre-heat treatment on laser welding of T-joints of workpieces made of selective laser melting steel and cold rolled stainless steel, Opt. Laser Technol. 107 (2018) 59–66. https://doi.org/10.1016/j.optlastec.2018.05.031.

[244] V. Laitinen, Weldability of powder bed fusion fabricated stainless steel 316L sheets to cold rolled sheet metal LAPPEENRANTA UNIVERSITY OF TECHNOLOGY LUT School of Energy Systems LUT Mechanical Engineering WELDABILITY OF POWDER BED FUSION FABRICATED STAINLESS STEEL 31, (2019).

[245] J. Simpson, Propagation of Uncertainty in Porosity Measurement Methods for Additive Manufacturing, Unpublished. (n.d.).